Advancements in Laser-Induced Lifetime Measurements for Combustion and Plasma Studies

Nilsson, Sebastian

2024

Document Version:
Publisher's PDF, also known as Version of record

Advancements in Laser-Induced Lifetime Measurements for Combustion and Plasma Studies

by Sebastian Nilsson

LUND
UNIVERSITY

Thesis for the degree of Philosophy Doctor
Thesis advisors: Dr. Andreas Ehn, Prof. Mattias Richter, Dr. Jingou Sun
Faculty opponent: Dr. Timothy Ombrello

To be presented, with the permission of the Faculty of Engineering at Lund University for public criticism in the Rydbergs lecture hall at the Department of Physics on Friday, the 29th of November 2024 at 9:00.

Organization
LUND UNIVERSITY

Department of Physics
Box 118
SE–221 00 LUND
Sweden

Document name
DOCTORAL DISSERTATION

Date of disputation
2024-11-29

Sponsoring organization

Author(s)
Sebastian Nilsson

Title and subtitle
Advancements in Laser-Induced Lifetime Measurements for Combustion and Plasma Studies:

Abstract
This thesis focuses on two main research areas: the development of thermographic phosphors for high-temperature surface measurements and the application of laser-based optical diagnostics in non-thermal plasma studies. Both projects utilize laser diagnostics to achieve non-invasive, in-situ measurements, allowing the investigation of the temporal evolution of laser-induced signals.

The first section centers on the development and characterization of high-temperature phosphors, specifically for use in hydrogen-powered gas turbines. When excited by lasers, these phosphors emit phosphorescence, with temperature-dependent spectral and temporal shifts that enable precise surface temperature measurements. The work emphasizes temporal characterization, which is crucial for applications in extreme temperature conditions.

The second section investigates advanced optical diagnostics for non-thermal plasmas. These plasmas are highly dynamic and challenging to measure using conventional methods, but laser-based techniques such as laser-induced fluorescence and Rayleigh scattering provide non-intrusive, high-resolution measurements. Key developments include Fluorescence Lifetime Imaging for quenching-corrected diagnostics and 3D emission tomography for spatially resolved plasma studies.

In summary, this thesis develops laser diagnostics for high-temperature and plasma applications, contributing to the advancement of efficient and sustainable technologies.

Key words
Fluorescence Lifetime Imaging, Phosphor Thermometry, Plasma, Discharges, Laser Diagnostics, Tomography, Quenching Correction

Classification system and/or index terms (if any)

Supplementary bibliographical information

Language
English

ISSN and key title
ISSN: 1102-8718

ISBN
978-91-8104-197-2 (print)
978-91-8104-198-9 (pdf)

Recipient's notes

Number of pages
303

Price

Security classification

Advancements in Laser-Induced Lifetime Measurements for Combustion and Plasma Studies

by Sebastian Nilsson

LUND
UNIVERSITY

A doctoral thesis at a university in Sweden takes either the form of a single, cohesive research study (monograph) or a summary of research papers (compilation thesis), which the doctoral student has written alone or together with one or several other author(s).

In the latter case the thesis consists of two parts. An introductory text puts the research work into context and summarizes the main points of the papers. Then, the research publications themselves are reproduced, together with a description of the individual contributions of the authors. The research papers may either have been already published or are manuscripts at various stages (in press, submitted, or in draft).

Cover illustration front: A gliding arc discharge in N_2 and Ar gas mixture while being sprayed with n-heptane.

Cover illustration back: A collage featuring images from various experimental campaigns throughout my thesis.

Funding information: The thesis work was financially supported by European Union funding through the European Research Council LAPLAS (852394) and HYFLEXPOWER (884229). Also Funding from Swedish Research Council through project 2021-04506 and funding from the Royal Physiographic Society of Lund is greatly appreciated.

Faculty of Engineering, Department of Physics

ISBN: 978-91-8104-197-2 (print)
ISBN: 978-91-8104-198-9 (pdf)
ISSN: 1102-8718
LRCP: 259

Printed in Sweden by Media-Tryck, Lund University, Lund 2024

Media-Tryck is a Nordic Swan Ecolabel certified provider of printed material. Read more about our environmental work at www.mediatryck.lu.se

MADE IN SWEDEN

Dedicated to my grandfather, Bo, whose last words to me were:
"Follow your own path."

Contents

List of publications

I **Investigating photomultiplier tube nonlinearities in high-speed phosphor thermometry using light emitting diode simulated decay curves**
H. Feuk, **S. Nilsson**, M. Aldén, M. Richter
Review of Scientific Instruments 92 (12)

II **Automated phosphor thermometry lifetime calibration of multiple phosphors and emission lines to above 1900 K**
H. Feuk, **S. Nilsson**, M. Richter
Measurement Science and Technology 33 (12), 127003

III **Laser excitation effects in lifetime-based high-speed phosphor thermometry**
H. Feuk, **S. Nilsson**, M. Richter
Journal of Luminescence 250, 119106

IV **Fluorescence lifetime imaging through scattering media**
S. Nilsson, E. Kristensson, M. Aldén, J. Bood, A. Ehn
Scientific Reports 13 (1), 3066

V **Temperature resolved decay time components of Mg_4FGeO_6: Mn using the maximum entropy method**
H. Feuk, **S. Nilsson**, M. Richter
Review of Scientific Instruments 94 (3)

VI **Upconversion phosphor thermometry for use in thermal barrier coatings**
H. Feuk, **S. Nilsson**, M. Richter
Measurement Science and Technology 34 (6), 064003

VII **High temperature thermographic phosphors YAG: Tm; Li and YAG: Dy in reduced oxygen environments**
S. Nilsson, H. Feuk, M. Richter
Journal of Luminescence 256, 119645

VIII **Fiber-coupled phosphor thermometry for wall temperature measurements in a full-scale hydrogen gas turbine combustor**
P. Nau, A. Müller, N. Petry, **S. Nilsson**, T. Endres, M. Richter, B. Witzel
Measurement Science and Technology 34 (10), 104003

IX **3D-tomographic reconstruction of gliding arc plasma**

D. Sanned, **S. Nilsson**, A. Roth, E. Berrocal, A. Ehn, M. Richter
Applied Physics Letters 123 (7)

X **Effect of a single nanosecond pulsed discharge on a flat methane–air flame**

Y. Bao, C. Kong, J. Ravelid, J. Sun, **S. Nilsson**, E. Kristensson, A. Ehn
Applications in Energy and Combustion Science 16, 100198

XI **Application of emission spectroscopy in plasma-assisted NH_3/air combustion using nanosecond pulsed discharge**
J. Sun, Y. Bao, J. Ravelid, **S. Nilsson**, AA. Konnov, A. Ehn
Combustion and Flame 263, 113400

XII **Photofragmentation laser-induced fluorescence imaging of CH_3 by structured illumination in a plasma discharge**
S. Nilsson, J. Ravelid, J. Park, MS. Cha, A. Ehn
Optics Express 32 (15), 26492-26499

XIII **Holistic analysis of a gliding arc discharge using 3D tomography and single-shot fluorescence lifetime imaging**
S. Nilsson, D. Sanned, A. Roth, J. Sun , E. Berrocal, M. Richter, A. Ehn
Communications Engineering 3, 103 (2024)

XIV **Fluorescence lifetime imaging of nitric oxide in nanosecond pulsed discharge-assisted NH_3/air flames**
J. Sun, **S. Nilsson**, J. Ravelid, Y. Bao, A. Ehn
Manuscript in preparation

Related Work

Observation of thickness-independent ultrafast relaxation times in MPCVD few-layer graphene
Tânia M. Ribeiro, Tiago E. C. Magalhães, Bohdan Kulyk, Alexandre F. Carvalho, **Sebastian Nilsson**, Henrik Feuk, António J. S. Fernandes, Florinda Costa, Paulo T. Guerreiro, Helder Crespo
Carbon, page 119700, 2024

Acknowledgments

I would like to extend my deepest gratitude to everyone who has supported and inspired me throughout the process of completing this thesis.

First, to my family your support and belief in me have been my constant source of strength.

To my division, thank you for creating an outstanding work environment. Your support and friendliness has been invaluable, and I couldn't have wished for a better place to grow.

A special thanks to my supervisors, Andreas, Mattias and Jinguo, for your hands-off approach, which allowed me to develop independently, while always being there when I needed guidance. The banter along the way made the journey even more enjoyable.

To my closest colleagues, Henrik, thank you for being a great friend, helping me settle in and to hit the ground running, and for our shared adventures in Germany, Canda and USA. Yupan, Jonas, and Jinguo our memorable Monday meetings and the trip to Japan will always stay with me.

To Mattias' group, thank you for your warm welcome and support. And to Elias' group, it has been a privilege working with you. The unforgettable "tombola" sessions with Vassily, David, Martin and more, was a way to relax and have fun and will always bring a smile.

To David, not only for being a great friend but also for the unforgettable times in the lab and beyond, like our mountain biking trip in Whistler.

To Saga, I'm deeply grateful for recommending this position and for the many shared experiences and memories we have created over the years.

Johan, thank you for forcing me into teaching from day one. It's been a rewarding experience, and I look forward to our future endeavors with the same sense of fun and excitement.

Marco, my first office mate, you were a kind and supportive presence with a brilliant sense of humor. I'm grateful for the time we shared.

Lastly, to everyone I may have missed,this thesis belongs as much to you as it does to me. The exceptional environment you all helped build made this possible, and it's a time I will cherish forever. Thank you all.

Popular summary in English

Recent technological advancements have led to the creation of highly specialized systems across various industries, enabling tasks that were once beyond imagination. As the global demand for sustainable and efficient energy solutions grows, the urgency for innovation in technology has never been greater. These advancements are not simply incremental but represent transformative changes that are reshaping entire sectors. From the expansion of renewable energy sources like solar and wind to the improvement of traditional fossil fuel systems and nuclear power, technology is driving a more sustainable and efficient future.

Methods for analyzing and developing energy systems are critical for enabling efficient and sustainable alternatives to conventional energy production. Progress in optical diagnostics is essential for advancing such sustainable energy systems, especially as the global shift toward clean energy accelerates. These non-invasive techniques use photons to access difficult-to-reach areas without disrupting the system under investigation and can capture and quantify complex phenomena that conventional tools often miss. Conventional measurement techniques, while useful, often lack the spatial and temporal resolution needed to capture fine-scale phenomena in plasma and combustion environments. In contrast, laser diagnostics offer a higher degree of precision, allowing for the detection of rapid changes in temperature, pressure, and species concentrations with unparalleled detail. This specialized information is crucial for understanding the intricate dynamics within energy systems, making laser diagnostics indispensable for refining models and optimizing system performance. The ability to measure and optimize performance in real-time without compromising system integrity is increasingly vital. Hence, further study of these techniques is essential to push the boundaries of what is currently achievable in energy research.

These innovative measurement techniques are more than just tools for analysis; they are catalysts for further innovation. By providing detailed insights into the performance and efficiency of new technologies, they enable researchers and engineers to refine and improve these systems, pushing the boundaries of possibility. Thus, measurement techniques play a dual role: validating current advancements and laying the groundwork for future breakthroughs.

This work utilizes laser diagnostics to investigate the temporal response of laser induced signals, allowing for the determination of temperature and relative number densities. The work presented here contributes to the advancement of sustainable energy systems by applying and developing laser diagnostic techniques to improve the efficiency of hydrogen-powered gas turbines. The transition to hydrogen as a fuel source is crucial for reducing carbon emissions and mitigating climate change, but it requires precise control and a deep understanding of combustion processes. In this research, laser diagnostics are used to develop and characterize thermographic phosphors for inline temperature measurements within

these hydrogen turbines, aiding optimization and minimizing environmental impact.

Advanced laser and optical measurement techniques are proving invaluable in the study of non-thermal plasmas, or cold plasmas, which are increasingly utilized in various industrial processes due to their ability to initiate chemical reactions at low temperatures. This capability is particularly beneficial in fields such as combustion control, pollution control, surface treatment, and medical applications. However, accurately measuring the physical properties of these plasmas such as electron density, temperature, and chemical composition remains challenging due to their dynamic and non-equilibrium nature. To address these challenges, advanced laser diagnostic techniques, including fluorescence imaging and 3D tomography, have been employed to study gliding arcs, a type of non-thermal plasma with significant potential in environmental and energy applications. These techniques provide detailed insights into the behavior and characteristics of gliding arcs, enabling further optimization of these systems. Additionally, photofragmentation laser-induced fluorescence has been used to study methyl radicals in a Dielectric Barrier Discharge (DBD) reactor, a widely used tool in plasma chemistry. This method allows for the selective and sensitive detection of methyl radicals, offering deeper insights into the chemical processes within DBD reactors and contributing to the development of more efficient and sustainable industrial practices.

Together, these innovations in laser diagnostics and optical measurement techniques are not only pushing the frontiers of scientific understanding but are also directly contributing to the development of future energy systems. These systems promise to be more efficient, sustainable, and capable of meeting the global energy challenges of the coming decades.

Populärvetenskaplig sammanfattning på svenska

De senaste teknologiska framstegen har lett till skapandet av högspecialiserade system inom olika industrier, vilket möjliggör uppgifter som tidigare varit otänkbara. I takt med att den globala efterfrågan på hållbara och effektiva energilösningar ökar, har behovet av innovation inom teknik aldrig varit större. Dessa framsteg representerar transformativa förändringar som omformar hela sektorer. Från utbyggnaden av förnybara energikällor som sol- och vindenergi till förbättringen av traditionella fossila bränslesystem och kärnkraft, driver teknologin en mer hållbar och effektiv framtid.

Metoder för att analysera och utveckla energisystem är avgörande för att möjliggöra effektiva och hållbara alternativ till konventionell energiproduktion. Framsteg inom optisk diagnostik är viktiga för att främja sådana hållbara energisystem, särskilt när den globala övergången till ren energi accelererar. Dessa icke-invasiva tekniker använder fotoner för att komma åt svåråtkomliga områden utan att störa systemet som undersöks, och de kan fånga och kvantifiera komplexa fenomen som konventionella verktyg ofta missar. Konventionella mättekniker, även om de är användbara, saknar ofta den rumsliga och tidsmässiga upplösning som krävs för att fånga småskaliga fenomen i plasma- och förbränningsmiljöer. Laserdiagnostik, å andra sidan, erbjuder en högre grad av precision, vilket gör det möjligt att upptäcka snabba förändringar i temperatur, tryck och koncentrationer av ämnen med oöverträffad upplösning. Den här specialiserade informationen är avgörande för att förstå de komplexa dynamikerna inom energisystem, vilket gör laserdiagnostik är ett viktigt verktyg för att förfina modeller och optimera systemens prestanda. Förmågan att mäta och optimera prestanda i realtid utan att kompromissa systemets integritet blir allt viktigare. Därför är vidare studier av dessa tekniker nödvändiga för att driva gränserna vidare för vad som för närvarande är möjligt inom energiforskning.

Dessa innovativa mättekniker är mer än bara analysverktyg; de fungerar som katalysatorer för ytterligare innovation. Genom att tillhandahålla detaljerade insikter i prestanda och effektivitet hos nya teknologier gör de det möjligt för forskare och ingenjörer att förfina och förbättra dessa system, vilket driver gränserna för vad som är möjligt. Således spelar mättekniker en dubbel roll: de validerar nuvarande framsteg och lägger grunden för framtida genombrott.

Detta arbete använder laserdiagnostik för att undersöka den temporala responsen hos laser inducerade signaler, vilket möjliggör bestämning av temperatur och relativa antaldensiteter. Arbetet som presenteras här bidrar till utvecklingen av hållbara energisystem genom att tillämpa och utveckla laserdiagnostiska tekniker för att förbättra effektiviteten hos vätgasdrivna gasturbiner. Övergången till vätgas som bränslekälla är avgörande för att minska koldioxidutsläppen och mildra klimatförändringarna, men det kräver exakt kontroll och djup förståelse av förbränningsprocesser. I denna forskning används laserdiagnostik för att

utveckla och karakterisera termografiska fosforer för inline temperaturmätningar inom dessa väteturbiner, vilket bidrar till optimering och minimering av miljöpåverkan.

Avancerade laser- och optiska mättekniker visar sig ovärderliga i studier av icke-termiska plasman, eller kalla plasman, som alltmer används i olika industriella processer på grund av deras förmåga att initiera kemiska reaktioner vid låga temperaturer. Denna kapacitet är särskilt fördelaktig inom områden som förbränningskontroll, föroreningskontroll, och ytbehandling. Dock är det svårt att noggrant mäta de fysiska egenskaperna hos dessa plasman såsom elektrondensitet, temperatur och kemisk sammansättning på grund av deras dynamiska och icke-jämviktskaraktär. För att hantera dessa utmaningar har avancerade laserdiagnostiska tekniker, inklusive fluorescensavbildning och 3D-tomografi, använts för att studera glidbågar, en typ av icke-termiskt plasma med stor potential inom miljö- och energiområden. Dessa tekniker ger detaljerade insikter i glidbågarnas beteende och egenskaper, vilket möjliggör ytterligare optimering av dessa system. Dessutom har fotofragmenteringlaserinducerad fluorescens använts för att studera metylradikaler i endielektrisk barriär urladdnings reaktor (DBD-reaktor), ett verktyg som ofta används inom plasmakemi. Denna metod möjliggör selektiv och känslig detektion av metylradikaler, vilket ger djupare insikter i de kemiska processerna inom DBD-reaktorer och bidrar till utvecklingen av mer effektiva och hållbara industriella tillämpningar.

Tillsammans driver dessa innovationer inom laserdiagnostik och optiska mättekniker inte bara gränserna för vetenskaplig förståelse, utan bidrar också direkt till utvecklingen av framtidens energisystem. Dessa system lovar att vara mer effektiva, hållbara och kapabla att möta de globala energifrågorna under de kommande decennierna.

Introduction

This report, by its very length,
defends itself against the risk of being read.
–Winston Churchill

This thesis is part of two interconnected research projects: the first focuses on the development of phosphor thermometry for high-temperature surface measurements, while the second involves the development and application of advanced optical techniques for the study of non-thermal plasmas.

Both projects focus extensively on utilizing laser diagnostics and optical measurement techniques to study the temporal response laser induced signals. Laser diagnostics have become indispensable tools across a wide array of scientific and industrial applications [1]. Their non-invasive nature makes them particularly valuable in environments where traditional physical probes may alter the system being studied, where access is physically constrained or where there exist no other way of obtaining information about the physical system under study. These optical techniques encompass a broad spectrum of methodologies and are extensively used to measure parameters such as temperature, molecular composition, flow velocities, and dimensional scales in various mediums [2]. The adaptability of optical and laser techniques allows for a diverse range of measurement formats, including point measurements (0D), line measurements (1D), planar measurements (2D), volumetric measurements (3D), and time-resolved studies, each tailored to meet specific experimental or industrial needs [3, 4].

The first part of the project concerns the development of high temperature phosphor thermometry for surface temperature measurements in hydrogen powered gas turbines [5]. Surface temperature measurement can be performed through various methods, including thermocouples and infrared (IR) cameras [6, 7, 8]. However, this thesis concentrates on laser-induced phosphor thermometry, a method favored for its ability to remotely measure temperatures with minimal intrusion [9]. In this technique, a phosphor coating is applied to the target surface. Upon excitation by a laser pulse, the phosphor emits light, known

as phosphorescence. The temperature of the surface is inferred by analyzing how the characteristics of this phosphorescence specifically, its spectral and temporal properties change with temperature.

Temperature-dependent spectral changes may appear as changes in the intensity of emission lines within the phosphorescent spectrum or as shifts in the wavelengths of these lines. Additionally, the duration of the phosphorescence, known as its lifetime, generally decreases as temperature rises, offering precise means for temperature determination [9, 10].

The phosphors utilized in this method are typically inorganic ceramics, often doped with trivalent lanthanide ions or trivalent transition metals. The first part of this thesis concentrates on the development of high-temperature phosphor thermometry, beginning with an introduction to the key concepts of thermographic phosphors. It then details the research conducted in this thesis on the development and characterization of these high-temperature phosphors [11]. The primary focus is on the spectral and temporal characterization of thermographic phosphors as a function of temperature, with an emphasis on temporal characterization, as this technique is better suited for high-temperature measurements [12].

The second part of this thesis focuses on the development of laser-based and optical diagnostic techniques for studying plasmas [13]. Plasmas consist of charged particles, including electrons, ions, and neutral species, which interact in complex, non-linear ways under very fast time-scales, see Figure 0.1 and are highly sensitive to external conditions. The rapid fluctuations in temperature, density, and electromagnetic fields within a plasma pose significant challenges to obtaining accurate, stable, and instantaneous measurements. Moreover, the high-energy environment and the potential for strong electromagnetic interference make conventional diagnostic tools, such as physical probes, less effective or unsuitable for these studies.

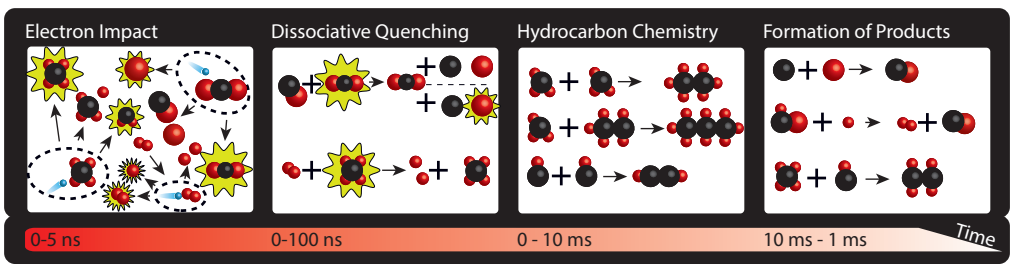

Figure 0.1: Illustration of different reaction mechanisms that can occur in a hydrocarbon plasma, this thesis focuses on two leftmost panels.

Laser diagnostics provide an effective solution to the challenges of measuring physical parameters in plasma [14, 15, 16]. By employing focused, coherent light, lasers can probe the dynamic and often inaccessible regions of a plasma with minimal disturbance [17]. Techniques such as laser-induced fluorescence, Rayleigh scattering, and interferometry enable

precise measurements of critical plasma properties, including temperature, density, and velocity distributions. These methods allow for non-intrusive, high-resolution diagnostics that can capture the rapid changes and complex interactions occurring within a plasma [18]. The ability to measure these properties with high accuracy is particularly important in understanding and controlling plasma behavior in various applications [19, 20].

Using laser diagnostics in plasma environments presents significant challenges, especially due to the presence of luminous backgrounds and scattering [21]. Plasmas often emit intense, broad-spectrum light that can interfere with laser-induced signals, complicating the isolation and accurate quantification of measurements [22]. This research focuses on non-thermal plasmas, where electrons have much higher temperatures than ions and neutral gas molecules, leading to an uneven energy distribution. The high energy of electrons, in contrast to the lower energy of heavier particles, complicates the quantification of fluorescence signals [17]. Moreover, the stochastic nature of plasma discharges, such as those in a gliding arc, further complicates the identification of precise measurement locations from a single measurment point.

To address these challenges, this thesis develops spatio-temporal measurement techniques, combining new approaches with existing methods. Fluorescence Lifetime Imaging (FLI) has been developed to perform quenching-corrected imaging, enabling the acquisition of quantitative fluorescence data [23, 24]. This technique was demonstrated in a highly scattering environment and subsequently applied to obtain quenching-corrected imaging of OH radicals in a gliding arc plasma [13]. To verify measurement locations within the plasma, 3D emission tomography was combined with fluorescence imaging of OH, providing spatially resolved fluorescence signals of OH relative to the plasma, allowing for a detailed study of both the OH distribution and the overall plasma structure [25]. Additionally, Rayleigh thermometry using structured illumination was integrated with OH fluorescence imaging to investigate gas heating in relation to the fluorescence signal. Finally, a novel method for photofragmentation imaging of methyl radicals in a plasma was demonstrated [26].

Theoretical Foundation

If you're going through hell, keep going.
–Winston Churchill

This thesis applies advanced spectroscopic and laser diagnostic techniques in plasma and combustion systems to determine key parameters such as temperature, species concentration, and plasma dynamics. The theoretical framework relies on light-matter interactions, allowing the extraction of physical information from how light interacts with the system under study. This chapter introduces and discusses the relevant theoretical concepts underpinning the thesis.

1 Quantum Mechanical Systems

Quantum physics, the fundamental theory describing the behavior of matter and energy at the smallest scales, provides a comprehensive framework for understanding atomic and molecular systems. Central to this theory is the energy quantization, a concept that underpins much of modern atomic and molecular physics [27].

1.1 Schrödinger equation

The concept of energy quantization arises from the solutions to the Schrödinger equation, which describes how the quantum state of a system evolves over time [28]. For an electron in an atom, the time-independent Schrödinger equation is:

$$\hat{H}\psi = E\psi \tag{1.1}$$

where $\hat{H}$ is the Hamiltonian operator, ψ is the wavefunction of the system, and E is the energy eigenvalue. The Hamiltonian operator for a single particle in a potential $V(r)$ is [29]:

$$\hat{H} = -\frac{\hbar^2}{2m}\nabla^2 + V(r) \tag{1.2}$$

In the context of atomic and molecular physics, solving the Schrödinger equation provides the energy levels and corresponding wavefunctions of electrons, nuclei, and their combinations [30].

1.2 Atomic Energy Levels

In the simplest case, such as for the hydrogen atom, the solutions to the potential $V(r)$ is the Coulomb potential due to the nucleus [28]:

$$V(r) = -\frac{Ze^2}{4\,\pi\,\epsilon_0\,r} \tag{1.3}$$

Solving the Schrödinger equation for this potential provides the energy levels for hydrogen-like systems, which are systems with a single electron [27]:

$$E_n = -\frac{Z^2 e^4 m_e}{8\,\epsilon_0^2 h^2 n^2} = -\frac{13.6\text{ eV} \cdot Z^2}{n^2} \tag{1.4}$$

where n is the principal quantum number, Z is the atomic number, and m_e is the electron mass. The solutions to the Schrödinger equation also provide the wavefunctions ,ψ, or orbitals, which encapsulates all the information about a system's quantum state, including aspects like positional probability, energy, and momentum, depending on the representation used. These wavefunctions are characterized by a set of quantum numbers [29]:

1. **Principal Quantum Number** (n): Determines the energy level and size of the orbital. It can take positive integer values (1, 2, 3, ...).
2. **Azimuthal Quantum Number** (l): Related to the angular momentum of the electron. It can take integer values from 0 to $n-1$. Each value of l corresponds to a different subshell (s, p, d, f).
3. **Magnetic Quantum Number** (m_l): Determines the orientation of the orbital in space. It can take integer values from $-l$ to $+l$.
4. **Spin Quantum Number** (m_s): Describes the intrinsic spin of the electron. It can take values of $+\frac{1}{2}$ or $-\frac{1}{2}$.

These quantum numbers define the unique state of an electron in an atom [30]. The Pauli exclusion principle states that no two electrons in an atom can have the same set of quantum numbers, which leads to the structure of the electron shells and subshells [27]. For multi-electron atoms, the situation becomes more complex due to electron-electron interactions and relativistic effects. Advanced theoretical models, such as Hartree-Fock and density functional theory, are used to approximate these interactions and predict the energy levels of more complex atoms [31].

1.3 Molecular Energy Levels

In molecules, the situation becomes even more intricate due to the presence of multiple nuclei. Molecular energy levels arise from electronic, vibrational, and rotational states [27]. The Born-Oppenheimer approximation simplifies the problem by assuming that the nuclear motion is much slower than the electronic motion, allowing the separation of the electronic and nuclear components of the Schrödinger equation [29].

Electronic States

The electronic energy levels of molecules are derived from molecular orbitals formed by the linear combination of atomic orbitals (LCAO). The resulting molecular orbitals are classified as bonding, anti-bonding, or non-bonding, depending on their energy and the nature of the electron distribution [30]. The electronic Schrödinger equation for a molecule, with fixed nuclei, is:

$$\hat{H}_{\text{electronic}}\,\psi_{\text{electronic}} = E_{\text{electronic}}\,\psi_{\text{electronic}} \tag{1.5}$$

where $\hat{H}_{\text{electronic}}$ includes the kinetic energy of electrons and the Coulomb interactions between electrons and nuclei [31]. The solutions provide the electronic energy levels $E_{\text{electronic}}$, which determine the chemical properties and reactivity of the molecule [27].

Vibrational States

Superimposed on the electronic energy levels are vibrational energy levels, resulting from the quantized vibrations of the nuclei within the molecule. Each electronic state has a series of vibrational levels, described by quantum number v [29]. While the harmonic oscillator model provides a first approximation, real molecular vibrations are better described by the anharmonic oscillator model [30]. The anharmonic vibrational Schrödinger equation for a diatomic molecule is:

$$\left(-\frac{\hbar^2}{2\mu}\frac{d^2}{dR^2} + V_{\text{vib}}(R)\right)\chi_v(R) = E_v\,\chi_v(R) \tag{1.6}$$

where μ is the reduced mass, R is the internuclear distance, χ_v is the vibrational wavefunction, and $V_{\text{vib}}(R)$ is the anharmonic potential, often modeled by the Morse potential [30]:

$$V_{\text{vib}}(R) = D_e\left(1 - e^{-a(R-R_e)}\right)^2 \tag{1.7}$$

Here, D_e is the dissociation energy, a is a parameter related to the well width, and R_e is the equilibrium bond length. The vibrational energy levels are then approximately [30]:

$$E_v = \left(v + \frac{1}{2}\right)\hbar\omega_e - \left(v + \frac{1}{2}\right)^2 \hbar\,\omega_e\,x_e \tag{1.8}$$

where ω_e is the harmonic vibrational frequency, and x_e is the anharmonicity constant. The anharmonic term accounts for the deviations from purely harmonic behavior, providing more accurate energy predictions [27].

Rotational States

Additionally, rotational energy levels are superimposed on the vibrational states and arise from the rotation of the molecule as a whole [27]. These levels are described by:

$$\left(-\frac{\hbar^2}{2I}\frac{d^2}{d\theta^2}\right) Y_{Jm}(\theta,\phi) = E_J Y_{Jm}(\theta,\phi) \tag{1.9}$$

where I is the moment of inertia, Y_{Jm} are the spherical harmonics and θ, ϕ are the rotational angles. The rotational energy levels, including centrifugal distortion, are [30]:

$$E_J = B_e J(J+1) - D_e J^2 (J+1)^2 \tag{1.10}$$

where B_e is the rotational constant and D_e is the centrifugal distortion constant. The term $-D_e J^2(J+1)^2$ accounts for the anharmonicity in rotational motion due to the non-rigidity of the molecule [27]. An example of the molecular energy levels is shown in Figure 1.1.

1.4 Transition Probabilities and Selection Rules

The probability of an electron transitioning between energy levels is governed by the transition dipole moment and selection rules derived from quantum mechanics [29]. The transition dipole moment μ is given by:

$$\mu_{if} = \langle \psi_f | \, \hat{\mu} \, | \psi_i \rangle \tag{1.11}$$

where ψ_i and ψ_f are the initial- and final-state wave functions, and $\hat{\mu}$ is the dipole moment operator. The square of the magnitude of the transition dipole moment determines the transition probability [27].

Selection rules specify the allowed transitions between quantum states based on the conservation of angular momentum and parity. For electric dipole transitions in atoms, the key selection rules are as follows [27]:

1. **Change in Angular Momentum** (Δl): The change in the azimuthal quantum number must be $\Delta l = \pm 1$.

2. **Change in Magnetic Quantum Number** (Δm_l): The change in the magnetic quantum number can be $\Delta m_l = 0, \pm 1$.

3. **Change in Spin** (Δs): The spin quantum number remains unchanged ($\Delta s = 0$).

These rules determine which transitions are allowed or forbidden. For example, in the hydrogen atom, transitions between the 1s and 2p orbitals are allowed ($\Delta l = 1$), while transitions between the 1s and 2s orbitals are forbidden ($\Delta l = 0$) and is therefore highly improbable [28]. When electrons transition between different internal states in an atom or molecule, a photon is emitted. The energy of this photon corresponds to the difference between the initial and final energy levels of the electron [30].

$$E_{\text{photon}} = h\nu = E_{\text{Initial}} - E_{\text{Final}}. \tag{1.12}$$

This energy difference, and hence the emitted photon, is unique for each atomic and molecular system and hence acts as a finger print for the molecule or atom under study. The temporal and spectral characteristic from this photon reveals physical characteristics about the system under study.

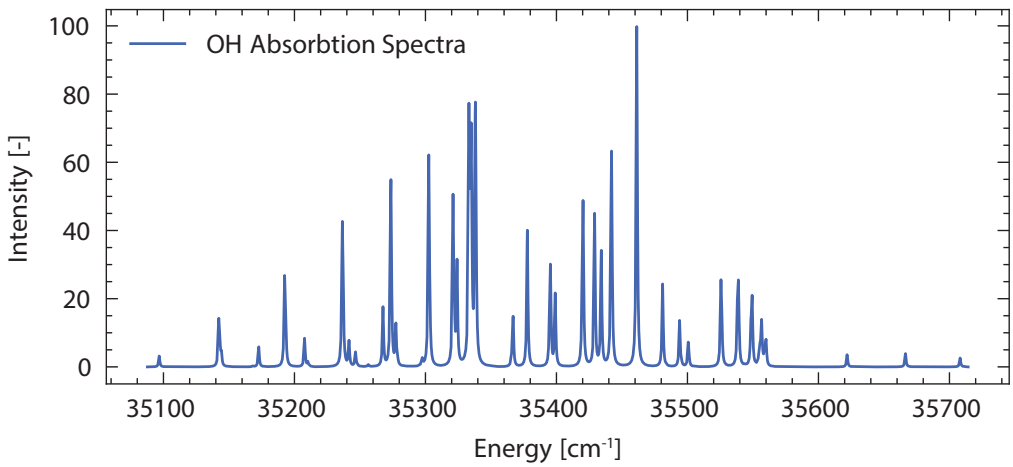

Figure 1.1: Simulated molecular absorption diagram of Hydroxyl radical (OH) at 300 K using the LIFBASE simulation software. The x-axis displays the energy in inverse centimeters and the y-axis represents the intensity of energy the transition.

2 Light-Matter Interaction in the Context of Laser Diagnostics

Light-matter interaction is fundamental to laser diagnostics, where laser light interacts with matter to reveal detailed information about a sample's properties. These interactions include absorption, scattering, emission, and nonlinear effects, each providing unique insights into the sample [32].. This chapter will explore the most common interactions, with more focus on those most relevant to this thesis which include fluorescence, phosphorescence and Rayleigh scattering.

2.1 Absorption

Absorption is a fundamental process where photons are absorbed by atoms or molecules, causing transitions between energy levels. This process is governed by quantum mechanics and is described by the Beer-Lambert Law, which relates the intensity of absorbed light to the concentration of absorbing species and the path length through the sample. When light of a specific wavelength passes through a sample, certain photons are absorbed if their energy matches the energy difference between two electronic states of the atoms or molecules in the sample [33]. This can be described as:

$$I = I_0 e^{-\alpha c L} \tag{2.1}$$

where I is the transmitted light intensity, I_0 is the incident light intensity, α is the absorption coefficient, c is the concentration of absorbing species, and L is the path length. There exist various diagnostic methods that exploit this phenomenon, but in principle, absorption spectroscopy is used to measure the concentration of specific species [34]. By tuning the laser to the absorption wavelength of the species of interest, the amount of absorbed light can be quantified, providing information about the species concentration [35].

2.2 Scattering

Scattering occurs when light interacts with particles, causing the light to be redirected in different directions. There are several types of scattering relevant to laser diagnostics, each capable of providing different types of information about the sample [34].

Rayleigh Scattering

Rayleigh Scattering involves the elastic scattering of light by particles much smaller than the wavelength of the incident light. Rayleigh scattering occurs due to the electric polarizability

of particles. The oscillating electric field of a light wave induces movement in the charges within a particle, causing it to oscillate at the same incident frequency. This transforms the particle into a small radiating dipole, which we observe as scattered light [36]. This process is highly dependent on the wavelength of the incident light and the properties of the scattering particles. Rayleigh scattering occurs when the diameter of the scattering particles is significantly smaller than the wavelength of the incident light, typically less than one-tenth, which is well satisfied for atoms and molecules in plasma and combustion processes [36]. For molecules the intensity of the scattered light (I) is proportional to the square of the induced dipole moment and can be expressed as:

$$I = I_0 \frac{8\,\pi^4 \alpha^2}{\lambda^4 r^2} \left(\frac{1 + \cos^2 \theta}{2} \right). \tag{2.2}$$

The polarizability (α) of a molecule depends on its electronic structure and can vary significantly between different molecules. Factors influencing molecular polarizability include:

1. Larger molecules generally have higher polarizability because their electron clouds are more easily distorted [29].
2. Molecules with delocalized electrons tend to have higher polarizability.
3. The orientation of anisotropic molecules relative to the electric field can affect the induced dipole moment.

Mie Scattering

Mie scattering occurs when the particles interacting with the incident light are of similar or larger size to the wavelength of the light. This can range from a few nanometers to several micrometers. The angular distribution of Mie scattering is more complex than Rayleigh scattering. The intensity of scattered light varies with the angle θ and can exhibit forward, backward, and side scattering peaks [37]. This is described by the differential scattering cross-section ($\frac{\partial \sigma_s}{\partial \Omega}$), which depends on the Mie coefficients [33].

Raman Scattering

Raman scattering happens when incident photons interact with a material, resulting in energy being transferred between the photons and the vibrational and/or rotational states of the molecules in the material [38]. Unlike Rayleigh scattering, where scattered photons have the same energy as the incident photons, Raman scattering involves a shift in the

energy of the scattered photons, corresponding to the energy difference between initial and final molecular states. The Raman effect involves two different types of scattering events: Stokes scattering occurs when a photon loses energy to a molecule, resulting in a scattered photon with lower energy and a longer wavelength than the incident photon. In contrast, anti-Stokes scattering happens when a photon gains energy from a molecule, leading to a scattered photon with higher energy and a shorter wavelength than the incident photon. The energy difference between the incident and scattered photons, known as the Raman shift, corresponds to the vibrational or rotational transitions in the molecule. This shift is also species specific, meaning that every molecule has a unique Raman shift. The Raman scattering cross-section is generally much smaller than that of Mie and Rayleigh scattering, making Raman signals weaker and requiring more sensitive detection techniques [39].

2.3 Emission

Emission processes involve the release of photons from excited states of atoms or molecules as they return to lower energy states. This emitted light can be analyzed to determine physical properties of the probed sample.

Fluorescence

Fluorescence happens when a molecule or atom absorbs light at a specific wavelength, exciting an electron to a higher energy state, see Figure 2.1. The electron then returns to a lower energy state, emitting a photon in the process. This emitted light, or fluorescence, has the same or longer wavelength (lower energy) than the absorbed light due to non-radiative relaxation processes within the excited state [40].

For a complete description of the system, the time-dependent intensity of the laser-induced fluorescence (LIF) signal can be described as:

$$I_{LIF}(t) = \sum_{v,j} N_{n\,(v',j')}(t) \sum_{v,j} A_{n\,(v',j')\rightarrow k\,(v,j)}. \tag{2.3}$$

Here, $N_{n(j',v')}$ represents the population of the excited state n at a specific vibrational (v') and rotational (j') level. The term $A_{n(v',j')\rightarrow k(v,j)}$ denotes the Einstein coefficient for spontaneous emission for the transition from the excited state $n(v',j')$ to the lower state $k(v,j)$. The most commonly discussed non-radiative energy transfer process affecting quantitative fluorescence data is collisional quenching, Q [40]. Collisional quenching is highly dependent on temperature and the ambient collisional partner molecules [34].

$$I_{LIF}(t) = N_n(t)\, A_{n\to k}. \tag{2.4}$$

For such a system, the average quenching rate can be calculated by summing the products of the species-specific quenching rate coefficient, k_{Qi}, and the number density of each species, N_i:

$$Q = \sum_i k_{Qi}\, N_i. \tag{2.5}$$

The relative velocity of the colliding species will affect quenching rate for a given collision. Hence the quenching rate coefficient depends on the colliding velocity of and the cross-section of the colliding species.

$$k_{Qi} = \langle v_i(\,T)\rangle\, \sigma_{Qi}(\,T) \tag{2.6}$$

$\sigma_{Qi}(T)$ represents the temperature-dependent quenching cross-section. For a thermalized system, the collision velocity can be derived from Boltzmann theory:

$$\langle v_i(\,T)\rangle = \sqrt{\frac{8k_BT}{\pi\mu}}. \tag{2.7}$$

Only a fraction of the excited molecules contribute to the fluorescence signal through spontaneous emission, and in a defined two-level system, the fluorescence quantum yield is expressed as:

$$\Phi = \frac{A_{nk}}{A_{nk} + Q_{nk}}. \tag{2.8}$$

By considering the excited and lower states as effective energy levels in a two-level system, the rate equation becomes:

$$\frac{d}{dt}N_n(t) = -N_n(t)(A_{n\to k} + Q_{n\to k}), \tag{2.9}$$

which has the solution:

$$N_n(t) = N_n \exp\left(-\frac{t}{\tau}\right). \tag{2.10}$$

This equation describes the change in population in state n over time with a decay constant $\tau = (A_{n\to k} + Q_{n\to k})$. For a given molecular system, if $A_{n\to k}$ is known, the quenching rate $Q_{n\to k}$ can be determined using a sufficiently short pulsed laser [41].

Phosphoresence

Phosphorescence is another luminescence phenomenon which involves the emission of light from a material following absorption of photons or electrons, but with a significant delay due to the involvement of triplet states [40].

When a molecule absorbs a photon and transitions to an excited singlet state (S_1), unlike fluorescence, where the molecule directly returns to the ground state (S_0), phosphorescence involves intersystem crossing (ISC) to an excited triplet state (T_1). The molecule then emits a photon with a delay as it returns to the ground state, see Figure 2.1. This delay is due to the quantum mechanically forbidden transition from the triplet state to the singlet ground state, resulting in a much slower process [42].

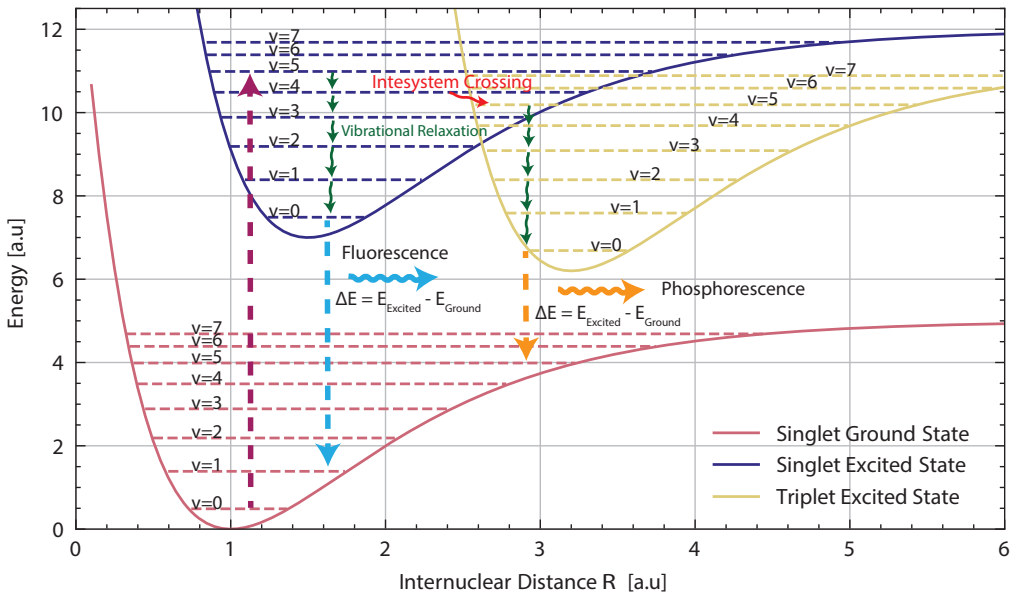

Figure 2.1: Illustration of electronic and vibrational energy diagram showing the physical mechanisms of fluorescence and phosphorescence.

Phosphorescence decay generally exhibits a multi-exponential behavior due to the complexity of the de-excitation processes involved [43]. In contrast to fluorescence, which generally exhibits a single- or double-exponential decay from excited singlet states to the ground state, phosphorescence involves transitions from excited triplet states, characterized by different lifetimes and decay pathways.

Several factors contribute to this multi-exponential decay. The triplet state often comprises multiple sub-levels, each with distinct lifetimes. Additionally, the local environment, including the presence of quenchers and the surrounding matrix, can significantly influence these lifetimes. Intersystem crossing from singlet to triplet states also vary, adding to the complexity. Furthermore, non-radiative deactivation processes such as internal conversion and vibrational relaxation introduce additional decay components [40]. As a result, the phosphorescence decay curve is typically a sum of several exponential terms, each representing a different decay pathway or mechanism [43].

Emission Spectra

When atoms or molecules absorb energy, electrons are excited to higher energy levels. Some of these electrons return to their ground state which results in the emission of photons, with wavelengths characteristic of the specific energy transitions involved. This phenomenon is the basis for emission spectroscopy, where the emitted light is analyzed to identify and quantify the elements or compounds present in a sample [44].

Emission spectra can be broadly categorized into continuous, line, and band spectra, see Figure 2.2. Continuous spectra arise from solids, liquids, or densely packed gases where numerous closely spaced energy levels are available. In contrast, line spectra are characteristic of isolated atoms in gaseous states, where distinct energy levels result in sharp, well-defined spectral lines [28]. Band spectra are associated with molecules and are comprised of closely spaced lines that appear as bands, resulting from rotational and vibrational transitions in addition to electronic transitions.

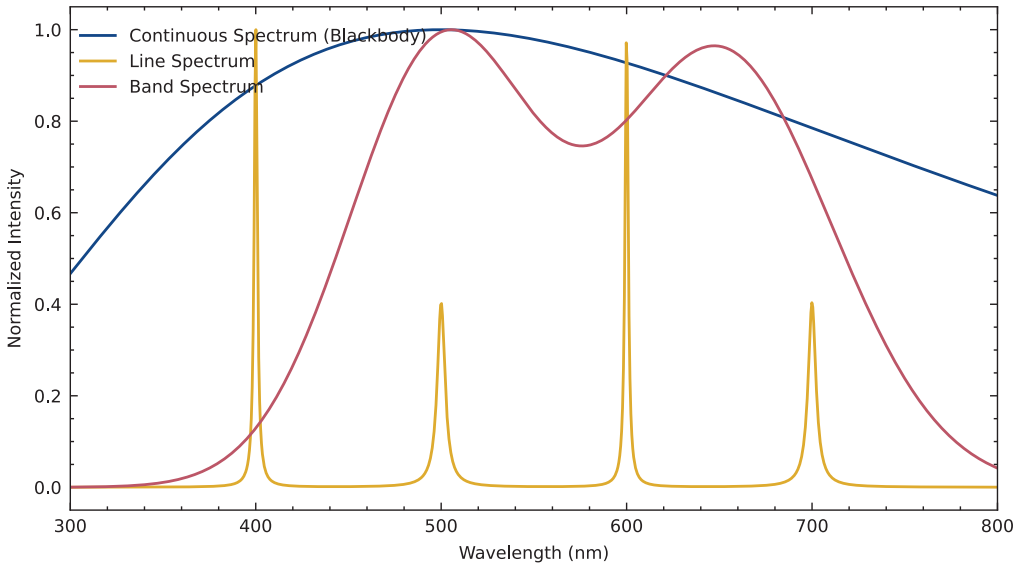

Figure 2.2: Simulated spectras that represent continuous, line and band spectra.

2.4 Non-linear Effects

Non-linear effects arise when a medium's response to a laser's electromagnetic field is not directly proportional to the field intensity. At high laser intensities, the electric field can induce higher-order polarization in the medium, making these non-linearities significant [45]. Non-linear optics encompasses a range of phenomena resulting from the interaction of high-intensity laser fields with a medium, including the generation of new frequencies, modulation of the refractive index, and other complex behaviors [46].

The polarization P of a medium in response to an electric field E can be described by a power series:

$$P = \epsilon_0 \left(\chi^{(1)} E + \chi^{(2)} E^2 + \chi^{(3)} E^3 + \dots \right) \tag{2.11}$$

Here, ϵ_0 is the permittivity of free space, and $\chi^{(n)}$ are the n-th order susceptibilities. The first term represents the linear response, while the higher-order terms account for non-linear effects [47]. Notable non-linear phenomena include:

1. **Second-Harmonic Generation (SHG)** is a second-order non-linear process where two photons at the same frequency ω combine to form a new photon at twice the frequency 2ω. This process requires a medium with a non-centrosymmetric crystal structure to allow the second-order susceptibility $\chi^{(2)}$ to be non-zero. SHG is

widely used in laser systems to generate coherent light at new wavelengths, enabling applications such as frequency doubling in laser systems [45].

2. **Third-Harmonic Generation (THG)** is a third-order non-linear process where three photons at the same frequency ω interact to produce a photon at 3ω. Unlike SHG, THG does not require a non-centrosymmetric material and can occur in a wider range of media, including gases, liquids, and solids [48]. Four-Wave Mixing (FWM) is a an example of a third order process Typically, two pump photons (ω_p) combine with a signal photon (ω_s) to produce an idler photon (ω_i), following the energy relation $2\omega_p = \omega_s + \omega_i$. FWM is widely used in spectroscopy, optical communications, and quantum applications [48].

3. **Coherent Anti-Stokes Raman Scattering (CARS)** is a third-order non-linear process that combines the benefits of Raman spectroscopy with the coherence and directionality of laser light. In CARS, a pump beam (ω_p) and a Stokes beam (ω_s) interact within a sample to produce a signal at the anti-Stokes frequency ($\omega_{as} = 2\omega_p - \omega_s$). The CARS signal is resonantly enhanced when the frequency difference $\omega_p - \omega_s$ matches a vibrational mode of the sample, making CARS a powerful tool for molecular fingerprinting and imaging [45].

The efficiency of harmonic generation depends on the non-linear susceptibility ($\chi^{(2)}$ for SHG and $\chi^{(3)}$ for THG) of the material [46]. Materials with high non-linear coefficients are preferred for generating strong harmonic signals. Moreover, the efficiency of harmonic generation is significantly influenced by phase matching of the incident waves, and in practice, achieving phase matching involves careful selection of the nonlinear medium and the wavelengths of the interacting waves to satisfy the phase matching condition [47].

3 Line Broadening

The width of an absorption line depends on several physical phenomena, some influenced by local temperature variations and ambient molecules. The linewidth function $g(\omega)$, expressed in terms of angular frequency, is given in Equation 3.1. The linewidth affects the spectral overlap of the wavelength distributions of the laser and the target species which then in turn the number of excited molecules. The properties of natural, collisional, Doppler and Stark broadening are discussed below.

3.1 Natural linewidth

Natural linewidth of an absorption line depends on the uncertainty of the two energy levels involved in the transition [34]. The natural linewidth arises due to the inherent quantum

mechanical uncertainty in the energy levels of the molecules involved in the transition. This uncertainty is inversely proportional to the lifetime of the excited state, meaning that shorter-lived states have broader natural linewidths. Without other line broadening effects, the spectral line shape is:

$$g(\omega) = \frac{1}{2\pi} \frac{\Gamma}{(\omega - \omega_{ba})^2 + \left(\frac{\Gamma}{2}\right)^2} \tag{3.1}$$

This Lorentzian function, where ω_{ba} is the center angular frequency of the absorption line and Γ is the full width at half maximum (FWHM) of the linewidth function, represents the inverse of the excited state's lifetime (assuming the lower state is stable) [49]. Natural linewidth is also independent of external conditions such as pressure and temperature, making it a reliable reference for calibrating and interpreting spectroscopic data. However, in real-world applications at atmospheric pressure and above, other broadening mechanisms such as Doppler and collisional broadening often dominate.

3.2 Collisional broadening

Collisional broadening becomes significant higher pressures. Both natural and collisional broadening are examples of homogeneous broadening, where all molecules in the probe volume have the same probability of being affected by the electromagnetic field. In natural broadening, energy level precision is determined by state stability, which is perturbed by molecular collisions at higher pressures. Collisions disrupt the coherence formed in the statistical ensemble of molecules, affecting state stability [49]. The line shape of collisionally broadened molecules can also be described by a Lorentzian function with a larger Γ, as collisions decrease the lifetime.

3.3 Doppler broadening

Doppler broadening occurs due to the relative motion between the laser light and the absorbing or emitting molecules which is highly dependent on the reference frame of you measurement. This motion causes a shift in the frequency of the light experienced by the molecules, known as the Doppler effect. This results in varying excitation probabilities among molecules in the probe volume, making Doppler broadening an inhomogeneous broadening effect. Molecules in a gas phase move with a distribution of velocities according to their temperature. As a result, the absorption or emission lines of these molecules broaden into a Gaussian profile because molecules moving towards the light source experience a blue shift, while those moving away experience a red shift [34]. The resulting line shape is given by:

$$g_D(\omega) = \frac{1}{\sqrt{\pi}\Delta\omega_D} e^{-\left(\frac{\omega-\omega_{nm}}{\Delta\omega_D}\right)^2} \tag{3.2}$$

where $\Delta\omega_D = \omega_0\sqrt{\frac{2k_BT}{mc^2}}$ is the FWHM of the Doppler-broadened spectral peak. Doppler broadening depends on local temperature and pressure variations. Doppler broadening dominates at low pressures where collisional broadening is minimal. In such conditions, the linewidth is primarily determined by the thermal motion of the molecules. However, as pressure increases, collisional broadening starts to contribute more significantly, and the combined effect often results in a Voigt profile, a convolution of Lorentzian (collisional) and Gaussian (Doppler) line shapes.

3.4 Stark Broadening

Stark broadening occurs due to the Stark effect, where the presence of an external electric field causes the splitting and shifting of energy levels, resulting in the broadening of spectral lines. The extent of this broadening is directly related to the strength of the electric field and the density of charged particles in the medium.

Stark broadening is typically described using a quantum mechanical approach that considers the interaction of the electric field (from ions and electrons) with atoms or ions. The width of the Stark broadened line can be estimated using the following relation [50]:

$$\Delta\lambda_S = 2\left(\frac{e^3\lambda^2}{hc}\right)\left(\frac{N_e}{\epsilon_0 kT_e}\right)^{1/2} \tag{3.3}$$

where $\Delta\lambda_S$ is the Stark broadening width, and is often represented by a Lorentzian profile as shown in Equation (3.1).

In practical applications, empirical and semi-empirical formulas are often used. These formulas are derived from both theoretical models and experimental data, providing a way to relate the observed broadening to plasma parameters such as electron density and temperature.

4 Plasma physics

Plasma, often referred to as the fourth state of matter, is a quasi-neutral gas consisting of ions, electrons, and neutral particles. Plasmas are found naturally in stars, including the sun, and interstellar space and make up 99% of the visible universe. Unlike solids, liquids, and gases, plasmas are characterized by their unique properties, such as high electrical conductivity, sensitivity to magnetic fields, and the ability to sustain collective behaviors. These properties make plasmas integral to a wide range of natural phenomena and technological applications [51].

4.1 Plasma properties

Plasma's distinct behavior arises from the presence of free charged particles, ions and electrons which interact through long-range electromagnetic forces. This section introduces key plasma physics concepts relevant to this thesis, illustrating how these properties govern plasma dynamics and are often observed in various forms of gas discharges.

One fundamental feature of plasma is quasi-neutrality, where the densities of positive and negative charges are nearly equal on large spatial scales, ensuring overall electrical neutrality. However, on smaller scales, local charge imbalances can develop, creating electric fields that influence particle motion and are crucial in sustaining discharges [51].

Plasmas also exhibit collective behavior, in contrast to neutral gases, where short-range collisions dominate. In plasmas, long-range electromagnetic interactions cause particles to behave collectively, leading to phenomena such as plasma waves and instabilities. This collective behavior is a defining characteristic of plasmas and plays a key role in the formation of electrical discharges such as arcs, sparks, and glow discharges [51].

A key mechanism in plasma is Debye shielding, where a charged particle attracts opposite charges and repels like charges, forming a cloud of screening charges around it. The distance over which this screening occurs is defined by the Debye length (λ_D), given by:

$$\lambda_D = \sqrt{\frac{\epsilon_0 k_B T_e}{n_e e^2}}, \tag{4.1}$$

where ϵ_0 is the permittivity of free space, k_B is the Boltzmann constant, T_e is the electron temperature, n_e is the electron density, and e is the elementary charge. Beyond the Debye length, the electric field of a charged particle is effectively neutralized. Debye shielding is crucial in determining the stability and behavior of discharge plasmas, where local charge separations can lead to ionization fronts or sheath formation [51].

Another important parameter is the plasma frequency (ω_p), which describes the natural oscillation of the electron population. It is defined as:

$$\omega_p = \sqrt{\frac{n_e\, e^2}{\epsilon_0\, m_e}}, \tag{4.2}$$

where m_e is the electron mass [51]. These oscillations represent how electrons respond to displacement from equilibrium and are important in understanding how plasmas, especially those in discharge conditions, interact with electromagnetic fields.

Temperature and density are two additional parameters that define plasma states. Plasmas are typically characterized by high temperatures, where the thermal energy of particles is sufficient to ionize atoms. Electron temperature (T_e) and ion temperature (T_i) are often different, as ions and electrons exchange energy at different rates. In addition, plasma density refers to the number of charged particles per unit volume, and it affects the properties of gas discharges. Discharge plasmas can have a wide range of densities, from low-pressure glow discharges with densities around 10^9 cm^{-3}, to high-density arcs exceeding 10^{20} cm^{-3}. Both temperature and density significantly influence the behavior of discharge plasmas, affecting processes such as ionization, recombination, and wave propagation [51].

In plasma discharges, such as glow discharges, arc discharges, and capacitively coupled discharges, the balance between ionization, electric fields, and thermal energy defines their stability and characteristics. For instance, glow discharges operate at lower pressures and produce visible light through electron collisions, while arc discharges occur at higher currents and can sustain high-density plasmas due to intense ionization.

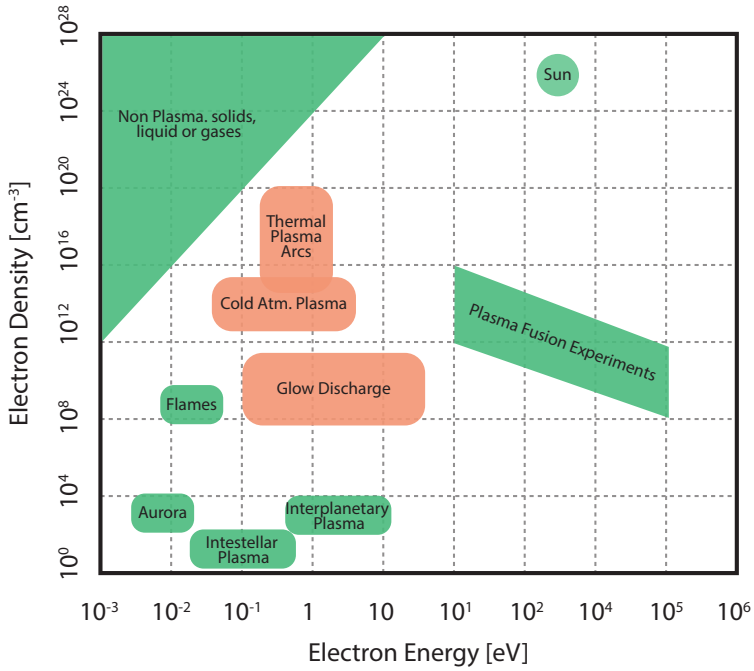

Figure 4.1: Common plasmas in the context of electron density and electron energy. The orange regions highlight the types of plasmas studied in this thesis. The region in the top left corner corresponds to bounded electrons.

4.2 Thermal and Non-Thermal Plasmas

To create plasma you need energy for ionization which can be supplied in various forms, such as electric fields, electric currents, electromagnetic waves, or thermal energy. Based on the energy distribution and pressure conditions, plasma can be broadly categorized into two main categories, thermal and non-thermal plasmas.

Thermal Plasmas

Thermal plasmas, also known as equilibrium plasmas, are characterized by the thermal equilibrium between electrons and heavy particles (ions and neutral atoms). In these plasmas, the temperature of electrons (T_e) is roughly equal to the temperature of ions (T_i) and the temperature of neutral atoms (T_n) [51]. Thermal plasmas typically occur at high pressures and temperatures, often reaching several thousand degrees Kelvin. Some common examples are [52]:

- **Arc Discharges:** Utilized in welding, cutting, and melting metals, where high temperatures are necessary to achieve the required thermal energy for processing.

- **Plasma Torches:** Employed in materials processing, including plasma spraying for coatings, waste treatment, and the synthesis of novel materials.
- **Electric Furnaces:** Used in the steelmaking industry, where thermal plasmas provide the intense heat needed to melt and refine metals.

Non-Thermal Plasmas

Non-thermal plasmas, also known as non-equilibrium plasmas, exhibit a significant temperature difference between electrons and heavy particle [51]. In these plasmas, the electron temperature (T_e) is much higher than the temperatures of ions (T_i) and neutral particles (T_n), which remain close to room temperature. Non-thermal plasmas typically form at low pressures or when energy is supplied over short time scales. These plasmas are notable for sustaining high-energy electrons without significantly heating the surrounding gas [52].

- **Glow Discharges:** Used in fluorescent lamps, neon signs, and plasma displays, where low-pressure conditions and non-thermal characteristics are essential for efficient light production.
- **Corona Discharges:** Employed in air purification, ozone generation, and surface treatment of materials, exploiting the ability of non-thermal plasmas to produce reactive species at low temperatures.
- **Dielectric Barrier Discharges (DBDs):** Applied in sterilization, biomedical treatments, and pollution control, the non-thermal nature is used to activate chemical processes without damaging heat-sensitive materials.

4.3 Plasma Dynamics

The temporal and spatial dynamics of plasma depend on its type, which necessitates different descriptive approaches. There are two primary approaches to describing a plasma: (i) treating the plasma as a fluid, where its motion is governed by electromagnetic, pressure, and viscous forces across space and time; and (ii) considering it as a collection of individual particles, with each particle's motion determined by electromagnetic forces acting on it independently. Additionally, plasma kinetics, involving the generation of new radicals and free charged particles, plays a crucial role. These kinetic processes, sharing similarities with chemical kinetics.

Plasma as a Fluid

The fluid approach, also known as the magnetohydrodynamic (MHD) approach. In this approach, the plasma is treated as a continuous medium rather than a collection of individual particles. This perspective simplifies the complex interactions within the plasma, allowing for a more tractable analysis of its macroscopic properties and dynamics with some basic assumptions [51, 53]:

- **Continuum and Quasi-Neutrality:** The plasma is treated as a continuous fluid, disregarding the discrete nature of its individual particles. This approximation holds when the relevant length scales are significantly larger than the mean free path of the particles [54]. Additionally, the plasma is often considered quasi-neutral, implying that the electron and ion number densities are approximately equal, which prevents large-scale electric charge separation [55].
- **Single or Multi-Fluid:** Depending on the level of detail required, the plasma can be described as a single fluid with averaged properties or as multiple fluids, each representing different species (e.g., electrons, ions) [56].

The fluid approach involves solving a set of coupled differential equations derived from the conservation laws of mass, momentum, and energy, along with Maxwell's equations for electromagnetism [51]. The fluid approach is particularly effective for studying large-scale, collective phenomena in plasmas, such as magnetospheric and solar wind dynamics, fusion plasma behavior, and industrial thermal plasma processes [53]. However, it has limitations when dealing with small-scale or high-frequency phenomena where kinetic effects and individual particle dynamics become significant. In such cases, a more detailed kinetic description, such as the Vlasov or Boltzmann equations, may be necessary [54].

Plasma as Particles

The particle approach, also known as the kinetic approach, provides a detailed description of plasma behavior by considering the motion and interactions of individual particles [51, 55]. Unlike the fluid approach, which treats plasma as a continuous medium, the particle approach accounts for the discrete nature of the constituent particles, such as electrons and ions. This method is particularly useful for studying phenomena that occur on small spatial and temporal scales, where individual particle dynamics and non-equilibrium effects are significant [56].

The state of the plasma is described by distribution functions $f_s(\mathbf{r}, \mathbf{v}, t)$, where s denotes the species (e.g., electrons, ions), $\mathbf{r}$ is the position, $\mathbf{v}$ is the velocity, and t is time. This distribution function represents the number density of particles in phase space. The evolution

of the distribution function depends on several parameters, primarily whether the plasma includes collisions between constituent particles or not [53].

- For collisionless plasmas, the evolution of the distribution function is governed by the Vlasov equation [54]:

$$\frac{\partial f_s}{\partial t} + \mathbf{v} \cdot \nabla_{\mathbf{r}} f_s + \frac{q_s}{m_s}(\mathbf{E} + \mathbf{v} \times \mathbf{B}) \cdot \nabla_{\mathbf{v}} f_s = 0$$

  where q_s and m_s are the charge and mass of species s, and $\mathbf{E}$ and $\mathbf{B}$ are the electric and magnetic fields, respectively.

- For collisional plasmas, the Boltzmann equation is used, incorporating a collision term $\left(\frac{\partial f_s}{\partial t}\right)_{\text{coll}}$ [53]:

$$\frac{\partial f_s}{\partial t} + \mathbf{v} \cdot \nabla_{\mathbf{r}} f_s + \frac{q_s}{m_s}(\mathbf{E} + \mathbf{v} \times \mathbf{B}) \cdot \nabla_{\mathbf{v}} f_s = \left(\frac{\partial f_s}{\partial t}\right)_{\text{coll}}$$

  The collision term accounts for interactions between particles, such as Coulomb collisions [56].

The particle approach provides a detailed description of particle dynamics, capturing non-equilibrium effects and fine-scale structures [55]. It accurately models collisional processes, crucial for many plasma applications, and is flexible, applicable to various plasma conditions and geometries [54]. However, this approach is computationally intensive, requiring significant resources to simulate large numbers of particles and resolve small-scale features, making large-scale simulations challenging to implement [51].

4.4 Discharge Plasma

The focus of this thesis is on discharge plasma, typically created by applying a high voltage that initiates gas breakdown and generates plasma. This process occurs when a neutral gas is ionized under the influence of an external electric field, transforming it into a partially ionized plasma. The study of discharge plasma physics explores the mechanisms behind ionization, primarily explained by Townsend and streamer theories, each describing different phases of the ionization process and breakdown phenomena. This section will give a brief overview of the physical mechanism and some limitations of the theories describing discharge plasma.

Townsend Theory

Townsend theory describes the process of ionization in gases under low electric fields, particularly during the early stages of discharge. When a sufficiently strong electric field is applied across a gas, free electrons are accelerated and collide with neutral atoms or molecules, leading to ionization. These collisions produce more electrons, leading to an electron avalanche. The number of ionizing collisions per unit distance traveled by an electron is characterized by the first Townsend ionization coefficient (α) [57]. This coefficient is defined as:

$$\alpha = A \exp\left(-\frac{B}{E}\right) \tag{4.3}$$

where A and B are empirical constants depending on the gas, E is the electric field strength. The total number of electrons generated by an avalanche starting with a single electron is given by:

$$N = e^{\alpha d} \tag{4.4}$$

where d is the distance traveled by the electron in the electric field. The avalanche process continues, leading to an increase in the current until the breakdown voltage is reached, and a self-sustaining discharge is established [57].

One limitation of Townsend theory is its assumption of uniform electric fields and a constant electron multiplication rate. It fails to accurately describe gas breakdowns in non-uniform fields, high pressures, or scenarios where space charge effects (from ions and electrons) significantly alter the local electric field.

Streamer Theory

Streamer theory extends Townsend's model by accounting for the effects of space charge produced by the growing avalanche. As the electron avalanche grows, a space charge region forms at the avalanche head due to the separation of positive ions and electrons. This leads to the formation of a highly localized electric field around the avalanche, further enhancing ionization in the vicinity of the avalanche head.

In streamer discharges, the local electric field (E_{local}) created by the space charge can exceed the applied field, leading to the rapid growth of the discharge. The development of a streamer can be modeled by considering the electron density (n_e) and the ionization rate (ν_i) [57]:

$$\nu_i = \alpha v_d \tag{4.5}$$

where v_d is the electron drift velocity and α is the ionization coefficient. The growth of the electron density is then given by:

$$\frac{dn_e}{dt} = \alpha v_d n_e \tag{4.6}$$

The space charge field generated by the accumulated ions at the avalanche head significantly enhances the local electric field, accelerating the breakdown process. Once the ionization front propagates through the gas, a conducting plasma channel (the streamer) is formed, enabling fast and localized breakdowns.

Streamer theory is particularly effective in explaining discharges at high pressures, where breakdown occurs much faster than predicted by Townsend theory. However, it still faces challenges in fully explaining the transition from the streamer phase to a fully developed arc discharge, where a stable conducting path is formed.

Breakdown and Paschen's Law

In the context of both theories, gas breakdown is typically analyzed using Paschen's law, which relates the breakdown voltage (V_b) to the product of gas pressure (p) and electrode separation (d) [57]:

$$V_b = \frac{Bpd}{\ln(Apd) - \ln\left(\ln\left(1 + \frac{1}{\gamma}\right)\right)} \tag{4.7}$$

where γ is the secondary emission coefficient, which accounts for ionization caused by ion collisions with the cathode. Paschen's law predicts the breakdown voltage in low-pressure gases but has limitations at very small or large pd values, where deviations from the law occur due to processes like field emission or the onset of streamers.

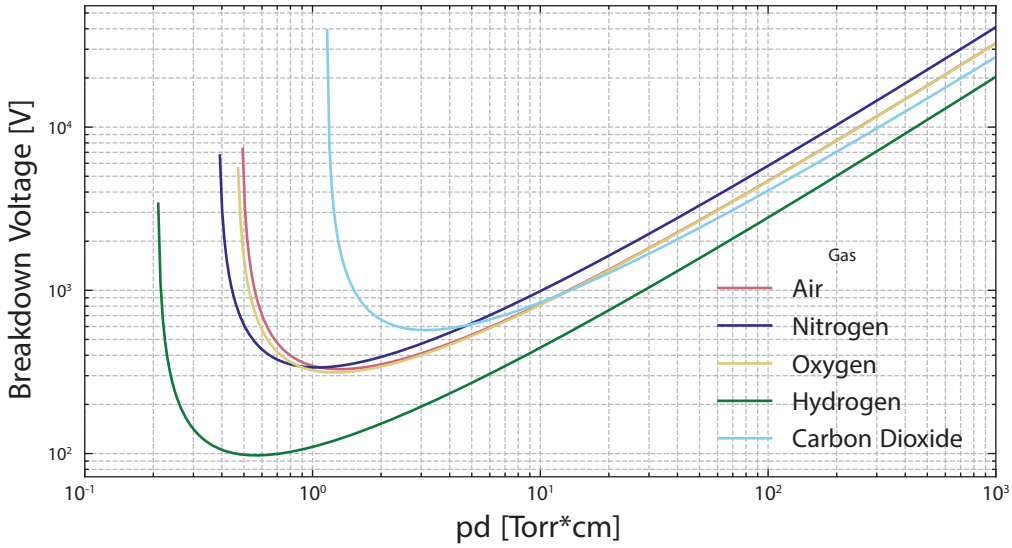

Figure 4.2: The graph shows the breakdown voltage as a function of the pressure-distance product (pd) for various gases. The breakdown voltage is calculated using equation (4.7), which relates the applied electric field, gas pressure, and electrode separation. The curves illustrate how the breakdown voltage varies for each gas, highlighting the minimum voltage required for ionization to occur and the gas-specific characteristics that influence this behavior. Constants taken from [58].

Limitations of Townsend and Streamer Theories

While Townsend theory successfully describes the initial stages of ionization, it falls short in explaining fast breakdowns in high-pressure or non-uniform electric fields. It also ignores the space charge effects that are crucial for the development of fast ionization fronts.

Streamer theory, on the other hand, explains fast discharges and the development of highly localized ionization regions in high-pressure gases. However, it does not fully capture the transition from streamers to a stable arc discharge, especially in scenarios involving complex gas mixtures or the interaction of multiple discharges. Additionally, both theories are limited in their ability to model non-local effects, such as the interaction of distant charge regions, and often require numerical or hybrid models to account for the full dynamics of plasma discharges.

4.5 Plasma Kinetics and Reactive Species Generation

In practical applications, plasmas are used to generate reactive species to treat surfaces or enhance chemical processes [59, 57]. Plasma kinetics is employed to study the dynamic processes within the plasma, including the generation, interaction, and decay of various species over time [51].

There are several ways a plasma can generate reactive species either via high-energy electrons colliding with neutral gas molecules, energy transfer between atoms/molecules, or interaction with photons leading to the formation of reactive species such as radicals, excited atoms, and ions. These reactive species are pivotal in enhancing chemical processes, particularly in non-thermal plasmas where the electron temperature is significantly higher than the gas temperature. Some notable reaction pathways are [59]:

- **Electron Impact Ionization:** $e^- + M \rightarrow M^+ + 2e^-$
- **Dissociation:** $e^- + AB \rightarrow A + B + e^-$
- **Excitation:** $e^- + M \rightarrow M^* + e^-$
- **Penning Ionization:** $A^* + B \rightarrow A + B^+ + e^-$
- **Photoionization:** $A + h\nu \rightarrow A^+ + e^-$

The temporal and spatial evolution of species in plasmas is described by plasma kinetics [59, 57]. Similar to chemical kinetics, plasma kinetics uses rate equations to model system behavior. However, unlike chemical kinetics, where reaction rates follow the Arrhenius expression, plasma kinetics depends on the cross-sections of colliding particles. These rates are derived from the Boltzmann equation, which provides the Electron Energy Distribution Function (EEDF) [51, 60]. The EEDF $f_e(\epsilon)$ represents the distribution of electron energies ϵ:

$$\int_0^\infty f_e(\epsilon)\, d\epsilon = 1 \tag{4.8}$$

Reaction rate coefficients (k) for processes like ionization, dissociation, and excitation can be calculated using the EEDF:

$$k = \int_0^\infty \sigma(\epsilon) v(\epsilon) f_e(\epsilon)\, d\epsilon \tag{4.9}$$

where $\sigma(\epsilon)$ is the cross-section of the reaction, and $v(\epsilon)$ is the velocity of electrons with energy ϵ. In thermal plasmas, the electron energy distribution follows a Maxwellian pattern, simplifying the analysis [59, 57]. However, in non-thermal plasmas, the EEDF deviates significantly from Maxwellian behavior and must be solved explicitly, which is computationally expensive [51], see Figure 4.3 for an example plasma simulation.

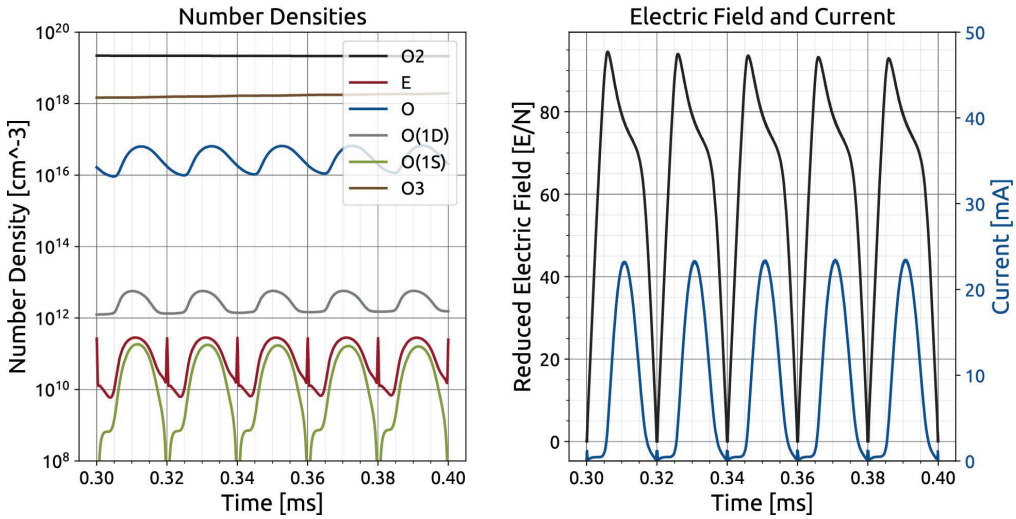

Figure 4.3: Simulation of an oxygen plasma using ZDPlaskin, which employs the Boltzmann equation to determine reaction rates. The left panel illustrates the temporal evolution of the major species, while the right panel displays the reduced electric field (electric field divided by the number density of neutral particles) and the current.

4.6 Plasma Reactors

Reactive species generated by plasma are critical in chemical engineering, as they accelerate or enable key reactions, making processes more energy-efficient or even possible [52, 59]. To maximize these benefits, it is essential to design and control plasma interactions to achieve optimal performance with the medium.

Non-thermal plasma offers significant advantages for chemical processing, primarily due to its ability to drive reactions under conditions that would be challenging or inefficient with traditional thermal methods. One of its main strengths is selective excitation and ionization [52, 57]. In non-thermal plasma, electrons can reach very high energies while not heating the surrounding gas. This allows for the initiation of energy-intensive reactions, such as breaking strong molecular bonds, without immediately heating the entire system, leading to greater energy efficiency. By maintaining low overall temperatures while generating high-energy electrons, non-thermal plasma processes consume less energy than methods that require heating large volumes of gas or material to high temperatures. Additionally, these energetic electrons facilitate the formation of reactive species like radicals, ions, and excited molecules, significantly enhancing reaction rates.

Plasma reactors are used to generate and sustain plasma under controlled conditions for various applications [52]. The type of plasma reactor employed strongly influences the concentration and distribution of reactive species, which depend on factors such as power input, gas composition, pressure, and reactor design [59, 57]. By fine-tuning these para-

meters, specific reactive species can be selectively produced and optimized for particular applications.

In this thesis, the Dielectric Barrier Discharge (DBD) and Gliding Arc discharge have been in focus, chosen for their simplicity and unique capabilities.

Dielectric Barrier Discharge (DBD) Reactors

Dielectric Barrier Discharge (DBD) reactors function by applying a high voltage across two electrodes, with at least one electrode covered by a dielectric material [52]. The dielectric barrier is essential in preventing the transition to a full arc discharge, thereby maintaining the plasma in a non-thermal state. This non-thermal state is advantageous because it allows the DBD reactor to generate a significant number of reactive species while keeping the gas temperature relatively low.

The electrode configuration typically involves either parallel plates or coaxial cylindrical electrodes, see example DBD reactor in Figure 4.4. The dielectric barrier, which can be made from materials such as glass, quartz, or ceramics, is selected based on the required breakdown voltage and the specific application of the reactor.

Plasma formation occurs when a high voltage is applied, leading to micro-discharges across the gas gap between the electrodes. These micro-discharges are usually transient and spatially distributed, resulting in a uniform plasma over the electrode surface [57]. The dielectric barrier plays a crucial role in limiting charge transfer, which quickly extinguishes the discharge and prevents the formation of a thermal arc.

The performance of a DBD reactor is highly dependent on several operational parameters. These include the type of dielectric material used, the gap between electrodes, the nature of the gas (such as air, argon, or nitrogen), and the applied voltage waveform, which could be sinusoidal or pulsed [52, 59].

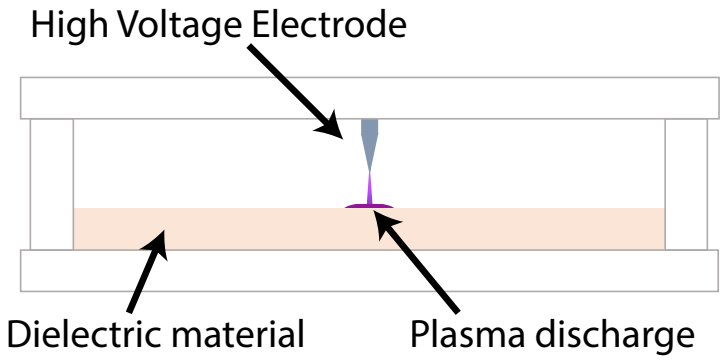

Figure 4.4: Illustration of a pin-to-plate DBD reactor with a single high-voltage electrode positioned at the top, designed to localize the discharge, making it ideal for studying plasma behavior.

Gliding Arc Reactors

Gliding Arc reactors represent a distinct class of non-thermal plasma reactors that operate on the principle of a stabilized arc discharge [52, 57]. Unlike Dielectric Barrier Discharge (DBD) reactors, which maintain the plasma in a non-equilibrium state through the use of a dielectric barrier, Gliding Arc reactors rely on the continuous movement of the arc itself to prevent the system from transitioning into a thermal equilibrium state and is highly dependent how the power supply deliver the power.

The reactor is equipped with two diverging electrodes between which an electric arc is initiated. This arc, being highly conductive, naturally seeks the shortest path between the electrodes. As the arc heats the surrounding gas, the gas flow between the electrodes the diverging geometry pushes the arc along the electrodes causing the arc to ”glide” along the electrodes, see Figure 4.5 [59].

The dynamic nature of the gliding arc is key to its operation. As the arc root continuously moves along the electrodes, it ensures that the arc remains in a non-equilibrium state. This movement is crucial as it allows the reactor to produce a wide range of reactive species at lower temperatures compared to conventional thermal arcs [52]. Their capacity to handle large volumes of gas and generate significant amounts of reactive species makes them suitable for both laboratory-scale studies and industrial applications. The efficiency of a Gliding Arc reactor is influenced by several design considerations. Key factors include the design of the electrodes, the dynamics of the gas flow, and the characteristics of the power supply [57].

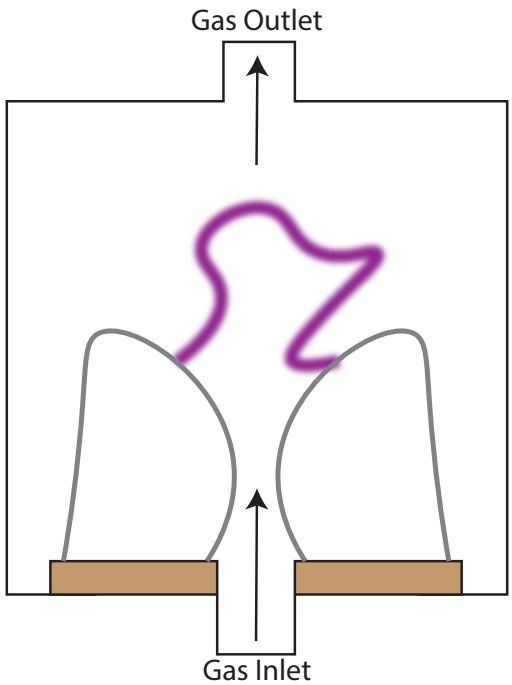

Figure 4.5: Illustration of a gliding arc reactor featuring two diverging electrodes, with a gas inlet positioned at the base of the electrodes and a gas outlet located at the top.

Optical Measurement Techniques

Success consists of going from failure to failure without loss of enthusiasm.
–Winston Churchill

Laser-based measurement techniques have revolutionized research and industry by offering precise, non-intrusive methods that support the development of novel technologies [61, 32]. This chapter describes and discusses the measurement techniques central to this thesis, including the experimental equipment and considerations involved.

5 Laser Systems and Detectors

The results presented in this thesis are significantly influenced by high-quality detectors and laser systems. This section provides a brief overview of the experimental equipment used and relevant considerations.

5.1 Laser Systems

This section presents a brief overview of fundamental concepts of laser pulse generation relevant to the research conducted in this thesis. It also includes a short description of the laser systems used [62].

Pulsed Lasers

Pulsed lasers produce short, intense bursts of light by accumulating energy in a laser cavity with a gain medium, which may be either gas or solid, rather than emitting a continuous beam [61]. The process begins with a pumping source, such as a flash lamp or another laser, that excites atoms in the gain medium to higher energy levels. The gain medium amplifies this light through stimulated emission. Techniques like mode-locking or Q-switching control the release of this stored energy, resulting in pulses typically lasting from femtoseconds to nanoseconds [62].

Q-Switching

Q-switched pulsed lasers generate intense, short bursts of light by modulating the quality factor (Q) of the laser's optical resonator [61]. The optical resonator, consisting of two mirrors, which contains and amplifies the light. The Q-switch controls the timing of light emission by switching between low-Q and high-Q states. During operation, the Q-switch initially maintains a low-Q state, allowing energy to accumulate in the gain medium. Once sufficient energy is stored, the Q-switch rapidly shifts to a high-Q state, releasing the energy as a high-intensity pulse [62]. These pulses typically last from a few nanoseconds to hundreds of nanoseconds.

Mode-Locking

Mode-locking is a technique used to generate ultrashort pulses of light, typically in the picosecond or femtosecond range, by causing the phases of different longitudinal modes of

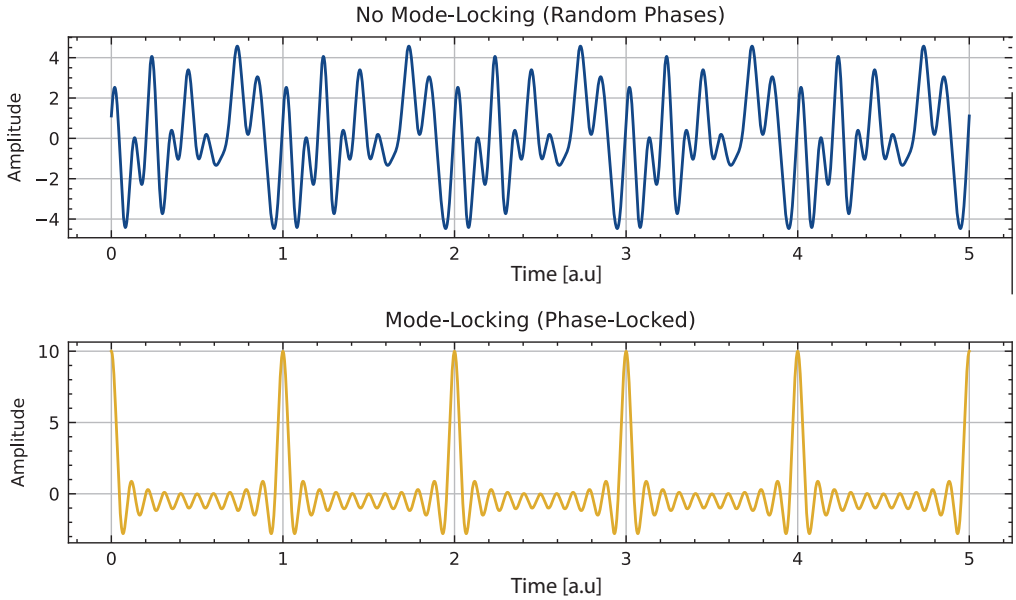

Figure 5.1: Comparison of the laser intensity output from multiple modes with and without phase-locking. The top plot shows the result when the modes have random phases (no mode-locking), leading to a continuous and irregular signal. The bottom plot shows the case where the modes are phase-locked (mode-locking), resulting in periodic, intense pulses.

a laser to lock together [32]. If the electric field of a single longitudinal mode is represented as $E_n(t) = E_n \cos(\omega_n t + \phi_n)$, where E_n is the amplitude, ω_n is the angular frequency, and ϕ_n is the phase, mode-locking occurs when the phases ϕ_n are synchronized such that $\phi_n = n\phi$ for a constant ϕ, see Figure 5.1. This phase synchronization causes the modes to interfere constructively at regular intervals, producing a train of pulses [62]. The resultant electric field can be expressed as $E(t) = \sum_n E_n \cos(\omega_n t + n\phi)$. The superposition of these modes result in periodic pulses with a separation of the length of the cavity and a duration inversely proportional to the bandwidth of the modes [61].

Optical Parametric Oscillator

An Optical Parametric Oscillator (OPO) is a device that converts a pump laser frequency into two different frequencies, termed the signal and idler frequencies, through the process of parametric down-conversion in a nonlinear crystal [61, 62]. The fundamental mechanism is governed by the energy conservation and phase-matching conditions. The relationship can be expressed as $\omega_p = \omega_s + \omega_i$ for the frequencies, where ω_p is the pump frequency, ω_s is the signal frequency, and ω_i is the idler frequency. Additionally, for efficient energy transfer, the phase-matching condition must be satisfied: $k_p = k_s + k_i$, where k represents the wave vectors of the respective waves [32]. By adjusting the phase-matching conditions

and the nonlinear medium properties, an OPO can be tuned to generate a broad range of frequencies.

Custom Ekspla Ultraflux Laser System

The Ekspla UltraFlux laser system is a tunable femtosecond system utilizing Optical Parametric Chirped Pulse Amplification (OPCPA) to generate pulses in the tens of femtoseconds with peak powers in the Terawatt range. Our custom-built system has a tunable range from 750 to 960 nm with pulse energies up to 50 mJ and pulse durations down to 25 fs which operates at 5 Hz, see Figure 5.3. Additionally, it features a separate 355 nm output with 60 mJ pulse energy and 90 ps duration, as well as two 532 nm outputs with pulse energies of 30 mJ and 40 mJ, and durations of 30 ps and 90 ps, respectively. The system also includes an Optical Parametric Oscillator (OPO) pumped by the 355 nm source, capable of generating pulses from 210 to 2300 nm with pulse energies up to 10 mJ. All laser outputs originate from the same source, resulting in a jitter of less than five picoseconds between individual beams. This low jitter simplifies synchronization between the laser outputs and detectors, making the system exceptionally suitable for short pulse diagnostics.

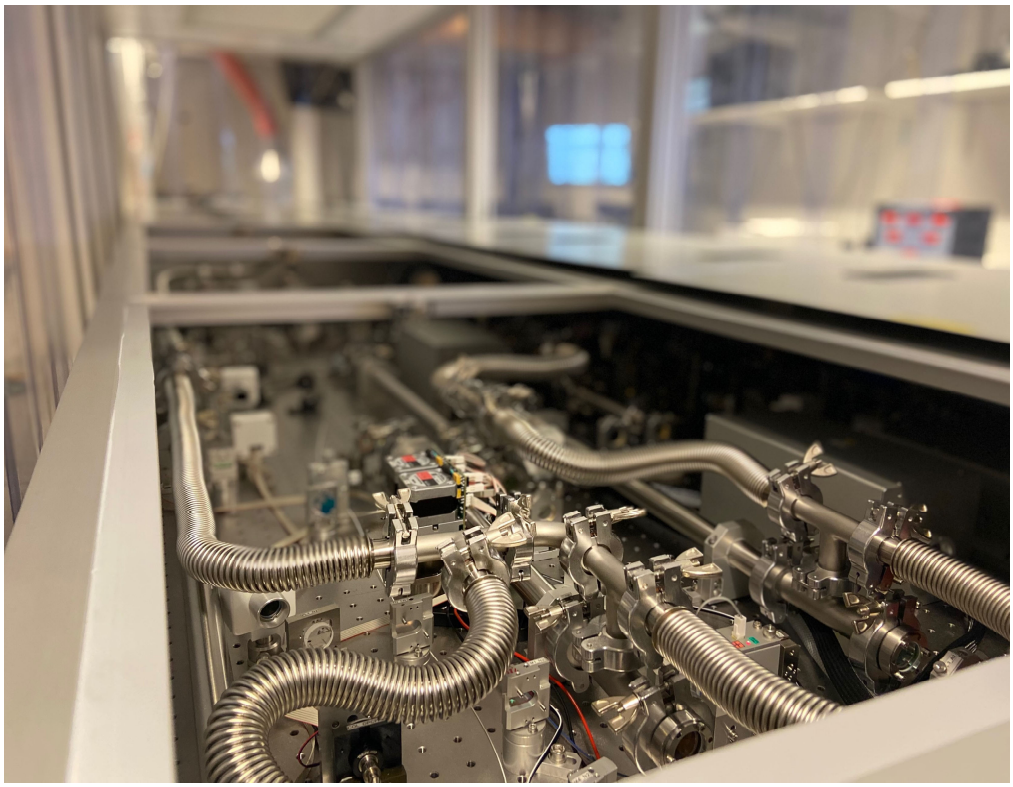

Figure 5.2: A photograph of the custom Ekspla UltraFlux newly installed at the division of Combustion Physics.

Ekspla SL334

The Ekspla SL334 is a solid-state, Q-switched Nd:YAG laser with a fundamental wavelength of 1064 nm. It produces picosecond pulses with a pulse duration of 190 ps and can generate harmonics at 266 nm, 355 nm, and 532 nm. The pulse energy can reach up to 500 mJ, depending on the harmonic used, and it operates at a repetition rate of 5 Hz.

Quantel Q-Smart 850 & Quantel Brilliant B

The Quantel Q-Smart 850 and Quantel Brilliant B are Q-Switched Nd:YAG lasers operating at a fundamental wavelength of 1064 nm. These lasers are capable of producing multiple harmonic wavelengths through the addition of harmonic generation modules. They feature pulse lengths of 5-6 nanoseconds, depending on the configuration, and can deliver pulse energies up to 850 mJ with a repetition rate of 10 Hz. The primary distinction between these two models is that the Q-Smart 850, being a more recent model, includes automatic phase matching.

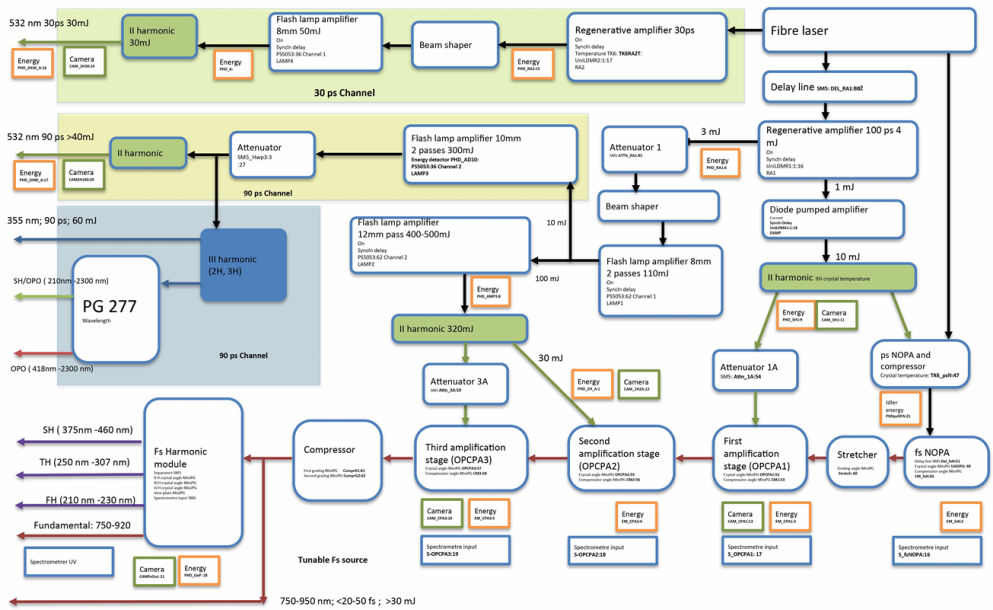

Figure 5.3: Graphical layout of the Custom Ekspla Ultraflux Laser System.

5.2 Photomultiplier Tubes and Intensified Cameras

When the laser interacts with matter in the probe volume, it generates a scattered or emitted signal. Because this signal is very weak, specialized detectors are required to capture and analyze it both spatially and temporally. This section will provide a brief introduction to key concepts of various detectors and their operation [63, 64].

Photomultiplier Tubes

A photomultiplier tube (PMT) operates by converting light into an electrical signal through the photoelectric effect, followed by a series of amplification stages via secondary emission from dynodes [63]. When light strikes the photocathode, it generates electrons through the photoelectric effect, and these photoelectrons are emitted into the vacuum of the tube. Focusing electrodes then accelerate and direct the photoelectrons towards the surface of the first dynode. Upon impact, the photoelectrons are multiplied through a process called secondary emission. This multiplication is repeated at each dynode in the chain, resulting in an overall multiplication factor of 10^6 to 10^7, a schematic of a photomultiplier seen in Figure 5.4. The secondary electrons emitted by the final dynode are collected by the anode, producing an output signal [65]. The spectral sensitivity range of a PMT is determined by the type of photocathode material employed. Photomultiplier tubes can be time-gated,

which enables the PMT to accept radiation only in a predetermined time window that is determined by an input gating pulse, which allows one to temporally filter signals to reduce background signals [64].

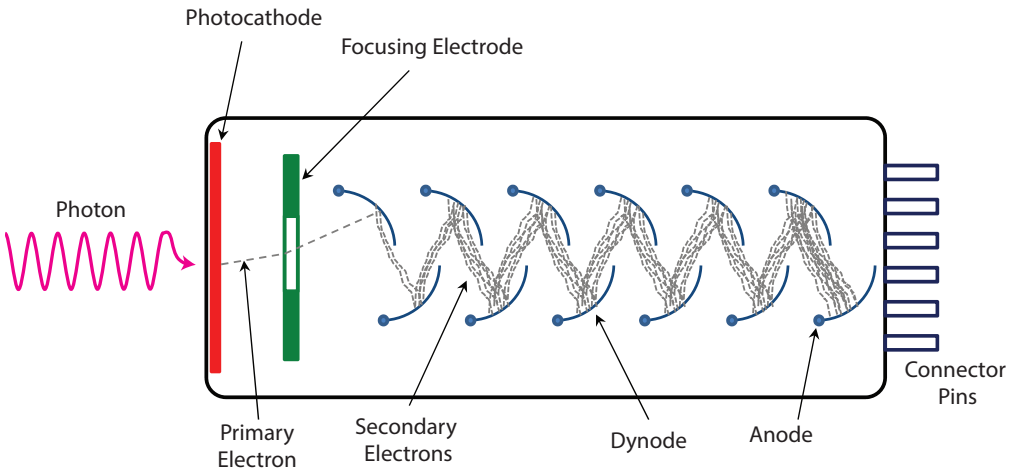

Figure 5.4: Schematic of a photomultiplier tube with signal output via connector pins. Adapted from [66].

Microchannel Plate Photomultiplier Tube

A microchannel plate photomultiplier tube (MCP-PMT) is a photomultiplier that uses tiny microchannels, each functioning as an individual photomultiplier, to achieve spatial resolution. The photocathode converts photons into photoelectrons. These electrons then enter the microchannels of the MCP, where they collide multiple times with the channel walls, causing secondary electron emissions and creating a cascade effect that significantly amplifies the signal. The amplified electrons are collected at the anode, producing an electrical signal proportional to the incident light. MCP-PMTs offer extremely fast temporal response times, faster than conventional PMTs with dynodes because of shorter path for electrons due to the microchannel, significantly reducing transit time.[65].

Intensified Cameras

Laser-induced signals are typically much weaker than the surrounding background when observed on the timescale of standard camera exposure times. Standard cameras have exposure times ranging from a few hundred microseconds and longer, during which the integrated background signal often overwhelms the laser-induced signals, making detection challenging. However, these laser-induced signals have high peak power, enabling detection through temporal filtering of background emissions. To address the limitations of

traditional cameras, intensified cameras, such as ICCD (Intensified CCD) and IsCMOS (Intensified sCMOS), have been developed. These cameras combine a MCP with a detector chip (either a CCD or an sCMOS), allowing temporal gating down to a few nanoseconds. This high temporal resolution makes intensified cameras ideal for time-resolved spectroscopy, where capturing transient phenomena and observing rapid processes is crucial. They also effectively reduce strong background signals through temporal filtering [64]. By recording data at various time points after an excitation event, intensified cameras enable the study of dynamic events with both spatial and temporal precision [63].

6 Phosphor Thermometry

Phosphor thermometry is a technique used to measure temperature by exploiting the temperature-dependent properties of phosphor materials. These luminescent materials emit light when excited by an external energy source, typically UV or visible light. The emitted light's characteristics such as intensity, decay time, and spectral features vary with temperature [9]. This section will explain the luminescence mechanism of thermographic phosphors and how these properties can be used to deduce temperature.

6.1 Thermographic Phosphors

Thermographic phosphors are usually inorganic materials that are mainly composed of a host and an activator [9]. The host, usually a ceramic, is optically inactive when irradiated by electromagnetic radiation or other sources such as electrons. Doping the host with an activator leads to luminescence being emitted by the composite material. The activator makes the host optically active and usually emits photons upon excitation in the visible part of the spectrum, which depends on the activator ion. The phosphor is traditionally sprayed onto a surface in a thin layer (10-20 μm) such that the phosphor has minimal interference on the measurement object. Depending on the application, different host and dopants are used to satisfy the experimental needs [67].

Host Crystal and Dopant Selection

The choice of dopants is crucial for determining the response of thermographic phosphors. Different dopants introduce unique energy levels within the host material's band structure, resulting in varying emission properties [68]. The type and concentration of the dopant affect the intensity of the emitted light upon excitation. Typically, increasing the dopant concentration enhances phosphorescence up to an optimal point, usually a few weight percent of the host crystal ions. For example, YAG:Dy (2%) means that two percent by weight of the yttrium ions have been replaced by Dy^{3+} ions. Beyond this level, concentration quenching can occur, reducing the intensity. This phenomenon arises primarily due to non-radiative energy transfer processes that occur between adjacent dopant ions when they are in close proximity. Another method to enhance luminescence properties is codoping. Codoping involves adding another activator to either: (i) aid in energy transfer from the excitation light to the main activator ion, or (ii) improve the local symmetry around the activator ion to enhance energy transfer [69]. The amount of codoping is typically less than that of the activator. For example, in YAG:Dy(2%)Ce(1%), here Ce^{3+} is the codopant with a lower concentration than Dy^{3+}.

The decay time of the phosphorescence post-excitation also varies with dopant type and can be adjusted to meet specific temporal resolution requirements. Dopant selection, typically transition metals or lanthanides, influences quenching and saturation effects, with non-radiative recombination processes becoming significant at higher temperatures, thereby reducing phosphorescence efficiency. The interaction between the host material and the local environment of the dopant impacts the overall efficiency and stability of the phosphor. A compatible host-dopant combination ensures efficient energy transfer and stable luminescent properties, which are essential for consistent and reproducible temperature measurements.

Dopants

Transition metal atoms feature an incompletely filled d subshell in their second outermost shell, while their outermost shell contains two s electrons. Upon ionization, these atoms typically lose the s electrons, leaving the d electrons exposed to the surrounding crystal environment. This exposure results in the luminescence of transition metal-doped phosphors being more strongly influenced by the crystal field effects of the host material compared to those doped with lanthanides [9]. Such phosphors usually have a spectrally broad emission, and the onset of temperature sensitivity occurs at lower temperatures due to poor shielding, rendering such doped phosphors better suited for low-temperature (less than 1000 K) applications.

Lanthanides are typically used for high-temperature applications (generally above 1000 K) due to the shielding of the $4f$ orbital [67]. Emission spectra from lanthanide elements are characterized by sharp spectral lines because the $4f$-shell of lanthanide elements are shielded by the filled $5s$ and $5p$ shells. This shielding means the host crystal has little effect on the position of these levels, so the emission from incorporated lanthanide ions in solids resembles that of free ions. In lanthanides, luminescence arises from $4f$ - $4f$ transitions, $4f$ - $4f5d$ transitions, and charge transfer transitions [68]. Due to these characteristics, the onset of temperature sensitivity in thermographic phosphors doped with lanthanides typically occurs above 1000 K and is sensitive up to high temperatures. For instance, YAG:Dy (2%) has demonstrated temperature sensitivity up to 2000 K.

6.2 Measurement Techniques

There are two main approaches for determining the temperature of thermographic phosphors: analyzing the spectral changes as the temperature varies or examining the temporal behavior of the phosphorescence intensity [9, 70, 71].

Spectral

The emission spectra of phosphors can change with temperature. Notable temperature-induced changes in the emission spectra include:

- **Thermalization**: As the temperature increases, higher vibrational levels in the phosphors are populated according to the Boltzmann distribution [67], allowing for more transitions to occur. Consequently, a higher population in these energy levels can increase or decrease the emission intensity of an emission line with rising temperature. Additionally, this may also cause additional emission lines to reveal themselves at higher temperatures.
- **Shift**: Thermal expansion of the crystal structure can influence the separation of the energy levels, resulting in a wavelength shift of the emission lines [72].
- **Lattice Vibrations**: Temperature increase causes lattice vibrations, creating a changing crystal field that produces a broadening of emission linewidths.

Additional broadening effects discussed in Section 3 may also impact the spectral behavior of phosphors.

The spectral changes of a phosphor can be leveraged to deduce a temperature. Most commonly, this is done by a method called Spectral Intensity Ratio (SIR), where the ratio of two emission lines is used to determine temperature [73]. This is achieved by using two optical filters to isolate light from two different spectral regions corresponding to two emission lines in a phosphor. As the temperature changes, the ratio between these two emission bands changes due to the mentioned effects, and this ratio can be correlated to the temperature. This is usually done with two detectors, which can either be point detectors or a 2D detector that captures the two emission bands during the same excitation pulse. The ratio from these two detectors is then correlated toward a calibration curve to extract the temperature [74]. Although the method is theoretically simple and robust, suitable for 2D measurements, it is highly sensitive to ambient light and optical path variations. It is typically restricted to lower temperatures since higher temperatures introduce significant background emission, affecting the ratio and thus the measured temperature. Additionally, the method's sensitivity, or the rate of change in the ratio with temperature, is generally low, leading to lower accuracy and precision compared to measuring decay time [75].

Temporal

The so called decay time method uses the temporal dynamics of the phosphorescence signal to determine temperature. Thermographic phosphors' decay times typically change by 2-3

orders of magnitude over a few hundred degrees of temperature change [76]. In contrast, the SIR usually changes by only one order of magnitude for the same temperature range, leading to improved sensitivity, precision, and accuracy for the temporal method.

The factors affecting the decay time of phosphorescence from a phosphor are detailed in Section 2.3. Practically, the temporal response of a phosphor after excitation is typically recorded using a PMT, with the PMT signal read by an oscilloscope [77]. The decay curve is stored and later analyzed to determine the decay time, usually employing a single exponential fit to find the characteristic lifetime rather than multi-exponential fitting to find the individual decay paths of various energy levels in the phosphor. The most robust method uses an adaptive window algorithm that adjusts the fitting window on the decay curve to where it is most mono-exponential or most stable using the following equation:

$$I = I_0 \exp\left(-\frac{t}{\tau}\right) + I_{Offset}. \tag{6.1}$$

The adaptive fitting window algorithm adjusts the fitting window and recalculates the decay time until a stable solution is achieved [78, 79]. The starting point of the fitting window, measured from the peak of the decay curve, is defined by $t_1 = c_1 \cdot \tau$, while the endpoint of the fitting window is given by $t_2 = c_2 \cdot \tau$. In the first iteration, τ represents the decay time estimate either by guess or some rough estimate, see Figure 6.1. In subsequent iterations, τ is updated to the decay time measured from the previous iteration until the difference between the previous $\hat{\tau}$ and the current τ is sufficiently small.

The determined decay time,τ, is then compared to a calibration curve to extract the temperature. The decay time method can be extended to 2D measurements using high-speed intensified cameras or ICCD/IsCMOS cameras [80]. The camera captures different parts of the decay curve and forms a ratio between these images. This ratio changes with the decay time, allowing temperature determination. A more detailed description of such algorithms is presented in Section 8.

Unlike the SIR method, the decay time method is insensitive to variations in detector positioning [81]. With the use of high-gain detectors, the decay time method can measure higher temperatures than the intensity ratio method.

There are several experimental considerations associated with both PMT and camera measurements of phosphorescence decay time. A detailed discussion of these considerations can be found in Dr. Henrik Feuk's thesis, to which I direct the reader [82].

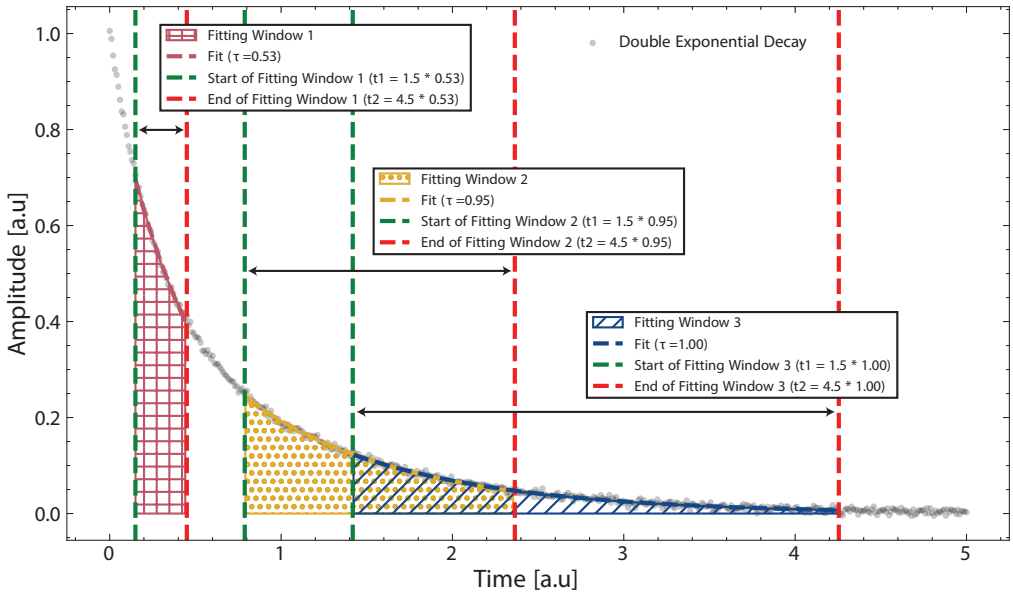

Figure 6.1: Simulated decay curve showing the iterative procedure of decay time fits. The simulated decay curve consists of two exponential decay, one with a lifetime of $\tau = 0.25$ and one with $\tau = 1$ both have equal contribution. The algorithm iterates until a stable solution is found.

7 Coded Imaging

In applications where background interference or scattering significantly affects contrast and image quality, encoding the signal of interest can mitigate these issues. In the context of this thesis coded imaging using structured illumination is used to enhance image contrast, primarily harsh imaging environments, such as in plasma studies and highly scattering environments. While non-laser-induced background signals can often be estimated and subtracted, contributions from spurious scattered light cannot be handled the same way and require different approaches.

Spurious scattered light poses significant challenges for quantitative imaging, both when (i) the laser interacts with the measurement object and (ii) the laser-induced signal propagates toward the detector. To suppress this multiply scattered light, methods based on structured illumination have been developed. The principle behind these approaches is that photons undergoing multiple scattering events will lose the superimposed structured information, unlike singly scattered light [83, 84]. The contribution from singly scattered light can be extracted using a spatial frequency lock-in filtering algorithm.

7.1 Practical application for coded imaging

Structured illumination can be achieved by periodically modulating the laser sheet in the probe volume with a cosine wave. Illuminating the sample with this modulated laser sheet produces an image, I, which is the product of the modulated laser intensity distribution and the spatial distribution of the object of interest, as described by:

$$I = I_C + I_S \cdot \cos\left(2\pi\nu_y \cdot y + \phi\right) \tag{7.1}$$

where ν_y is the spatial modulation frequency in the y-direction, and ϕ is an arbitrary spatial phase. This description involves two images: I_C and I_S. I_C is the conventional image, representing what one would obtain without modulating the laser sheet, while I_S contains the amplitude of the modulation, correlating to the intensity from the laser-induced signal [83, 85].

The information in I_S can be extracted through frequency-sensitive lock-in analysis, which separates the modulated signal from the non-modulated background. This analysis leverages the fact that the modulated information is frequency-shifted to higher spatial frequencies in the Fourier domain. The high-frequency components can be extracted by: (i) filtering out all other information in the Fourier domain with a frequency filter, (ii) translating the filtered data to the origin of the Fourier domain, and (iii) applying an inverse Fourier transform to the signal, resulting in a non-modulated image that contains the interference-free laser-induced signal, see illustration in Figure 7.1. The spatial resolution of such an image is typically reduced and is governed by two main factors: (i) the frequency of the imposed modulation, and (ii) the size of the frequency filter in the Fourier domain. The final image resolution results from the convolution of these two factors, so this method should be applied cautiously to objects with delicate image structures.

It should be noted that various factors such as dynamic range, spatial resolution, and modulation frequency need to be considered. A detailed discussion on these topics would be extensive, so I would direct the reader to the thesis by Dr. Vassiliy Kornienko for a comprehensive discussion and analysis [86].

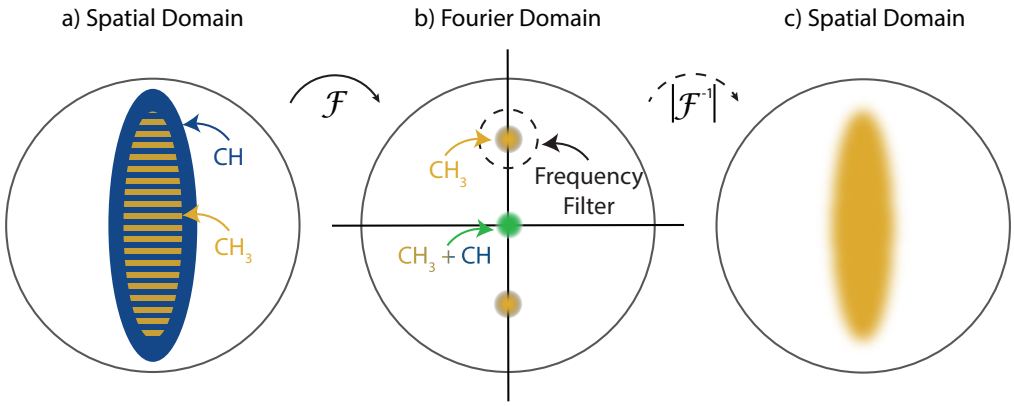

Figure 7.1: Example use of structured illumination to separate two species in a Photofragmentation Fluorescence imaging application from paper XII. Panel (a) shows the signal detected by the camera, comprising naturally occurring CH (blue region) and PF CH_3 (striped yellow region). Panel (b) presents the Fourier transform of (a), where the CH_3 signal is shifted vertically in the Fourier domain, while the non-modulated signal remains centered. A frequency filter is applied to the shifted signal, which is then moved to the center of the Fourier domain and inversely transformed back to the spatial domain, resulting in the image in panel (c). This final image is free from background noise, stray light, and naturally occurring signals.

8 Fluorescence Lifetime Imaging

Fluorescence Lifetime Imaging encompasses all measurement techniques capable of producing a two-dimensional image of fluorescence lifetime. Originally developed to investigate local variations in fluorescence quantum yield, this technique, within the context of this thesis, is employed to gain insights into the local environment of fluorescent molecules. The fluorescence lifetime is sensitive to neighboring species due to their influence on the non-radiative quenching rate, thus affecting the fluorescence lifetime. Fluorescence imaging enables quantitative analysis of fluorescence signals, facilitating precise measurements of molecule concentrations, interactions, and activities [87]. This quantitative capability is crucial for comparing experimental conditions and drawing meaningful conclusions [88, 40].

8.1 Measurement Techniques

Several techniques have been developed to perform FLI in both the temporal and frequency domains. However, this thesis focuses on determining the fluorescence lifetime in the temporal domain and hence the discussion here is limited to temporal techniques. The temporal response of the fluorescing signal is usually approximated by a single exponential decay as the detector usually has a spectral filter such that only one emission line is analyzed, as the quenching rate between different emission lines may vary and hence the fluorescence lifetime [89].

Time Correlated Single Photon Counting

Time-correlated single photon counting (TCSPC) is a highly sensitive technique for measuring the time intervals between photon emission and a reference signal. The process starts by exciting a sample with a pulsed light source, usually a laser emitting extremely short pulses in the picosecond or femtosecond range. When the sample absorbs this laser light, it re-emits photons via fluorescence. These emitted photons are detected by a point detector, such as a PMT or an avalanche photodiode (APD). A timing signal synchronized with the laser pulse acts as the start reference for the timing measurements. Each detected photon generates a stop signal, and the time interval between the reference signal (start) and photon detection (stop) is measured [88]. These time intervals are recorded to build a histogram, showing the distribution of photon arrival times relative to the excitation pulse. This histogram represents the temporal profile of the sample's fluorescence signal. TCSPC's key advantage is its ability to evaluate multiple fluorescence lifetimes within a signal. The technique offers temporal resolutions as low as tens of picoseconds. However, it requires a high-repetition-rate laser system since only one photon is detected per excitation pulse. Additionally, being a point measurement technique, TCSPC requires a scanning procedure to obtain a fluorescence lifetime image. Consequently, it is limited to objects that are both temporally and spatially stationary [40].

Temporal Gating Techniques

Instead of temporally sampling the signal with high resolution to determine the fluorescence lifetime, gating techniques sample two or more parts of the fluorescence decay. By forming a ratio between these samples, the fluorescence lifetime can be deduced [90].

The most popular one is called Rapid Lifetime Determination (RLD) and is illustrated in Figure 8.1 [90]. From these two intensity windows I_1 and I_2, and by knowing the width of the intensity windows Δt the fluorescence lifetime can be calculated as:

$$\tau = -\frac{\Delta t}{\ln\left(\frac{I_2}{I_1}\right)}. \tag{8.1}$$

This algorithm can be easily implemented using a picosecond laser and a compact formula, either for point measurements or imaging [90]. When using intensified cameras, the gate function is assumed to be a square integration box. The two PLIF images form a ratio image, with each pixel value serving as input data for Equation (8.1), producing a fluorescence lifetime image. However, the sensitivity of RLD is limited; as the fluorescence lifetime shortens, the total intensity in I_2 decreases, reducing the SNR and accuracy of the

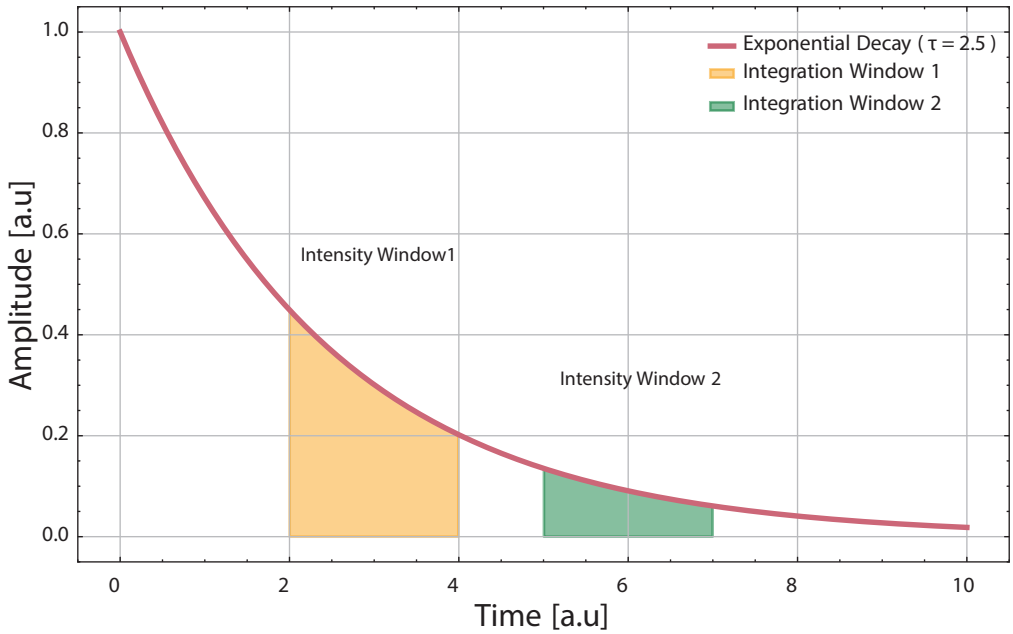

Figure 8.1: Illustration of RLD.

algorithm. To address this, an optimized algorithm called Optimized Rapid Lifetime Determination (ORLD) has been developed, which uses variable-width integration windows [91]. This approach significantly improves the SNR, as the intensity in I_2 is higher, and enhances the dynamic range of the algorithm by minimizing errors in the determined lifetime through optimal window selection. The intensity in each window then becomes:

$$I_1 = \int_0^{\Delta t} I_0 \exp\left(-\frac{t}{\tau}\right) dt \tag{8.2}$$

and

$$I_2 = \int_{Y\Delta t}^{Y\Delta t + P\Delta t} I_0 \exp\left(-\frac{t}{\tau}\right) dt. \tag{8.3}$$

The variables Y and P are adjustable coefficients for the integration intervals. The ratio of the one integration to the other is formed, yielding the following expression:

$$\frac{I_2}{I_1} = \frac{\exp\left(-R\left(P+Y\right)\right) - \exp\left(-RY\right)\right)}{\exp\left(-R\right)\right) - 1} \tag{8.4}$$

where

$$R = \frac{\Delta t}{\tau}. \tag{8.5}$$

In contrast to RLD, ORLD does not have a closed-form solution and requires an iterative Newton-Raphson method for solving. However, because the detector gate shape and efficiency change with short gate widths (less than 100 ns), both RLD and ORLD algorithms is not suitable for fluorescence imaging and has therefore seen limited use.

To address this issue, Ehn et al. developed an algorithm called Dual Imaging with Modeling Evaluation (DIME), which considers the gate shapes of the two integration windows through gate mapping [24, 92]. The gate windows are created by stepping the camera gate over the laser pulse, effectively performing a convolution of the laser pulse and the gate. Since the laser pulse duration is much smaller than the camera gate, the signal obtained on the camera corresponds to the gate shape itself[1]:

$$G(t) = l(t - \delta) * g(t - \delta) \tag{8.6}$$

where $l(t)$ represents the laser pulse and $g(t)$ represents the camera gate shape and δ is the time jitter between the laser and the gate function. The mapped camera gate $G(t)$ can then be utilized in the evaluation scheme to compensate for variations in detector efficiency. In DIME, two integration windows are employed: one that captures the full fluorescence decay and another that captures the early part of the decay. The intensity in each integration window then becomes:

$$I_j = \int G_j(t - \Delta t_j - \delta) S(t) dt. \tag{8.7}$$

where j denotes the gate number and Δt_j is the individual gate delay. In practical terms, these are usually referred to as long and short gates. A ratio is formed between these images, allowing the ratio D to be calculated:

$$D(x, y) = \frac{I_{Short}(x, y)}{I_{Short}(x, y) + I_{Long}(x, y)}. \tag{8.8}$$

Using the mapped gates, a model that relates the ratio D to the lifetime τ can be established. An example of this model is shown in Figure 8.2.

[1] Similar to convolving a function $F(t)$ with a Dirac delta function $\delta(t)$, which results in the function itself $F(t)$.

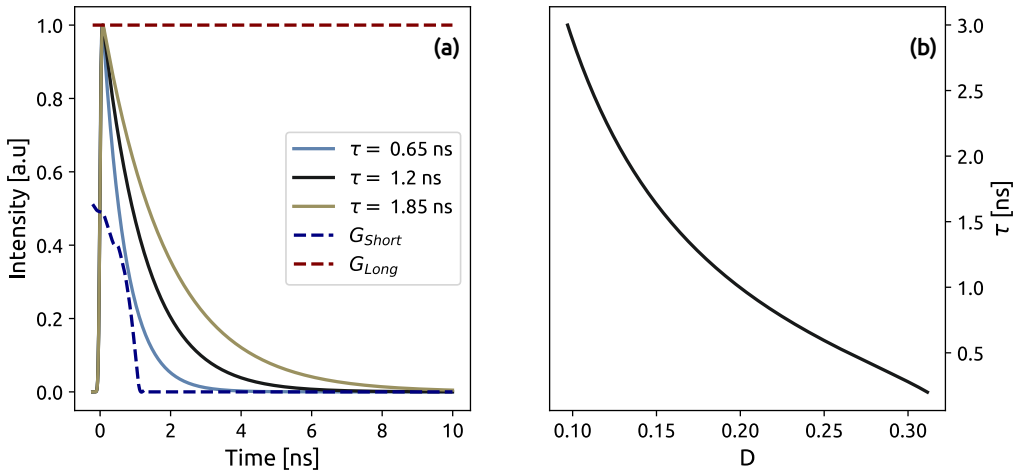

Figure 8.2: Example of DIME gate setup as used in Paper IV.

A single camera can be used to acquire both images if the variations in the excitation and the measurement object are insignificant during the acquisition process. When using two cameras, the images need to be matched pixel-by-pixel. If the measurement system is carefully characterized, all parameters in Equation (8.6) are known except for the signal, $S(t)$. While it is not possible to determine the full temporal shape of the signal using Equation (8.6), a single parameter characterizing the signal can be determined under certain conditions, provided there is an unambiguous relationship between this parameter and the ratio.

To use Equation (8.6) (8.7) (8.8) in its complete form, the following system characteristics need to be determined:

- The temporal shapes of the gate functions
- The delay time of the camera relative to the time of excitation
- The duration of the laser pulse
- The time jitter between the laser pulse and the trigger pulse
- The expected temporal shapes of the signals from the measurement volume

Minimizing the time jitter between the cameras and the laser pulse to be smaller than the laser pulse width greatly simplifies the experiment and subsequent data evaluation. In this thesis, the DIME algorithm has been used to determine lifetimes in Paper IV and Paper XIII.

9 Rayleigh Thermometry

Laser-based Rayleigh thermometry is a non-intrusive diagnostic technique used to measure temperature in various media, particularly gases. This method relies on the principles of Rayleigh scattering, where light is scattered by particles much smaller than the wavelength of the incident light. The scattered light intensity is influenced by the temperature of the scattering medium, allowing for temperature measurements [93]. The physical process of Rayleigh scattering is outlined in section 2.2.

The scattered light intensity decreases as the temperature of the gas increases according to the ideal gas law [94]:

$$P = nRT. \tag{9.1}$$

The intensity of Rayleigh scattered light I_{Rs} is directly proportional to the number density n of the gas molecules, which is inversely proportional to the temperature T at constant pressure [95, 36]:

$$I_{Rs} \propto n \propto \frac{1}{T}. \tag{9.2}$$

Different gases have varying polarizabilities, resulting in differences in their scattering cross-sections. Larger or more complex molecules generally exhibit higher polarizabilities and thus larger Rayleigh scattering cross-sections compared to smaller or simpler molecules [93]. If the gas composition remains constant, a reference measurement can be performed at a known temperature. By comparing the signal from this reference to the measurement data, assuming other parameters such as detector gain and laser power remain constant, the temperature can be deduced using the following formula [96]:

$$T_{\text{Measured}} = \left(\frac{I_{\text{Reference}}}{I_{\text{Measured}}} \right) T_{\text{Reference}} \tag{9.3}$$

The measured temperature, T_{Measured}, is sensitive to background signals. Therefore, it is crucial that both the reference and measurement data are free from background signals not originating from Rayleigh scattering, as these can bias the determined temperature [97]. If the gas composition varies in the probe volume, this variation must be accounted for in the evaluation. Consequently, a correction term should be added to Equation (9.3) to compensate for changes in the Rayleigh cross-section [98].

10 3D Emission Tomography

Three-dimensional emission tomography (3D ET) is an advanced imaging technique that reconstructs the three-dimensional spatial distribution of a source based on its emissions. Unlike traditional imaging, which captures only two-dimensional projections, 3D ET provides volumetric data, allowing for detailed analysis of the source's internal structure and properties. The fundamental principle of 3D ET involves capturing multiple two-dimensional images (projections) from different angles around the object. These projections are then computationally processed to reconstruct a three-dimensional representation of the emission source. In this thesis, a custom algorithm developed by Sanned et al. was utilized, which allows for random positioning of the cameras, offering enhanced experimental flexibility. [99].

10.1 Mathematical Formalism

To allow for practical computations the continuous probed volume Ω is initially discretized into N_v voxels. Thereafter, 2D line-of-sight projections q of Ω are acquired by cameras from various viewpoints, each view having individual pixel projections p in the form of a matrix ($m \times n$). Each pixel projection measurement p corresponds to an integral trough the probed volume. The continuous luminescence field $f(\vec{s})$ within the probed volume Ω represents intensity at spatial positions $\vec{s} = (x, y, z)$. The method revolves around mapping the objects luminosity onto each view projection qp using a first-kind Fredholm integral equation derived from the radiative transfer equation [100]:

$$b_{qp} = \int_{qp} f(\vec{s}) dA. \tag{10.1}$$

In this equation, b_{qp} denotes a camera projection measurement from pixel p in view q, and $f(\vec{s})$ represents the objects luminescence field. The model is a simplification of the radiative transfer equation as it neglects self-absorption and scattering effects. Discretizing the objects luminescence field into voxels, allows each measured projection shown in Equation (10.1) to be approximated as a finite sum

$$b_{qp} = \sum_{v=1}^{N_v} w_{qpv} x_v \tag{10.2}$$

where, x_v represents a voxel within Ω, and w_{qpv} denotes the contribution of that voxel to the complete projection qp. Smoothness was imposed on the solution, employing a sparse

discrete Laplacian matrix with homogeneous Dirichlet boundary conditions for all boundaries. Implementing the Laplacian matrix promotes continuous solutions, aligning with the expected physical behavior of the measurement object. Furthermore, the strategy mitigates any negative consequences arising from the potential ill-posed nature of the problem. The reconstruction problem can therefore be stated as a quadratic problem

$$\min_{x} ||b - A\mathbf{x}||_2^2 + \lambda \mathbf{x}^T \mathcal{L} \mathbf{x}. \tag{10.3}$$

In this equation, $\mathbf{x}$ is a vector representing the discretized field of $f(\vec{s})$, $\mathcal{L}$ is the Laplacian matrix, b is the measurement data vector, λ is a penalty term, and A is the projection matrix encompassing all linear voxel projections. This projection matrix A maps contributions from each 2D camera projections to each voxel in Ω based on Tsai's pinhole camera model [101]. Iterative methods are commonly employed to solve this type of problem and by doing so, reconstructing the full volume Ω. In this work the preconditioned conjugate gradient (PCG) method was used to solve the inverse problem, with convergence criteria defined by a relative residual tolerance of $||b - A\mathbf{x}||/||\mathbf{x}|| < 10^{-6}$.

Results

However beautiful the strategy,
you should occasionally look at the results.
–Winston Churchill

This chapter presents several key developments and findings from this thesis, focusing on the advancement of phosphors for high-temperature phosphor thermometry and the application of fluorescence lifetime imaging techniques. The work on novel phosphors includes their high-temperature calibration and an investigation into multi-exponentiality, particularly its dependence on oxygen quenching. In addition, the chapter explores the use of fluorescence lifetime imaging in high scattering environments and obtain quantitative data, such as relative number density and temperature, in a gliding-arc plasma. Furthermore, it details the development of a photofragmentation technique designed for interference-free measurements of methyl in a DBD plasma. The chapter draws on material from papers II, IV, V, VII, VIII, IX, XII, XIII, and some unpublished research.

11 Development of High-Temperature Phosphors

High-temperature measurements are challenging because phosphor luminescence signals must compete with strong blackbody background radiation [102]. According to Planck's law, the intensity of blackbody radiation increases with the fourth power of temperature, and the peak radiation wavelength shifts to shorter wavelengths as temperature rises. This is illustrated in Figure 11.1.

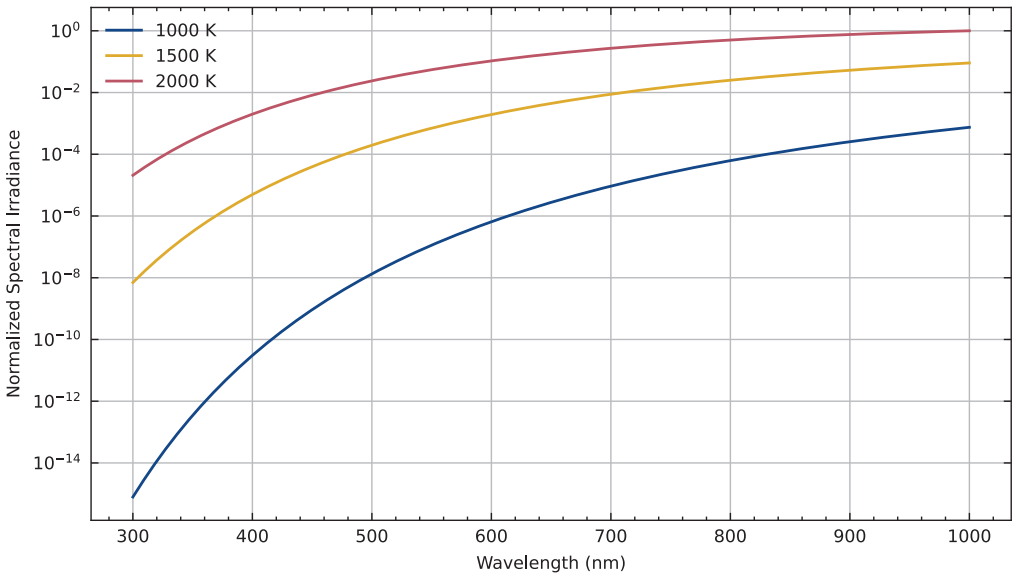

Figure 11.1: Normalized spectral irradiance of blackbody radiation across wavelengths from 300 nm to 1000 nm for temperatures of for some temperatures. The spectral irradiance is normalized to the maximum value from the highest temperature.

The increases background stemming from black body radiation affects the quality of the measurement and hence the determined temperature on several fronts:

- **Signal to Noise Ratio:** As the temperature rises, the spectral radiance from the measurement surface increases, which affects the quality of the signal detected by the detector, thereby reducing the measurement precision.
- **Detector Linearity:** A high background signal can adversely impact the detector's linearity, leading to measurement inaccuracies [103]. This issue is examined in detail in Paper I.
- **Sensor material:** As temperature increases, the stability of the phosphor material becomes crucial. It is important for the material to be resilient to high-temperature cycling effects and exhibit minimal hysteresis [104].

From Figure 11.1 it becomes clear that having a phosphor material that emits towards the blue region is greatly beneficial as the background emission is much lower, which benefits both the SNR and detector linearity. Moreover, it is beneficial if the phosphor has high peak intensity rather than strong luminescence, as it is easier to distinguish it from continuous background signals [105]. The choice of phosphor material also becomes crucial: it is essential that the host material can withstand high temperatures and that the dopant is compatible with the host and has emission in the blue region to improve SNR.

11.1 Investigation of High-Temperature Phosphors

For high-temperature thermographic phosphor applications, Yttrium Aluminum Garnet (YAG) is an attractive host material due to its high melting point of 2200 K . There are several doping variations of YAG, with YAG:Dy being the most popular because it has reasonable sensitivity and an emission line at 456 nm which makes it attractive for high temperature measurements [106]. The phosphorescence lifetime of YAG:Dy changes by three orders of magnitude from the onset of temperature sensitivity up to 2000 K [107]. Although YAG:Dy exhibits strong luminescence due to its relatively long lifetime (ranging from 10^{-3} to 10^{-6} seconds), it has a relatively low peak intensity. As a result, at higher temperatures, the precision of the determined lifetime and thus the temperature decreases due to a reduced SNR [104].

As part of this thesis work, we investigated potential alternatives to YAG:Dy to increase the SNR and hence the measurment precision. In total, 16 different phosphors were investigated, including YAG:Dy, see Table 1.

The selected phosphors needed to have an emission line in the blue region. YAG:Dy was included as a benchmark due to its widespread use in high-temperature thermometry [108]. Co-doping has been explored to enhance phosphor luminosity, increasing luminescence and altering decay time. YAG:Dy co-doped with Pr was selected because it has been shown to increase luminosity by 30% [109, 110]. Phosphors co-doped with Ytterbium were considered for their potential use in up-conversion excitation. Ce doping has been shown to boost luminosity and decrease decay time. Nd co-doped phosphors have exhibited increased UV absorption, enhancing luminescence [109]. YAG:Tm was chosen for its emission lines at 365 and 456 nm, which are suitable for thermometry [110]. Li co-doping is known to significantly enhance luminescence by increasing crystallite size and breaking dopant-ion pairing, as well as altering optical properties, so YAG:Tm was co-doped with Li^+ [106, 111, 112].

Exploring potential thermographic phosphors and their emission for lifetime phosphor thermometry can be a lengthy process, particularly when using conventional calibration methods. These methods typically require the operator to wait for the phosphor sample

Table 1: This table lists the properties of various phosphors studied for high-temperature applications. All phosphors were purchased from Phosphor Technology Ltd. The phosphors labeled "Not Tested" have not been tested prior to this work, to the best of the authors' knowledge.

Phosphor	Chemical Formula	Temperature [K]	Decay Time	Reference
YAG:Dy (2%)	$Y_{2.94}Al_5O_{12}:Dy_{0.06}$	1300-2000	0.75 ms – 0.5 µs	[113], [114], [105]
YAG:Dy(2%)Pr(1%)	$Y_{2.91}Al_5O_{12}:Dy_{0.06}Pr_{0.03}$	1300-1600	0.6 ms – 100 µs	[115]
YAG:Dy(2%)Yb(1%)	$Y_{2.91}Al_5O_{12}:Dy_{0.06}Yb_{0.03}$	Not Tested	Not Tested	Not Tested
YAG:Dy(2%)Yb(0.1%)	$Y_{2.937}Al_5O_{12}:Dy_{0.06}Yb_{0.003}$	Not Tested	Not Tested	Not Tested
YAG:Dy(2%)Ce(1%)	$Y_{2.91}Al_5O_{12}:Dy_{0.06}Ce_{0.03}$	Not Tested	Not Tested	Not Tested
YAG:Dy(2%)Ce(0.1%)	$Y_{2.937}Al_5O_{12}:Dy_{0.06}Ce_{0.003}$	Not Tested	Not Tested	Not Tested
YAG:Dy(2%)Nd(0.1%)	$Y_{2.937}Al_5O_{12}:Dy_{0.06}Nd_{0.003}$	Not Tested	Not Tested	Not Tested
YAG:Dy(2%)Nd(0.01%)	$Y_{2.9397}Al_5O_{12}:Dy_{0.06}Nd_{0.0003}$	Not Tested	Not Tested	Not Tested
YAG:Tm(1%)	$Y_{2.97}Al_5O_{12}:Tm_{0.03}$	1200-1700	0.2 µs - 100 ns	[116]
YAG:Tm(1%)Li(0.1%)	$Y_{2.967}Al_5O_{12}:Tm_{0.03}Li_{0.003}$	Not Tested	Not Tested	Not Tested
Y_2SiO_5:Dy(1%)	$Y_{1.98}SiO_5:Dy_{0.02}$	1200-1700	1 ms - 1 µs	[105]
$Y_2Si_2O_7$:Dy(1%)	$Y_{1.98}Si_2O_7:Dy_{0.02}$	1200-1700	1 ms - 10 µs	[105]
BSAS:Dy(1%)	$[Ba_{0.74}Sr_{0.25}]Al_2Si_2O_8:Dy_{0.01}$	1300-1700	0.75 ms – 0.1 µs	[105]
BSAS:Tb(1%)	$[Ba_{0.74}Sr_{0.25}]Al_2Si_2O_8:Tb_{0.01}$	1300-1700	3 ms - 1 µs	[105]

to reach thermal equilibrium in a furnace at each data point and then doing this several times depending on the spacing desired between each data point. As part of this thesis, a new automated calibration procedure was introduced, allowing for high-temperature lifetime calibrations up to 1900 K. This approach enables simultaneous calibration of multiple phosphors and the investigation of multiple emission lines for each phosphor [117, 103].

The experimental setup, shown in Figure 11.3, includes a galvo system that directs the excitation laser to specific spots on the alumina substrate to excite the targeted phosphor, as demonstrated in the zoomed-in view. A motorized filter wheel in front of the photomultiplier tube (PMT) allows investigation of different phosphor emission-characteristics. Ref-

erence temperatures for phosphor calibrations are measured using thermocouples inserted into indentations in the phosphor-coated substrate.

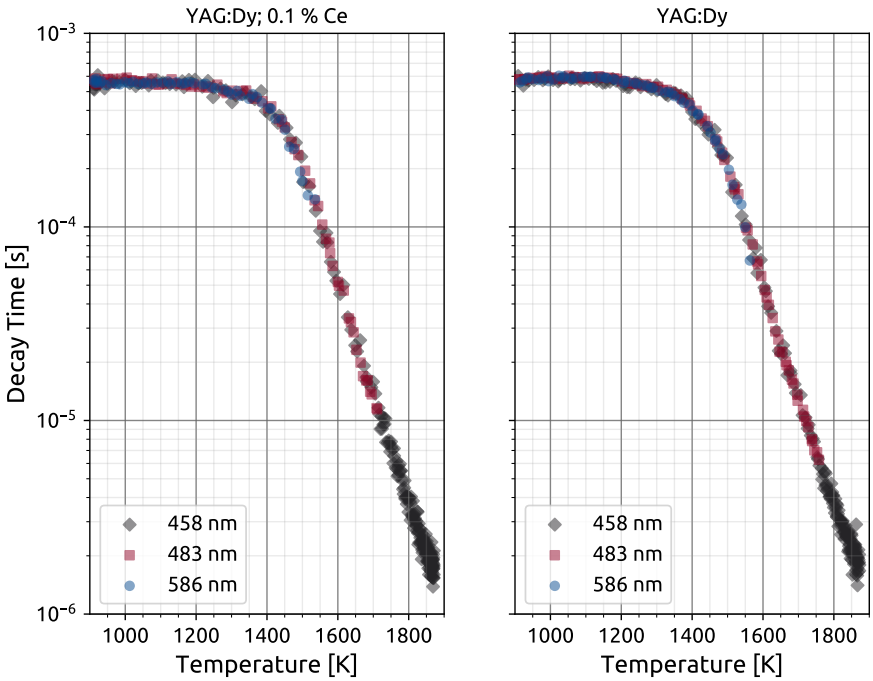

Figure 11.2: Calibration data captured by the automated calibration procedure, here showing both YAG:Dy and YAG:Dy;Ce. The wavelength in each figure corresponds to the filter center wavelnegth.

The main advantage of this method is that it ensures all phosphors and emission spectra are calibrated under the same environmental conditions, providing a powerful tool for comparing phosphor sensitivities to various environmental factors. A detailed description of calibration methodology can be found in paper II.

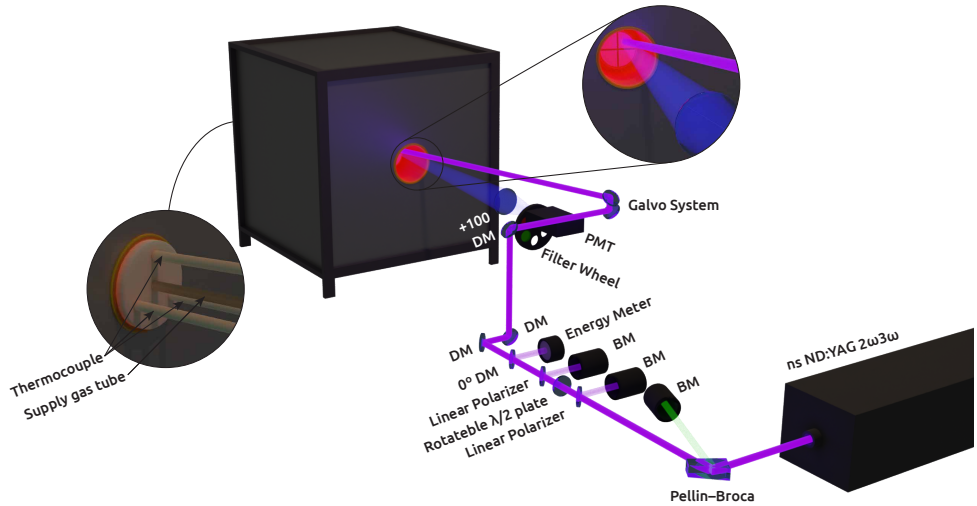

Figure 11.3: This experimental setup allows for the simultaneous calibration of multiple phosphors. DM stands for Dichroic Mirror. The zoomed-in section illustrates the configuration of the galvo system, which is currently set to excite the phosphor located in the upper right quadrant.

Table 2: An overview of the phosphor emission lines studied in this thesis with the corresponding bandpass filters.

Phosphor	Emission [nm]	Filter [nm]
YAG:Dy (2%)	456, 497, 573	458 ± 10 OD4, 483 ± 31 OD6, 586 ± 20 OD6
YAG:Dy(2%)Pr(1%)	456, 497, 573	458 ± 10 OD4, 483 ± 31 OD6, 586 ± 20 OD6
YAG:Dy(2%)Yb(1%)	456, 497, 573	458 ± 10 OD4, 483 ± 31 OD6, 586 ± 20 OD6
YAG:Dy(2%)Yb(0.1%)	456, 497, 573	458 ± 10 OD4, 483 ± 31 OD6, 586 ± 20 OD6
YAG:Dy(2%)Ce(1%)	456, 497, 573	458 ± 10 OD4, 483 ± 31 OD6, 586 ± 20 OD6
YAG:Dy(2%)Ce(0.1%)	456, 497, 573	458 ± 10 OD4, 483 ± 31 OD6, 586 ± 20 OD6
YAG:Dy(2%)Nd(0.1%)	456, 497, 573	458 ± 10 OD4, 483 ± 31 OD6, 586 ± 20 OD6
YAG:Dy(2%)Nd(0.01%)	456, 497, 573	458 ± 10 OD4, 483 ± 31 OD6, 586 ± 20 OD6
YAG:Tm(1%)	365, 456	365 ± 10 OD4, 458 ± 10 OD4
YAG:Tm(1%)Li(0.1%)	365, 456	365 ± 10 OD4, 458 ± 10 OD4
Y_2SiO_5:Dy(1%)	456, 497, 573	458 ± 10 OD4, 483 ± 31 OD6, 586 ± 20 OD6
$Y_2Si_2O_7$:Dy(1%)	456, 497, 573	458 ± 10 OD4, 483 ± 31 OD6, 586 ± 20 OD6
BSAS:Dy(1%)	456, 497, 573	458 ± 10 OD4, 483 ± 31 OD6, 586 ± 20 OD6
BSAS:Tb(1%)	542	543 ± 20 OD6

Emission spectra and lifetime calibrations were gathered for all phosphors, see Table 2 for detailed information about emission spectra, resulting in over sixty emission spectra and forty lifetime calibrations, see sample lifetime calibration in Figure 11.2. From this data, YAG:Tm;Li was chosen for more detailed investigation due to its superior signal-to-noise ratio (SNR) and unambiguous decay fitting compared to the other phosphors (see Table 3). YAG:Tm;Li exhibited approximately twice the signal of YAG:Tm. The non-YAG-based phosphors did not demonstrate the expected luminescence observed in previous studies.

Table 3: A summary of the phosphor survey. In the SNR column the values have the same convention as the emission lines column in Table 2. The bold SNR values indicate the 458 nm bandpass filter. The SNR is defined as the ratio of the average phosphorescence amplitude divided by the standard deviation of the background. The average phosphorescence amplitude is calculated by integrating the phosphorescence signal from the peak value to seven times the determined lifetime then dividing it by the determined lifetime. The comments are relative to YAG:Dy's properties.

Phosphor	**Lifetime Calibration Possible**	**SNR at 1200 K**	**Comments**
YAG:Dy (2%)	Yes	**110**, 530, 210	Was used as baseline
YAG:Dy(2%)Pr(1%)	Yes	**20**, 60, 50	Lower overall signal
YAG:Dy(2%)Yb(1%)	Yes	**50**, 250, 80	Lower overall signal
YAG:Dy(2%)Yb(0.1%)	Yes	**70**, 320, 110	Not significantly different
YAG:Dy(2%)Ce(1%)	Yes	**20**, 110, 30	Broad emission lines, bright at low temperatures
YAG:Dy(2%)Ce(0.1%)	Yes	**80**, 240, 120	Marginally broader emission lines, slightly brighter at low temperatures
YAG:Dy(2%)Nd(0.1%)	Yes	**80**, 310, 100	Not significantly different
YAG:Dy(2%)Nd(0.01%)	Yes	**30**, 150, 50	Lower overall signal
YAG:Tm(1%)	Yes	110, **340**	Higher peak signal level
YAG:Tm(1%)Li(0.1%)	Yes	160, **750**	Significantly higher peak signal level
Y_2SiO_5:Dy(1%)	No	—	Observed structural changes in coating at high temperatures
$Y_2Si_2O_7$:Dy(1%)	No	—	Observed structural changes in coating at high temperatures
BSAS:Dy(1%)	No	—	Coating integrity was compromised at high temperatures
BSAS:Tb(1%)	No	—	Coating integrity was compromised at high temperatures

This discrepancy may be attributed to interactions between the YAG binder and the host material. These hosts possess complex phase diagrams, and interactions between the host and binder could potentially affect the luminescence properties of the phosphors.

The Dieke diagram is a graphical tool used to represent the energy levels of lanthanides. This diagram, depicted in Figure 11.4, showcases the electronic energy levels and transitions of these ions in various host materials. In this Figure an overview of the energy levels properties of Dy^{3+} and Tm^{3+} can be observed. For Dy^{3+}, the Dieke diagram highlights transitions between multiplet levels such as $^6H_{15/2}$, $^4F_{9/2}$, and $^4I_{15/2}$. Significant transitions occur in the visible spectrum, including a yellow emission at 582 nm and a blue emission at 456

nm, which are marked in the diagram. In the case of Tm^{3+}, transitions from the $^3H_6$ ground state to higher energy levels like $^1D_2$ and $^3F_4$ to $^1D_2$ which both can be used for thermometry.

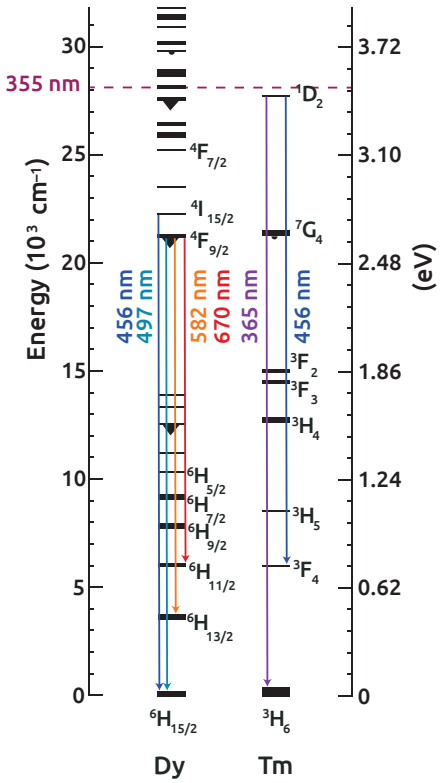

Figure 11.4: Dieke energy diagram for Dy^{3+} and Tm^{3+} displaying the observable emission lines studied in this paper. The horizontal dashed line marked indicates the excitation energy of the third harmonic of Nd:YAG.

Figure 11.5 presents the emission spectra for YAG:Dy and YAG:Tm;Li. YAG:Dy exhibits three prominent emission lines at 582 nm ($^4F_{9/2} \rightarrow {}^6H_{13/2}$), 497 nm ($^4F_{9/2} \rightarrow {}^6H_{15/2}$), and 456 nm ($^4I_{15/2} \rightarrow {}^6H_{15/2}$). The 456 nm line is typically used for high-temperature measurements as it becomes more prominent at elevated temperatures due to increased population density in higher energy levels. In contrast, YAG:Tm;Li displays two peaks: one at 456 nm ($^1D_2 \rightarrow {}^3F_4$) and another at 365 nm ($^1D_2 \rightarrow {}^3H_6$). The spectra for YAG:Tm;Li are shown only up to 1200 K because, at higher temperatures, the luminosity becomes too low for detection by the spectrometer. This is attributed to the decay time of YAG:Tm;Li being nearly two orders of magnitude shorter than that of YAG:Dy. The total luminosity of a mono-exponential decay is given by $I_{\mathrm{Tot}} = I_0 \cdot \tau$, indicating that the detected luminosity decreases by two orders of magnitude if I_0 is the same for both phosphors.

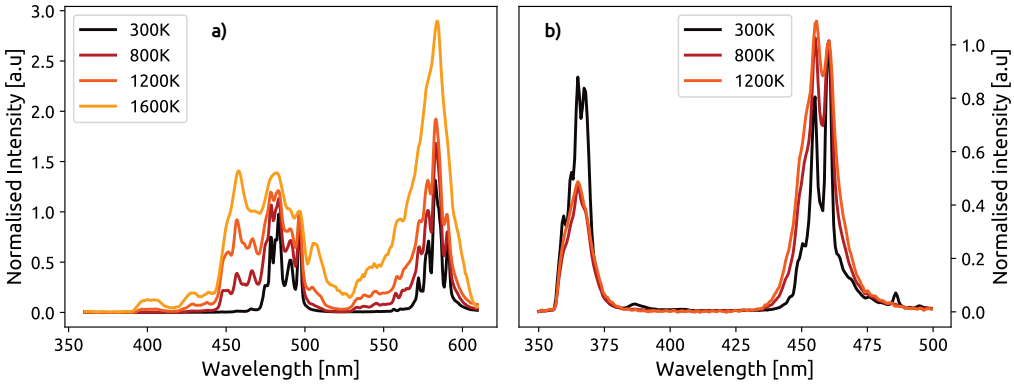

Figure 11.5: Emission spectra for YAG:Dy and YAG:Tm;Li are presented. In (a), the emission spectrum of YAG:Dy is shown up to 1600 K, normalized to the 497 nm peak. In (b), the emission spectrum of YAG:Tm;Li is displayed up to 1200 K, normalized to the 461 nm peak.

Figure 11.6(a) displays the peak phosphorescence signal of the lifetime component used for decay-time fitting (I_0 in Equation (6.1)). YAG:Tm is included for comparison with YAG:Tm;Li to evaluate signal strength. The introduction of Li^+ results in an average signal increase of 50% without significantly affecting the decay time. The peak phosphorescence signal for YAG:Tm;Li is consistently about ten times greater than that of YAG:Dy, enhancing the signal-to-noise ratio (SNR) and improving the accuracy of decay curve fitting.

Figure 11.6(b) plots decay time against temperature for both phosphors. The sensitivity onset occurs at approximately 1300 K for YAG:Tm;Li and 1450 K for YAG:Dy. Both phosphors exhibit similar sensitivity in the temperature-sensitive range, with average sensitivities of 1.26%/K for YAG:Tm;Li and 1.21%/K for YAG:Dy between 1400 and 1900 K. This data also explains why spectra at 1600 K for YAG:Tm;Li could not be obtained. Although YAG:Tm;Li has a peak signal value one order of magnitude larger than YAG:Dy, its decay time is about two orders of magnitude shorter, resulting in a total luminosity that is one order of magnitude lower.

Figures 11.6(c) and 11.6(d) compare decay curves at different temperatures, with the time axis expressed in terms of the determined lifetime to facilitate comparison of signal strength and SNR. As shown in Figure 11.6(c), the fluorescence component is approximately 75 times stronger than the phosphorescence component for YAG:Dy and about 10 times stronger for YAG:Tm;Li. At higher temperatures, the fluorescence component of YAG:Tm;Li quenches, and the phosphorescence component becomes more dominant, as seen in Figure 11.6(d). In contrast, YAG:Dy maintains a strong fluorescence component at all temperatures. The reduced peak signal strength in YAG:Dy decreases the precision of decay times, leading to greater variability in measured decay times compared to YAG:Tm;Li.

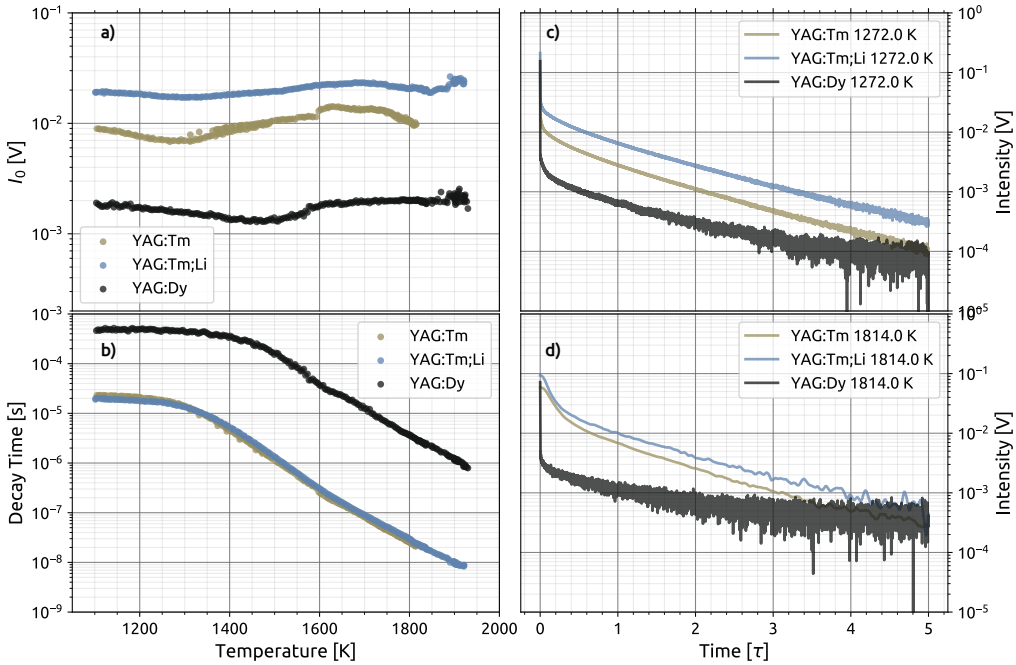

Figure 11.6: Comparison of YAG:Dy, YAG:Tm and and YAG:Tm;Li with both using a 458 ± 10 nm bandpass filter in air to 1930 K, YAG:Tm was only calibrated up to 1814 K. Figure a) shows the parameter I0 from equation (1) in b) decay time vs. temperature plotted using c1 = 0.5 and c2 = 4. In c) and d), two decay curves at different temperatures are compared with the x-axis, which is expressed as multiples of the measured decay time to facilitate the comparison of the signal strengths

11.2 Oxygen Sensitivity Study

In high-temperature applications such as gas turbines and internal combustion engines, the oxygen concentration may be lower than ambient levels due to the consumption of oxygen during combustion [12]. This reduced oxygen concentration can create oxygen vacancies in the phosphor's host lattice, shifting the charge-transfer state (CTS) and decreasing the nonradiative decay rate [118]. Consequently, the sensor becomes particularly sensitive to changes in oxygen concentration [68, 119, 108?].

The sensitivity of YAG:Dy and YAG:Tm;Li to oxygen concentration in the gas environment was investigated using a tube furnace. Decay time calibrations were conducted at oxygen concentrations of 21% and 0%, as shown in Figure 11.8, with a constant gas flow rate of 2 liters per minute in both scenarios. The phosphorescence peak signal, I_0, increased for both phosphors when exposed to pure nitrogen, consistent with previous studies. Additionally, the S-shaped pattern in the peak phosphorescence intensity in Figure 11.8 (a) and (b) may be attributed to absorption line shifts caused by temperature increases.

The effect of reduced oxygen concentration on measured decay time differed for the two

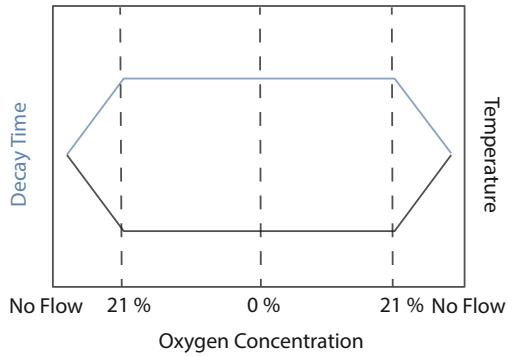

Figure 11.7: Visualization of the desired behavior of the thermographic phosphors during the oxygen sensitivity study.

phosphors. For YAG:Tm;Li, an increase in lifetime was observed, whereas YAG:Dy experienced a decrease in lifetime. The oxygen effect arises from the CTS, becoming a major mechanism for nonradiative decay in oxygen-sensitive conditions. This effect is most pronounced when the excited state is at a high-energy level, and the CTS is at a low-energy level, suggesting that the energy gap between these states is smaller for Tm^{3+} in this host material.

In a follow-up study, the tube furnace was set to approximately 1600 K and was allowed to stabilize without any gas flow into the furnace. The flow was initially set to normal air and then the oxygen content was gradually reduced every 20 min in 5% increments to pure nitrogen and then back to the initial conditions, as shown in Figure 11.7. This investigation was conducted simultaneously for both phosphors. Ideally, there should be a slight increase in the determined lifetime when the gas flow is turned on because of the cooling effects of the gas flow and should then remain constant for different oxygen concentrations and then return to the initial condition when the gas is turned off, see Figure 11.7.

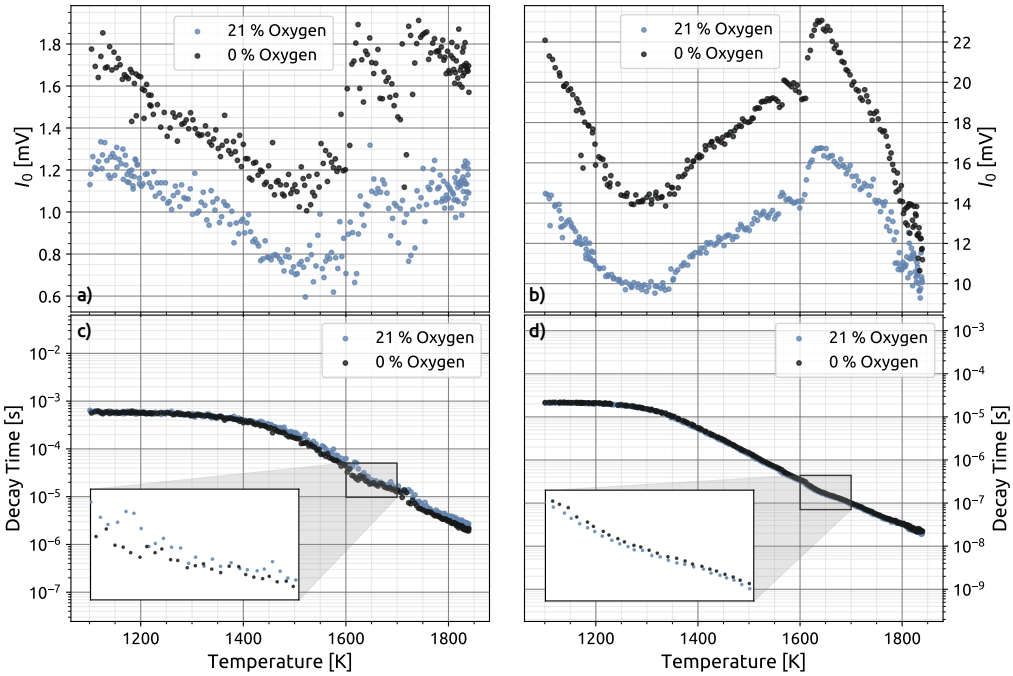

Figure 11.8: The decay time calibration for YAG:Dy and YAG:Tm;Li was conducted at oxygen concentrations of 21% and 0%. Both calibrations utilized a constant flow rate of 2 liters per minute. The decay curves were fitted using the parameters $c_1 = 0.5\tau$ and $c_2 = 4\tau$. In the figure, the top sections, labeled (a) and (b), present the parameter I_0 from the fitting process for YAG:Dy and YAG:Tm;Li, respectively. The bottom sections, labeled (c) and (d), illustrate the relationship between decay time and temperature for YAG:Dy and YAG:Tm;Li, respectively.

The maximum difference in the average determined temperature across all flow conditions was approximately 20 K for YAG:Dy and 7 K for YAG:Tm;Li when using $c_1 = 0.5$ and $c_2 = 4$, as shown in Figure 11.9. Although the reduced oxygen environment seemed to have irreversible effects over the duration studied, its impact on temperature measurements was minimal, affecting YAG:Tm;Li by less than 0.5% and YAG:Dy by 2%. The change in determined lifetime when transitioning from 21% to 0% oxygen showed a relative decrease of about 15% for YAG:Dy and a increase of 4% for YAG:Tm;Li, as illustrated in Figure 11.9(c) and 11.9(d). At 1600 K, the decay time decreased by 10% for YAG:Dy and increased by 3% for YAG:Tm;Li when the oxygen concentration changed from 21% to 0%, as indicated in Figure 11.8. This consistency across experiments highlights the reliability of the results. The superior precision of YAG:Tm;Li compared to YAG:Dy in lifetime measurements is apparent from the error bars in Fig. 11.9(c) and 11.9(d). The reduction in oxygen concentration affected the lifetime determination of the two phosphors in opposite ways, aligning with the data in Figure 11.8. While both phosphors are sensitive to oxygen with this mono-exponential fitting strategy, YAG:Tm;Li exhibits less sensitivity.

To mitigate the effects of changing oxygen concentrations, a specialized decay-time fitting

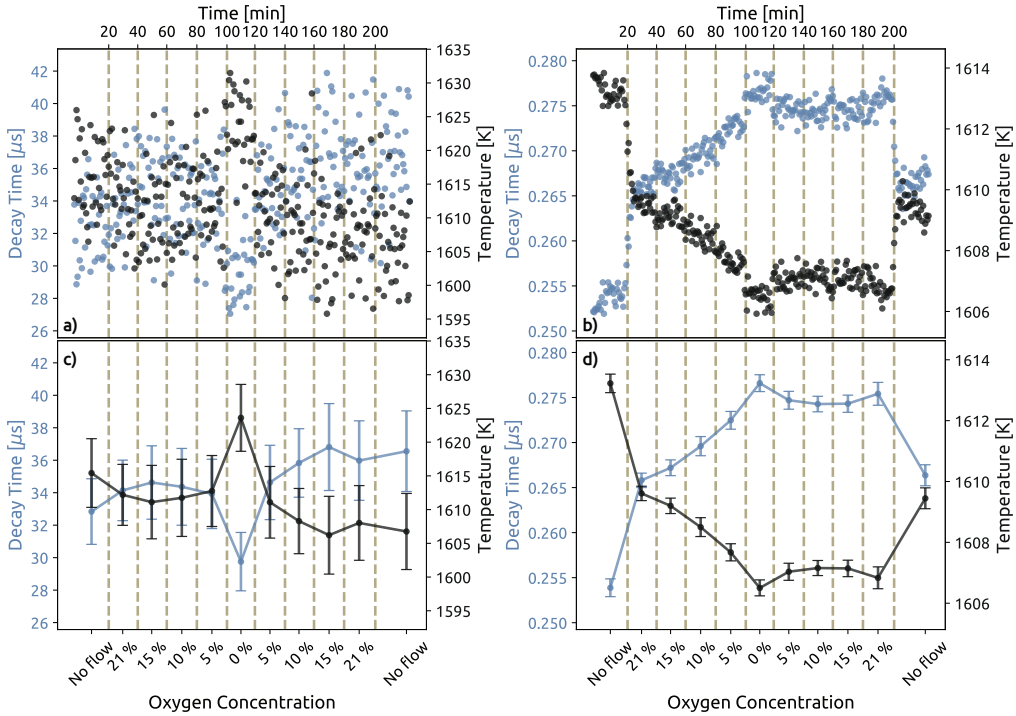

Figure 11.9: The determined lifetimes from the oxygen sensitivity study were analyzed using $c_1 = 0.5$ and $c_2 = 4$. In the upper section, scatter plots illustrate the measured lifetimes for YAG:Dy (a) and YAG:Tm;Li (b) at various oxygen concentrations, with decay times converted to temperature through calibration using an airflow. In the lower section, the data for each interval were averaged and presented along with their standard deviations for YAG:Dy in (c) and YAG:Tm;Li in (d). It is important to note the difference in temperature scales between the two phosphors.

strategy can be employed. However, this method may reduce the precision of the measurements. Figure 11.10 displays the same data as Figure 11.9 but fits the curve at a later stage, with parameters $c_1 = 1$ and $c_2 = 4.5$. For YAG:Tm,Li, the impact of decreased oxygen levels is significantly reduced and seems to be reversible, indicating that the shorter decay components are most affected. Thermocouple data in Figure 11.10(b) show a consistent temperature trend, where gas flow results in cooler temperatures due to its cooling effect. Although the gas environment's influence on YAG:Dy is also reduced, changes in oxygen concentration still produce a noticeable effect.

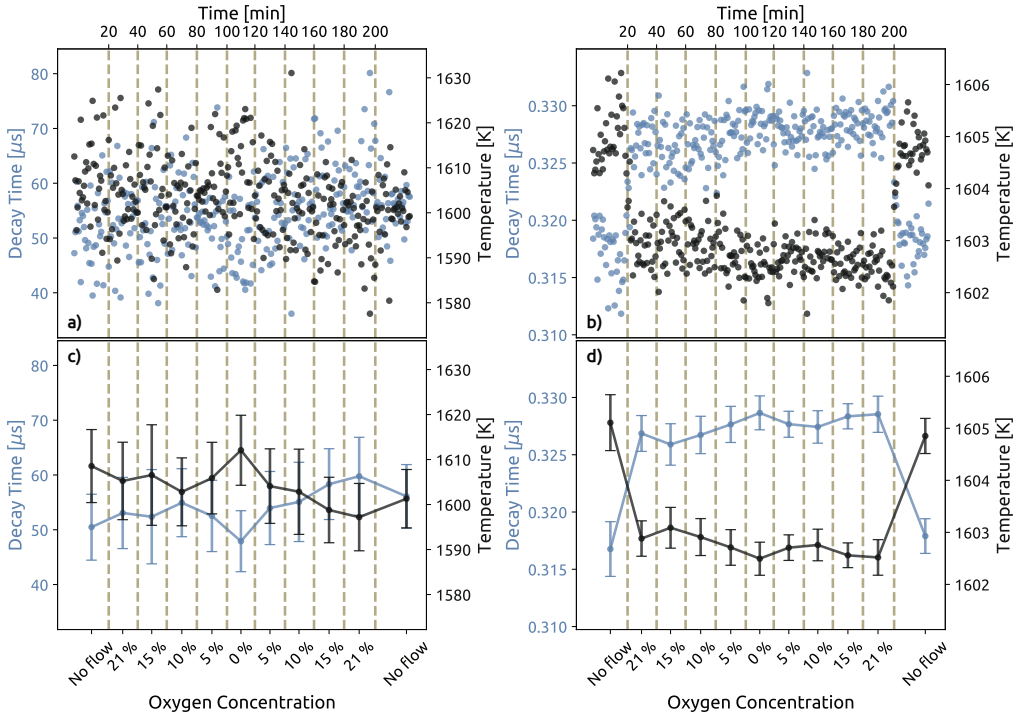

Figure 11.10: The data shown in Figure 11.9 were refitted using a later portion of the decay curve, with parameters $c_1 = 1$ and $c_2 = 4.5$. This adjustment led to a reduction in the precision of the measured decay times due to a decreased signal-to-noise ratio (SNR). For YAG:Tm;Li, the influence of oxygen concentration was significantly diminished, whereas for YAG:Dy, the effect remained noticeable, albeit to a lesser degree.

11.3 Determining Significant Decay Time Components

The sensitivity of thermographic phosphors to oxygen quenching is an important factor to consider in their application. Oxygen quenching alters the multi-exponential decay components, complicating the interpretation of luminescent signals. As previously demonstrated for YAG:Dy and YAG:Tm;Li, fitting the decay curve later can reduce sensitivity to oxygen quenching. However, further study of these decay components is needed to understand their relative strengths. Understanding and compensating for this sensitivity is essential for accurate temperature measurements, particularly in environments with varying oxygen concentrations. Therefore as part of this thesis a algorithm based on maximum entropy method (MEM) have been developed to extract the relative strengths of the decay components.

Maximum Entropy Method for Exponential Decays

Maximum Entropy Method (MEM) utilizes the principle of maximum entropy, which states that the distribution with the largest entropy is the best representation of a system. In the case of lifetime phosphor thermometry, many decay time distributions could be used to fit a decay curve adequately, but the one that best fits the data is the distribution of decay times with the highest entropy or alternatively makes the fewest assumptions about the data.

The formulation of the Maximum Entropy Method (MEM) problem follows the approach outlined in [120, 121], with the computational techniques described in [122]. The time-resolved decay data E_m can be modeled using a function $T(t)$, which includes a response function $R(t)$:

$$T(t) = \sum_{m=1}^{M} R(t_m) \cdot I(t - t_m) \tag{11.1}$$

Here, t_m is the time corresponding to the m-th data point in E_m, and M is the total number of data points. The response function $R(t)$ is determined by the experimental setup at each time t_m. In this study, the influence of the response function is ignored and is set to unity, although it is anticipated to significantly impact decay times shorter than 10 ns.

The luminescence of phosphors is modeled as a sum of discrete exponential decays $I(t)$:

$$I(t) = \sum_{i=k}^{N} \alpha_k e^{-t/\tau_k} \tag{11.2}$$

Here, α_i represents the amplitude factor for a given lifetime τ_i, and N is the number of partitions in the interval $[\tau_1, \tau_N]$. The range of decay times sets the resolution of the distribution concerning decay times, and the boundaries define the detectable range of decay times. Setting unreasonable boundaries can result in reduced algorithm accuracy.

By combining Equations (11.1) and (11.2), we can rewrite the equation as:

$$C_{m,k} = \sum_{m=1}^{M} e^{-t_m/\tau_k} \tag{11.3}$$

$$T(t_m) = \sum_{k=1}^{N} \alpha_k C_{m,k} \tag{11.4}$$

In Equation (11.4), the weightings α_k are multiplied by the unweighted decay curves $C_{m,k}$ to produce the fitted decay curve $T(t_m)$. The parameter α determines the contribution of each lifetime, and a distribution of α that models the data E is sought. The objective of MEM is to determine the weighting α of each decay curve in Equation (11.4) to best fit $T(t_m)$ to the data $E(t_m)$. The sum of the weightings α is normalized to one because all decay curves analyzed by the algorithm have peak intensities normalized to 1. The optimal distribution of α fitting E is found by minimizing the functional Λ:

$$\Lambda = \frac{\|E(t_m) - T(t_m)\|^2}{M} - \lambda S \tag{11.5}$$

where λ is a regularization parameter, and S is the entropy functional. Minimizing Λ requires minimizing both the MSE and the term $-\lambda S$, where the latter is the Shannon-Jaynes entropy multiplied by $-\lambda$:

$$S = -\sum_{i=1}^{N} \alpha_i \log\left(\frac{\alpha_i}{\beta_i}\right) \tag{11.6}$$

where β represents the previous iteration's distribution of α. The regularization parameter λ balances the emphasis on the MSE and S, and is always positive and non-zero. Solving Λ involves calculating $\nabla \cdot \Lambda = 0$, leading to a set of nonlinear equations:

$$\nabla \cdot \Lambda_i = \nabla \cdot \left(\frac{\|E(t_m) - T(t_m)\|^2}{M}\right)_i - \nabla \cdot (\lambda S)_i \tag{11.7}$$

$$\nabla \cdot \left(\frac{\|E(t_m) - T(t_m)\|^2}{M}\right)_i = \frac{\sum_{m=1}^{M}\left(-2 \cdot (E(t_m) - \sum_{k=1}^{N} \alpha_k C_{m,k}) C_{m,i}\right)}{M} \tag{11.8}$$

$$\nabla \cdot (\lambda S)_i = -(1 + \log(\alpha_i/\beta_i))\lambda \tag{11.9}$$

$$\nabla \cdot \Lambda_{N+1} = S \tag{11.10}$$

where $i = 1 : N$. To solve these equations, a Taylor expansion is performed by defining $\mathbf{x} = [\alpha_1, \cdots, \alpha_N, \lambda]$ and setting $\nabla \cdot \Lambda = \mathbf{F}(\mathbf{x})$, resulting in:

$$F_i(\mathbf{x}+\delta\mathbf{x}) = F_i(\mathbf{x}) + \sum_{j=1}^{N+1} \frac{\partial F_i}{\partial x_j}\delta x_j + O(\delta x^2) \tag{11.11}$$

This can be reformulated in matrix form as:

$$\mathbf{F}(\mathbf{x}+\delta\mathbf{x}) = \mathbf{F}(\mathbf{x}) + \mathbf{H}\cdot\delta\mathbf{x} + O(\delta\mathbf{x}^2) \tag{11.12}$$

where $\mathbf{H}$ is the Hessian matrix of size $(N+1)\times(N+1)$, and its components are:

$$H_{i,j} = \sum_{i=1}^{N}\sum_{j=1}^{N}\left(\delta_{i,j}\frac{\lambda}{x_j} + 2\sum_{m=1}^{M} C_{m,j}C_{m,i}\right), \quad i,j \le N \tag{11.13}$$

$$H_{i,j} = 1 + \log\left(\frac{x_i}{\beta_i}\right), \quad i \le N, j = N+1 \tag{11.14}$$

$$H_{i,j} = 1 + \log\left(\frac{x_j}{\beta_j}\right), \quad i = N+1, j \le N \tag{11.15}$$

$$H_{i,j} = 0, \quad i,j = N+1 \tag{11.16}$$

where $\delta_{i,j}$ is the Kronecker delta, and i denotes the row and j the column in the Hessian matrix. Also, $\lambda = x_{N+1}$. By neglecting higher-order terms and solving $\mathbf{F}(\mathbf{x}+\delta\mathbf{x}) = 0$, a set of linear equations is obtained:

$$\mathbf{H}\cdot\delta\mathbf{x} = -\mathbf{F} \tag{11.17}$$

where $\delta\mathbf{x}$ is the correction to the vector $\mathbf{x}$, derived from a Newton step. The updated solution is then given by $\mathbf{x} = \mathbf{x} + \epsilon\delta\mathbf{x}$. The parameter ϵ is chosen to minimize $\mathbf{F}$ in the descent direction $\delta\mathbf{x}$ while ensuring that $\delta\mathbf{x}$ does not produce negative values in $\mathbf{x}$. If any component of $\mathbf{x}$ is less than 10^{-10}, it is set to 10^{-10}, preventing singularity issues in the Hessian matrix. This iterative process continues until a stable solution is reached, where the mean change in $\mathbf{F}$ magnitude is less than 0.1% over ten iterations. The resulting distribution of $\boldsymbol{\alpha}$ that meets this convergence criterion represents the decay times best fitting the experimental data.

The estimates for the central lifetime and relative amplitude of the k-th decay component, $\langle\tau_k\rangle$ and $\langle\alpha_k\rangle$, are calculated as follows:

$$\langle \tau_k \rangle = \frac{\sum_{j=1}^{N_k} \alpha_j \tau_j \Delta_j}{\sum_{j=1}^{N_k} \alpha_j \Delta_j}, \quad \langle \alpha_k \rangle = \frac{\sum_{j=1}^{N_k} \alpha_j \Delta_j}{\sum_{j=1}^{N} \alpha_j \Delta_j} \tag{11.18}$$

In these equations, N_k represents the number of lifetimes contributing to the k-th peak, and Δ_j is the logarithmic spacing between lifetime values τ_j. In Figure 11.11 simulated decay curve with added Gaussian noise is analyzed the capabilities of the above described algorithm. In this example, a total of $N = 1000$ lifetimes τ_i are evenly distributed in logarithmic space between $[1 \times 10^{-9}, 1 \times 10^{-5}]$. This algorithm has been used in the following works [123, 11, 12, 124]

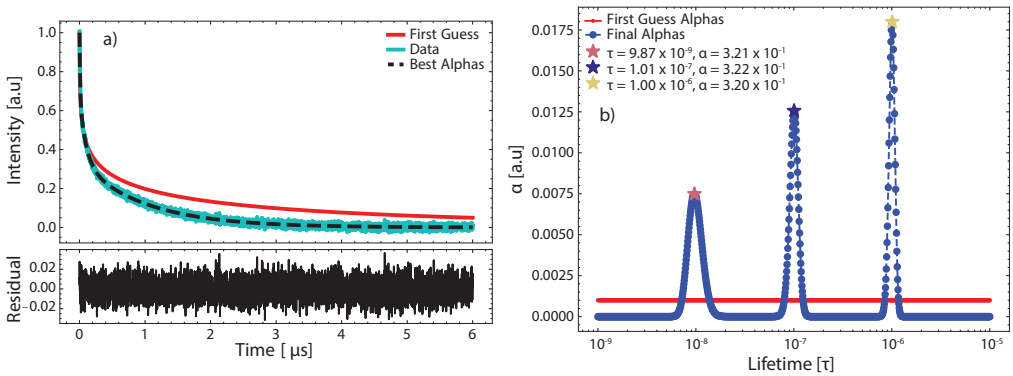

Figure 11.11: In panel (a), a simulated decay curve is presented, consisting of three decay components with constants $[1 \times 10^{-8}, 1 \times 10^{-7}, 1 \times 10^{-6}]$, each contributing equally. Gaussian noise was added to mimic real experimental conditions, resulting in a SNR of 100. The red line represents the initial guess for the alpha vector, which assumes equal contribution from each of the guessed decay time component. The black dashed line shows the optimal alpha distribution that best fits the data. In panel (b), the distribution of decay time components corresponding to the optimal alphas is displayed. Each peak is labeled with its decay time and its relative contribution to the overall decay curve calculated using Equation (11.18).

Observation of Decay Time Components Shifts of YAG:Tm;Li and YAG:Dy

Figure 11.12 presents the results of the MEM analysis, summarizing the average data for oxygen concentrations of 21%, 5%, and 0%, as depicted in Figure 11.9 and 11.10. The dashed lines in the close-up views of Figures 11.12(a) and 11.12(b) represent the average lifetimes determined at 0% oxygen for each fitting approach and phosphor type. At lower oxygen levels (0% and 5%), the shorter decay components, in the range of 10^{-9} to 10^{-8} seconds, diminish for both phosphors. Concurrently, the longer decay components, crucial for phosphor thermometry, exhibit a relative shift.

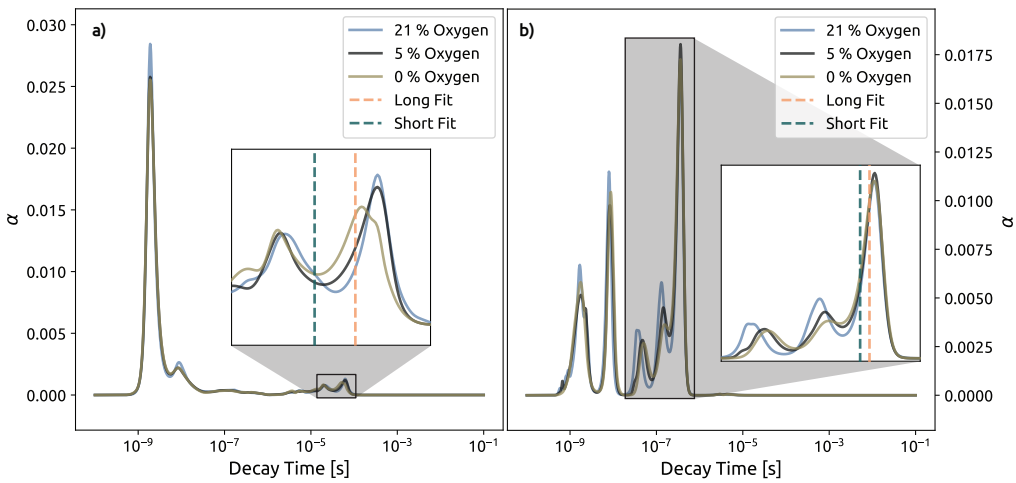

Figure 11.12: Decay time distribution from MEM analysis. The MEM analysis for each decay curve was averaged when going from 21%, 5%, and 0% oxygen for the data presented in Figure 11.9 and 11.9 for YAG:Dy (a) and YAG:Tm;Li (b).

In Figure 11.12(a) (YAG:Dy), the close-up reveals two decay time components on either side of the lifetime fits, showing that both were considered in the fitting process. When the oxygen concentration decreases from 21% to 0%, the right-side decay component near the lifetime fits shortens by 18% compared to the 21% oxygen level, resulting in a reduced determined lifetime for both fitting windows. Similarly, in Figure 11.12(b) (YAG:Tm;Li), the two rightmost components in the close-up are used for determining the lifetime with a mono-exponential fit. As oxygen levels drop to 5% and 0%, the two leftmost components decrease in relative significance and shift to longer decay times, while the rightmost component remains unchanged.

These findings indicate that the relative contributions of the lifetime components for both phosphors vary with oxygen concentration. Specifically, for YAG:Tm;Li, when applying the long fit, the analysis largely relies on a single lifetime component, which remains unaffected by changes in oxygen concentration, resulting in minimal sensitivity to oxygen. This dependency on a single lifetime is further evidenced by the alignment between the calcu-

lated lifetime using the long fit and the peak decay time of the longest lifetime component seen in the close-up of Figure 11.12(b). Thus, the sensitivity of lifetime measurements to oxygen concentration is highly influenced by the method of decay time analysis used. It is important to note that this oxygen sensitivity is most pronounced between 0% and 5% oxygen concentration, as shown in Figure 11.9 and 11.10.

12 Laser Diagnostics in Plasma Applications

Laser diagnostics play a vital role in the study of plasmas, enabling precise, non-intrusive measurements of key properties such as temperature and number density [125]. Optical methods, including Laser-Induced Fluorescence (LIF), Rayleigh scattering, and Raman scattering, allow for high-accuracy probing of plasmas without disrupting the system. However, the intense brightness of plasma can complicate signal detection, making it difficult to differentiate laser-induced signals from the plasma's luminescence [126].

This thesis investigates non-equilibrium plasmas, particularly dielectric barrier discharges (DBD) and gliding arcs. It focuses on developing techniques to extract laser-induced signals in high-scattering environments, enabling the collection of laser-induced fluorescence lifetime imaging data. This data is essential for applying quenching corrections in fluorescence imaging. The methods were then employed to study the quenching behavior of OH radicals in a gliding arc plasma, utilizing 3D emission tomography to spatially correlate the fluorescence signal with the arc. This approach provides a detailed analysis of OH quenching relative to the arc. Furthermore, fluorescence lifetime imaging data was converted to temperature using a fluorescence lifetime model, revealing the spatial distribution of temperature derived from fluorescence lifetime imaging. Rayleigh thermometry was subsequently applied to the same gliding arc setup to examine the surrounding gas temperature in relation to OH fluorescence by integrating fluorescence imaging and Rayleigh thermometry. Additionally, methyl radicals were analyzed in the context of methane reformation in a DBD plasma using photofragmentation techniques.

12.1 Fluorescence Lifetime Imaging Through Scattering Media

While non-laser-induced background signals can often be estimated and subtracted, addressing scattered light requires a different strategy. Scattered light is particularly problematic in studies involving scattering media, both when the laser interacts with the object and as the signal travels to the detector. To tackle this issue, structured illumination techniques have been developed [83, 85]. These methods isolate singly scattered light, which maintains its structured pattern, while filtering out multiply scattered light, which loses this information.

Structured illumination is typically effective in reducing image blur caused by scattered light. However, in fluorescence lifetime imaging , signals from different areas may have varying lifetimes, and multiple scattering can mix these signals, complicating the accurate measurement of lifetimes within the probe volume, see Figure 12.1. Consequently, the measured lifetime might not truly represent the actual lifetime at that specific location.

In this thesis, we explore whether combining structured illumination with spatial lock-

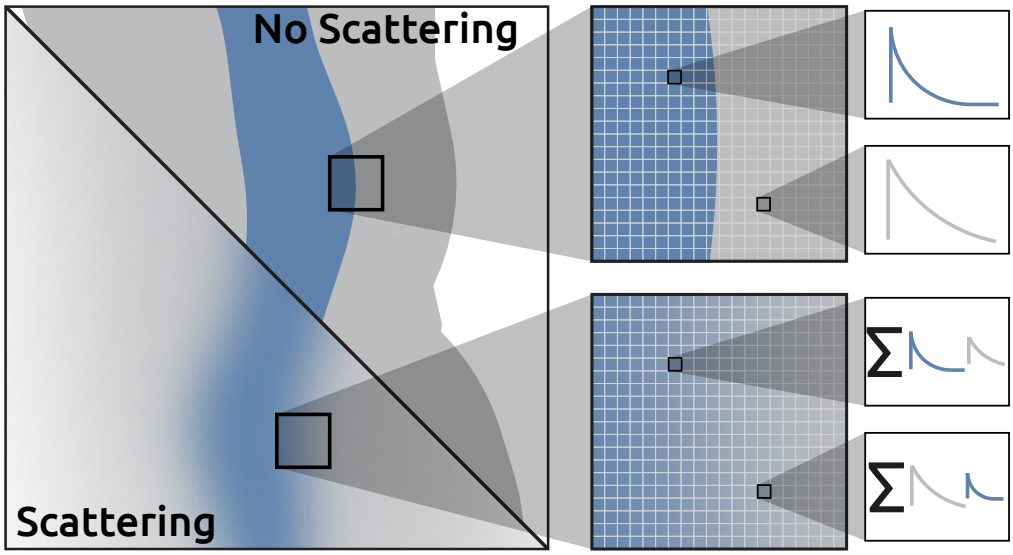

Figure 12.1: The upper section illustrates a scenario without scattering, where the short (blue) and long (gray) fluorescence lifetimes in the detector plane can be directly correlated to specific locations in the image plane. However, in the lower part of the figure, where scattering is present, contributions from adjacent areas in the image plane blend into the detected luminescence lifetime in the detector plane, resulting in reduced spatial resolution. As a result, the signal in these pixels becomes a composite of signals from nearby locations.

in analysis can suppress multiply scattered light to facilitate accurate lifetime imaging in scattering environments. The fluorescence-lifetime images are obtained using the DIME technique, as detailed in Section 8.

To demonstrate these methods, we conducted an experiment using a flow system that combines a stable laminar jet with a co-flow of gas mixtures containing different levels of oxygen. This setup is depicted on the right side of Figure 12.2. In the experiment, a vertical jet of toluene-seeded air was centered within a porous plug. Surrounding this jet, a co-flow of nitrogen-enriched air, also seeded with toluene, was introduced through the porous plug to stabilize the laminar flow. This stabilization allowed for the accumulation of images, resulting in high-quality data with a strong signal-to-noise ratio, see experimental setup in Figure 12.2. The gas mixtures were prepared by bubbling the gases through liquid toluene, ensuring consistent toluene seeding.

The experimental setup produced a fluorescence lifetime imaging image that revealed three distinct regions with varying lifetimes. The central jet region was expected to show a lifetime of 0.65 ns, while the surrounding co-flow region was anticipated to have a lifetime of 1.8 ns, consistent with previous studies. Between these two regions, a transition zone was observed, where lifetimes ranged from 0.65 to 1.8 ns due to the mixing of the jet and co-flow gases.

Experiments were conducted both with and without the scattering medium in the detection line, and the results are illustrated by the accumulated PLIF images shown in Figure 12.3

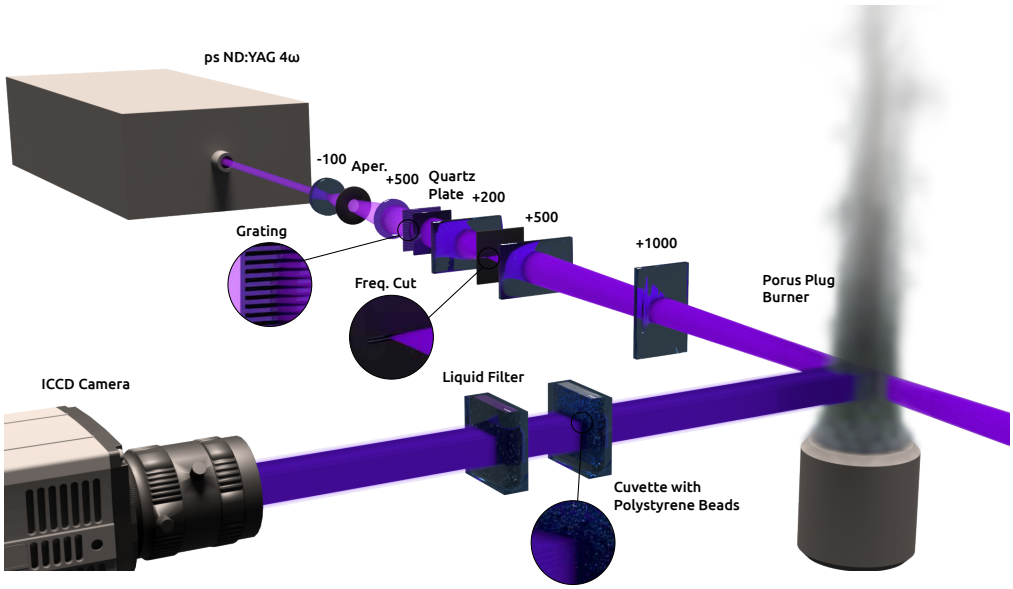

Figure 12.2: A schematic of the experimental setup is shown, with all dimensions in millimeters. A water-filled quartz cuvette, positioned between the gas flow and the ICCD camera, was seeded with polystyrene spheres to create scattering within the imaging system.

(a) and (b), respectively. In both images, the modulation pattern is clearly visible. The gas jet, positioned at the center, appears slightly darker than the surrounding gas, which is attributed to the shorter fluorescence lifetime of the toluene-seeded air. This reduction in lifetime results in a decreased fluorescence signal. The introduction of polystyrene spheres as a scattering medium leads to (i) a degradation in image contrast and (ii) a decrease in signal intensity due to light scattering.

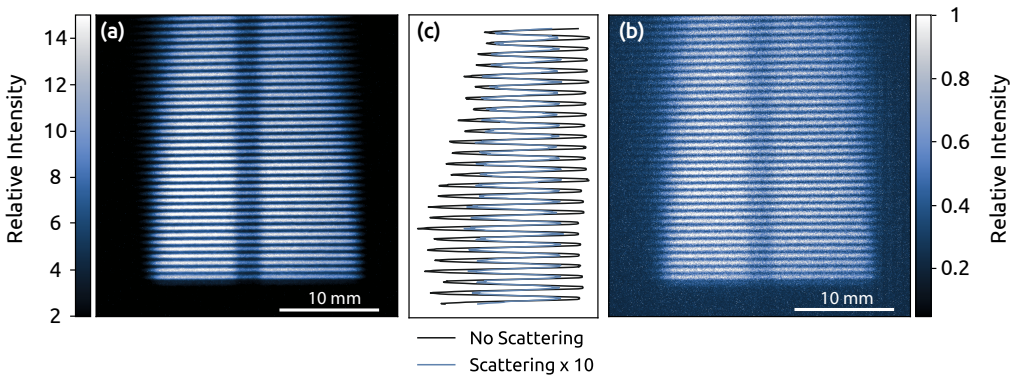

Figure 12.3: Raw PLIF images show a contrast of approximately $M \approx 0.44$ in (a) without additional scattering. (b) When imaging through a scattering medium (OD ≈ 1), the contrast is reduced to $M \approx 0.37$. (c) The cross-sectional data from the central radial position illustrate the difference in modulation between images (a) and (b). It is important to note that the signal intensity is roughly an order of magnitude lower when collected through the scattering medium.

FLI images were generated using both the conventional and lock-in methods with DIME, with the results presented in Figure 12.4. Both methods successfully capture the desired characteristics, where the signal in the central jet exhibits a shorter lifetime compared to the co-flow. However, the lifetimes in the jet, as determined by the conventional analysis (12.4 (a)), are overestimated by a factor of two relative to the expected values. In the co-flow, where lifetimes are expected to be symmetrical around the jet, a noticeable slanted bias is observed in the lifetime measurements (12.4 (b)). In contrast, the combination of structured illumination and spatial lock-in analysis yields fluorescence lifetimes that closely align with the expected values, as illustrated in 12.4 (b) and (c).

The overestimation of lifetimes in the conventional analysis arises from the method's inability to eliminate the background intensity offset, a challenge inherent to all intensity-based techniques. This issue is particularly problematic in scattering environments, where it leads to a non-uniform background. As a result, the scattering-induced background cannot be accurately determined from any reference image or blank recording. Although the average intensity offset in the conventional image was adjusted by subtracting the intensity value at a height of 3 mm, where no laser illumination occurred, this correction is not entirely effective. The remaining background from scattering introduces errors in the lifetime evaluation.

It's important to note that the lock-in analysis employs a frequency filter, which can reduce the spatial resolution of the original image Figure 12.4. Therefore, this method should be used with caution when dealing with objects that have fine image structures. In challenging environments, capturing such details and strong image gradients is typically difficult due to suboptimal imaging conditions. However, in the current scenario, these details are already compromised by signal scattering. Under these circumstances, applying spatial lock-in analysis does not further degrade the image resolution.

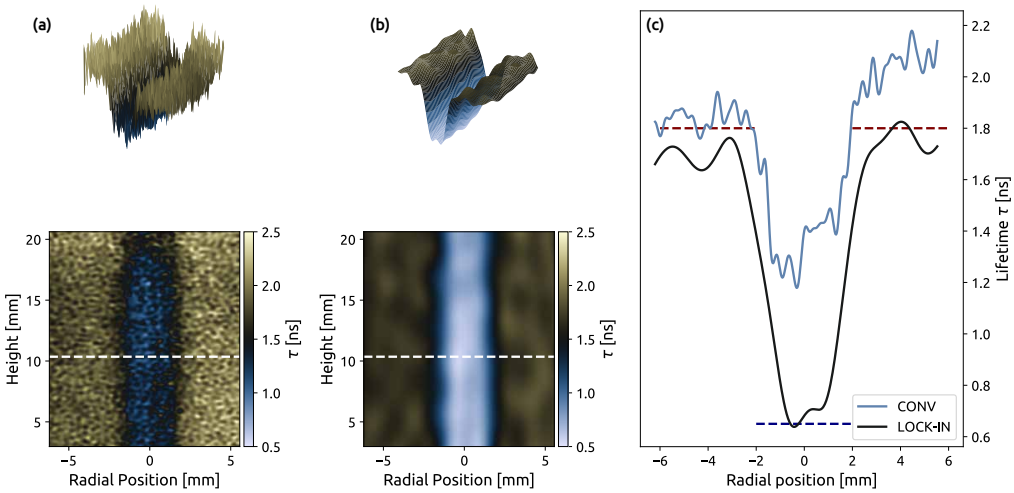

Figure 12.4: Fluorescence lifetime images are shown for (a) the conventional method and (b) the lock-in method. The 3D plots display the same data as their corresponding images. In (c), data along the dashed white line in each image were extracted and compared in a line plot. The red and blue dashed lines represent the expected values for the co-flow region (red) and the central jet (blue).

12.2 FLI and 3D Tomography of Gliding Arc

The industrial applications of gliding arc plasma are diverse, ranging from air pollution control, where it assists in the decomposition of hazardous gases [127], material processing, including surface modification and polymerization, as well as in energy applications like hydrogen production through methane reforming [128].

However, to optimize these applications and fully harness the potential of gliding arc plasmas, a deeper understanding of the plasma chemistry, reaction kinetics, and energy efficiency is essential [129]. The interaction between plasma species and target materials is complex and requires precise control to achieve desired outcomes efficiently. Advancing our knowledge in these areas is crucial to developing more efficient, sustainable, and cost-effective plasma-based chemical processes in various industrial sectors.

Emission 3D Tomography

Traditionally, 2D optical diagnostics have been the standard approach for studying gliding arc discharges. However, the inherently three-dimensional structure of these discharges suggests the need for techniques that can provide comprehensive 3D data. Earlier 3D studies have explored aspects such as hydroxyl radical distributions using the FRAME technique and plasma column lengths through particle tracking velocimetry (PTV) [130].

In response to the limitations of 2D methods, in this work 3D emission tomography was applied to investigate gliding arc discharges. This technique captures volumetric luminosity data across the entire observed region, focusing on emissions primarily from N_2 chemiluminescence in the visible spectrum. By acquiring 3D data, this approach enables more accurate analysis and characterization of critical attributes like arc position, geometry, length, and topology parameters that are typically difficult to assess without volumetric data and are essential for calculating physical properties related to plasma discharges[99, 26].

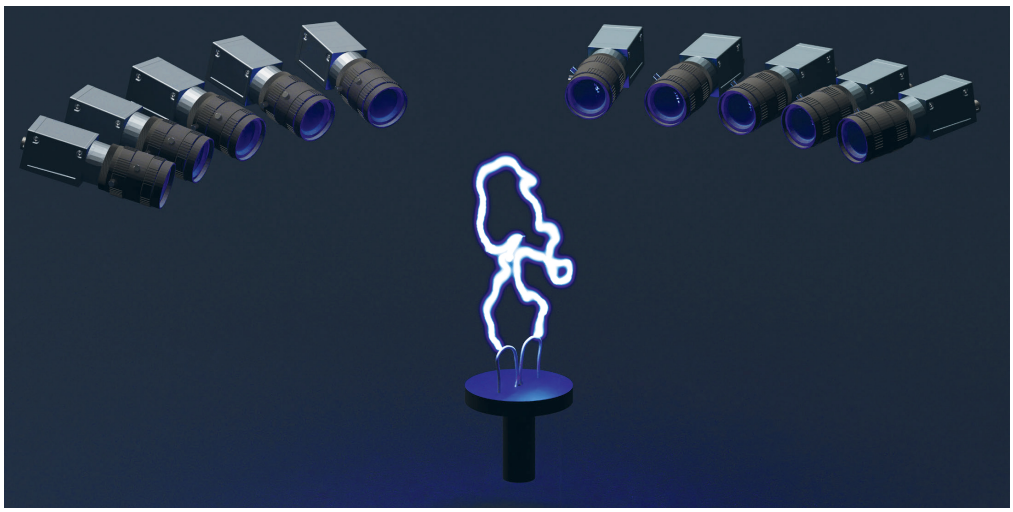

Figure 12.5: Schematic of the emission tomography configuration and electrode layout. The illustrated gliding arc is a reconstruction derived from actual discharge data using emission tomography.

The gliding arc discharge system operates in an open-air environment and consists of three main components: the electrodes, the airflow mechanism, and the power supply. The electrodes are made from hollow stainless-steel tubes, each with an outer diameter of 6 mm, and are securely mounted on a Teflon plate, as depicted in Figure 12.5. These electrodes are internally cooled by water, with one electrode connected to the high-voltage power supply to act as the active electrode, while the other serves as the grounded electrode. Airflow is directed between the electrodes through a 3 mm diameter nozzle located at the center of the Teflon plate. The airflow rate is controlled via a mass flow controller (MFC), and the system was examined under four different airflow rates 10, 20, 30 and 40 l/min.

Luminescence field measurements were captured using 10 commercially available CMOS cameras arranged in a semicircle around the electrodes, as depicted in Figure 12.5. The reconstructed volume was discretized into 221x221x221 voxels, with a spatial resolution of 0.5 mm per voxel. This resolution was selected to balance detail capture with computational efficiency.

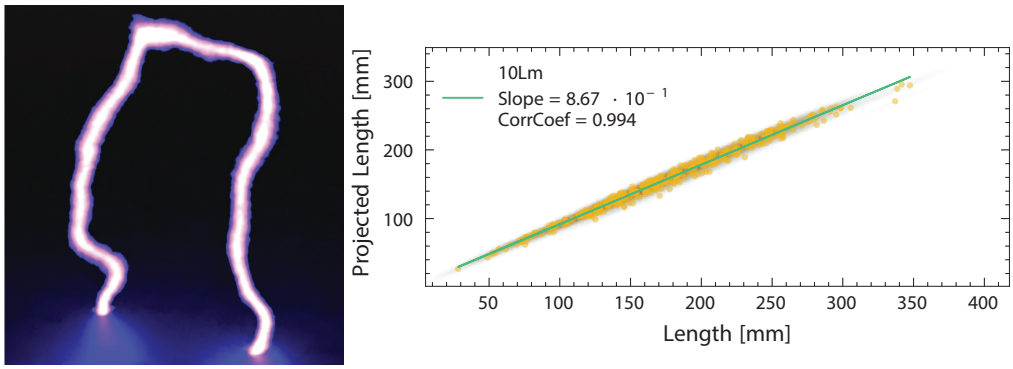

Figure 12.6: The left panel displays a tomographic reconstruction for the 10 l/min case, while the right panel shows the 3D length of the arc along the x-axis and the projected 2D length along the y-axis for the same case. The scatter points represent individual measurements, and the green line indicates a linear fit with the corresponding slope value. A slope less than one, as observed here, suggests that the projected length is approximately 13% shorter than the 3D length.

The 3D arc length is caluclated by finding the start and end points within the bottom slice of the reconstructed probe volume Figure 12.6. Dijkstra's algorithm, using the Python package iGraph, finds the shortest path through voxels with 26-connectivity, weighted by the inverse cube of their average intensity to follow the arc's center. The choice of weight is based on arc length convergence. The calculated arc path is validated against a projected image from the CMOS camera. A degree-20 B-Spline smoothing, applied with 'scipy.interpolate', generates the final set of coordinates, and the arc length is calculated by summing the Euclidean distances between these points.

Comparisons between the quantified 3D length and 2D length were made by projecting the reconstructed arc path along the axis perpendicular to the anode-cathode plane, generating an optimal image for extracting the 2D arc length. Figure 12.6 demonstrate the expected trend of underestimating the arc length when using 2D projections. Discrepancies were approximately 13% at 10 L/min, 14% at both 20 L/min and 30 L/min, and up to 15% at the highest tested flow rate of 40 L/min. This discrepancy arises from the loss of depth information in 2D, which is influenced by the degree of curvature in the arc.

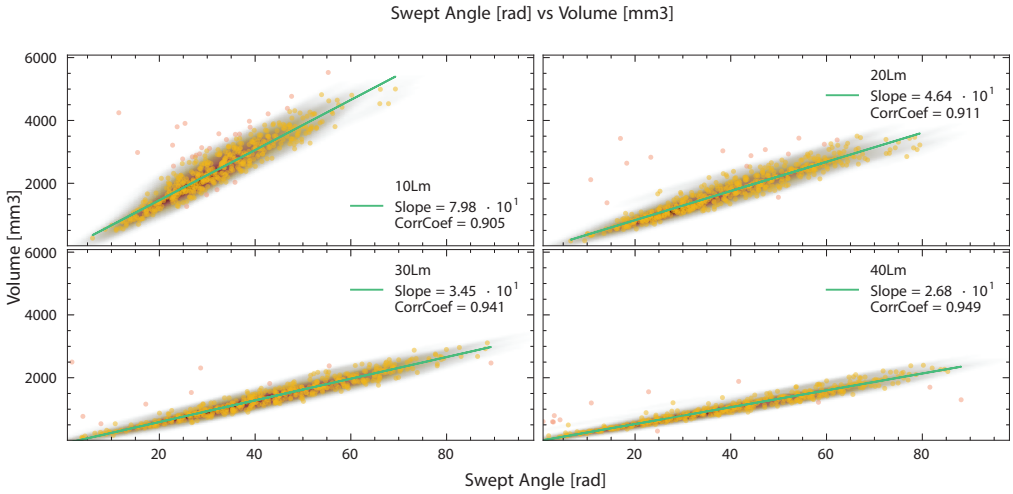

Figure 12.7: The swept angle plotted towards the volume of the arc for the studied flow-rates.

Additionally, the 3D information from the arcs allow for extraction of multitudes of parameters, volume, surface area, curvature mean cross-sectional area just to name a few. An example is shown in Figure 12.7. Here the swept angle and the volume of the arcs are plotted against each other to study the correlation between these parameters. The swept angle is a measure of how much the arc curves in 3D space, which is extracted from the path length, for a semicircle corresponds to a value of π radians of swept angle. The arc volume was calculated by applying a global threshold to remove reconstruction artifacts. Voxel values exceeding this threshold and connected to the previously identified arc coordinates, determined using a 6-connectivity connected components algorithm, were included as part of the volume. The total arc volume was then obtained by multiplying the number of identified arc voxels by the volume of each voxel.

In Figure 12.7, it is evident that as the flow rate increases, the arc volume decreases while the swept angle increases. Higher flow rates shorten the residence time, leading to smaller structures and a stronger influence of forced convection on arc dynamics. This results in a longer, more wrinkled discharge channel with greater vertical extension. The increased turbulence at higher flow rates further reduces the residence time, limiting the plasma discharge's impact on the surrounding gas and decreasing the cross-sectional area of the luminous discharge channel. Since the arc volume is roughly proportional to the cross-sectional area, the volume continues to decrease with higher flow rates, despite the arc becoming longer.

Fluoresence Imaging of OH

The 3D tomographic reconstructions of the gliding arcs in Figure 12.9 are shown alongside the OH radical distributions relative to the plasma channel. The OH distributions, captured through laser-induced fluorescence imaging, clearly indicate that the OH region consistently surrounds the plasma channel. The intersecting cross-section between the fluorescence imaging and the 3D reconstruction from Figure 12.9(a) is depicted in Figure 12.10.

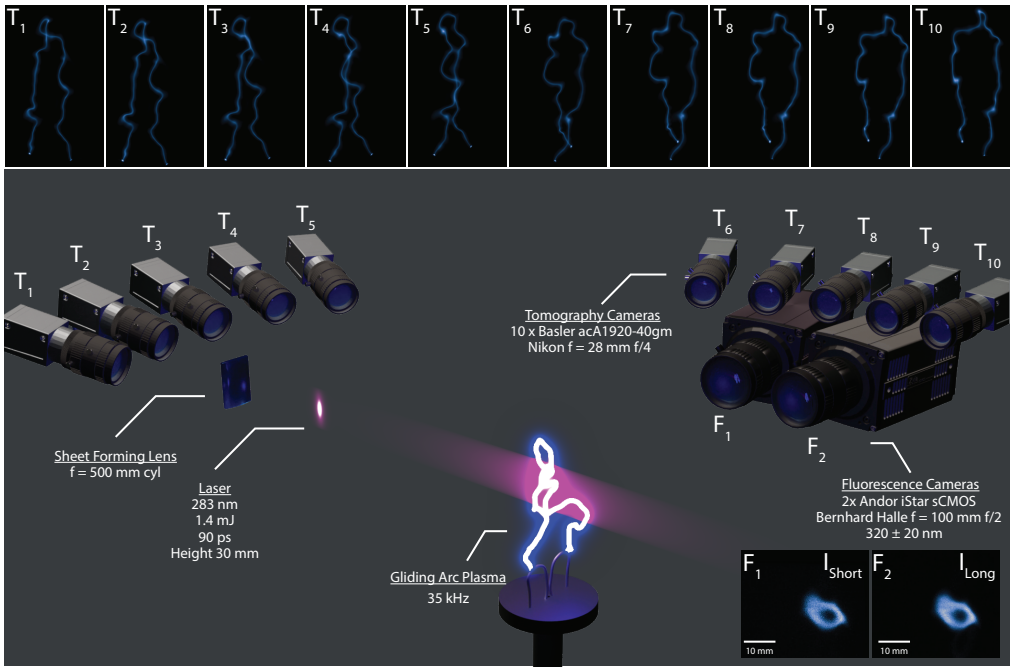

Figure 12.8: Modified experimental setup from Figure 12.5 which now includes the a picosecond laser to excite OH.

As the flow rate increases, the OH fluorescence structure associated with the gliding arc discharge decreases in size, with a 60% reduction in cross-sectional area observed from 10 l/m to 40 l/m. At lower flow rates, the OH distribution is smooth and circular due to diffusive effects from the plasma channel. However, higher flow rates introduce turbulence, leading to deformation and a thinner, smaller fluorescence structure.

A distinct central hole in the OH structure, where OH production from water vapor occurs, exhibits approximately four times lower intensity than the surrounding ring, as shown in the line plot in Figure 12.10. The red dots mark the hole's center, determined by 3D tomography. The intersection angle, displayed in the bottom right corner, affects the hole's shape, with lower angles causing it to appear elongated and elliptical.

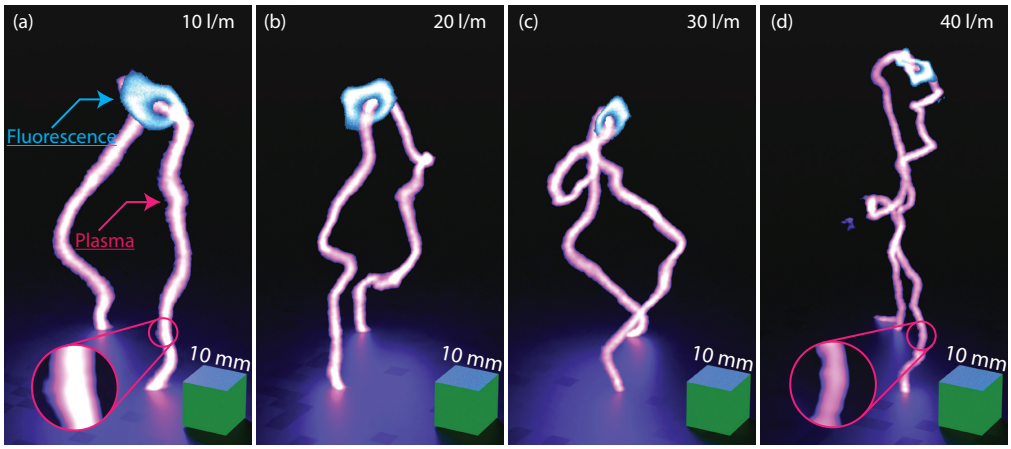

Figure 12.9: Representative fluorescence images from the experiments are combined with their corresponding three-dimensional tomographic reconstructions, shown from 10 l/m in (a) to 40 l/m in (d). Complete three-dimensional tomography renderings are available in Supplementary Material 1, highlighting the interaction between fluorescence structures and the three-dimensional tomographic reconstructions in three-dimensional space.

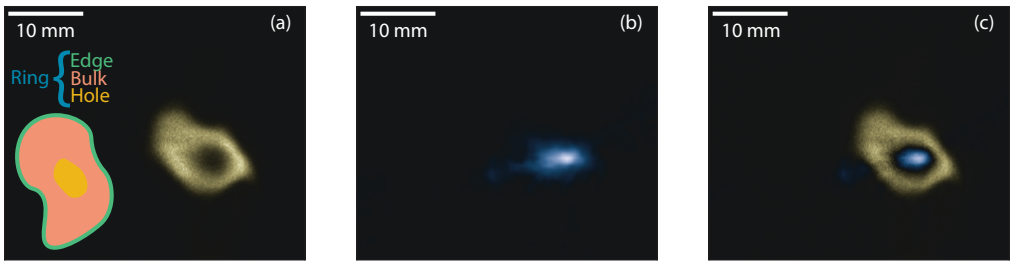

Figure 12.10: The raw data from the fluorescence image and the intersecting cross-section of the three-dimensional tomography, shown in Figure 12.9 (a), are presented in panels (a) and (b), respectively. A composite image, created by normalizing and subtracting (a) and (b), is shown in panel (c), where the blue and brown regions represent the tomography and OH fluorescence signals, respectively. Panel (a) also provides a graphical explanation of the edge, bulk, hole, and ring features.

The region around the gliding arc, particularly near the OH distribution's center, exhibits non-thermal characteristics within a 1 mm radius, where intense fluorescence from N_2^* and OH^{**} is observed [131]. Energy dissipation near the arc shows a discrepancy between vibrational and translational energy, suggesting that OH in the central region may not be in the ground state, potentially escaping detection. The continuous dissociation of OH within the hole could be a result of thermal processes or electron dissociation. Upon plasma power disconnection, the central hole fills with ground-state OH, indicating recombination or de-excitation [132]. Previous studies have also suggested localized variations in chemical production and loss channels of OH as factors in distribution dynamics [133], though experimental conditions differ significantly. Further investigation is needed to understand the role of thermal equilibrium and chemistry in shaping radical distributions in gliding arc plasma.

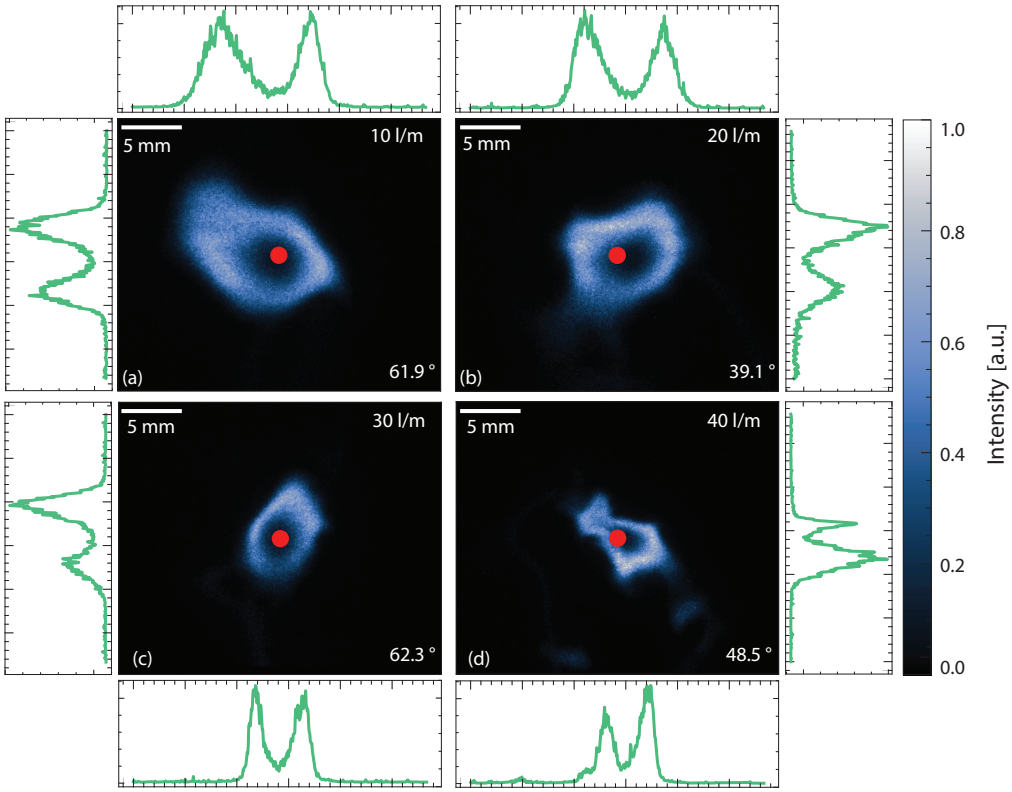

Figure 12.11: Fluorescence images captured by the Long camera for the four flow rates are shown in panels (a) to (d). Each image is accompanied by line graphs that present data extracted from the center of the red dots in both vertical and horizontal directions. The red dots indicate the arc's center, as determined by three-dimensional tomography. The intersection angle between the laser and the plasma arc is provided in the bottom right corner of each figure.

Fluorescence Lifetime Imaging of OH

The image in Figure 12.11 (a) is analyzed using the DIME algorithm, resulting in a two-dimensional fluorescence lifetime image shown in Figure 12.12 (b). The analysis reveals spatial variation in lifetime, with the outer edge displaying a shorter lifetime compared to the hole, while the bulk of the ring-like structure remains relatively uniform. Data from the outer edge, hole, and bulk of the OH ring are presented in Figure 12.10 and summarized in Table 4. The analysis shows that as the flow rate increases, the average lifetime in the ring decreases by approximately 400 ps, indicating stronger quenching effects. At lower flow rates, the arc behaves like a glow discharge with non-thermal characteristics, but at flow rates above 40 l/m, it transitions to a spark-type discharge. This transition, influenced by high Reynolds number gas, reduces residence time and system temperature, leading to cooling and contraction of the surrounding gas, which becomes more thermal while the core remains non-thermal. The increased quenching at higher flow rates is partly due to

lower gas temperatures, with the decrease in fluorescence lifetime being more pronounced at the structure's outer edge and within the central hole.

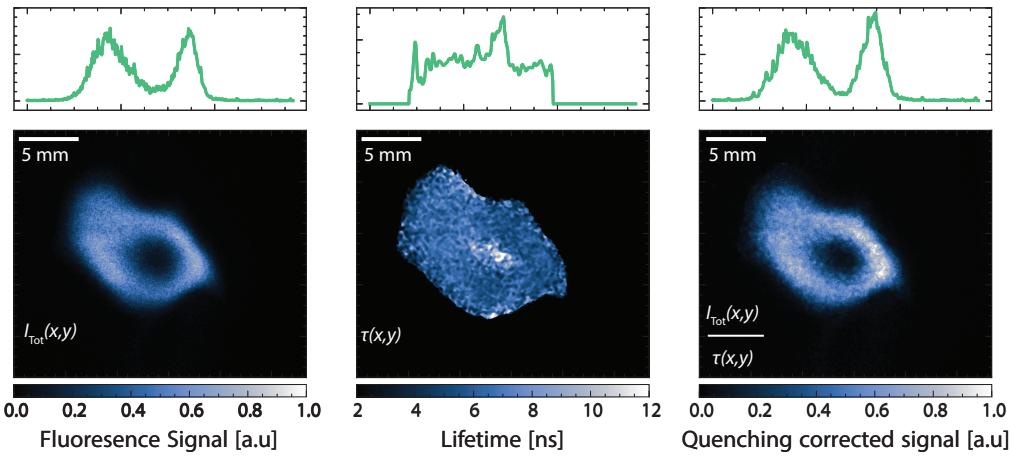

Figure 12.12: Quenching corrected fluorescence imaging, in panel (a) displays a fluorescence image sourced from the 10 l/m flow rate, identical to the depiction in Figure 12.11 (a), this image represente the total emission from the laser induced fluoresence $I_{\text{Tot}}(x, y)$. Panel (b) presents the corresponding lifetime image, $\tau(x, y)$ obtained using the Dual Imaging and Modelling Evaluation algorithm. Finally, panel (c) showcases the fluorescence image after quenching correction has been applied.

The image in Figure 12.12 (a) can be corrected for local variations in collisional quenching using the corresponding lifetime image in Figure 12.12 (b). This is done by dividing image (a) by image (b), resulting in the quenching-corrected image $I_0(x, y) = \frac{I_{\text{Tot}}(x,y)}{\tau(x,y)}$, shown in Figure 12.12 (c). The intensity $I_0(x, y)$ is proportional to the OH number density, allowing direct comparison of image intensities after correction. While the overall shape in Figure 12.12 (c) resembles that in Figure 12.12 (a), the cross-section reveals that intensity was overestimated in the hole before correction. Quenching correction at the OH-distribution's outer edge, where lifetime is slightly longer, does not significantly alter the shape, as OH density is relatively low there. Overall, quenching correction has minimal impact on the OH distribution within the investigated parameter range.

Table 4: Fluorescence lifetime measurements for different flow rates. Data acquired with MCP.PMT contain signal from all parts of the OH-distribution structure.

Flow Rate	Ring [ns]	Edge [ns]	Bulk [ns]	Hole [ns]	MCP-PMT [ns]
10 l/m	5.9 ± 1.5	5.8 ± 2.8	6.0 ± 1.4	8.1 ± 2.7	5.9 ± 0.2
20 l/m	5.8 ± 1.6	5.5 ± 2.7	5.9 ± 1.5	7.2 ± 2.5	NA
30 l/m	5.7 ± 1.7	5.2 ± 2.7	5.8 ± 1.6	6.9 ± 3.2	NA
40 l/m	5.5 ± 1.8	5.1 ± 2.8	5.6 ± 1.7	7.0 ± 2.8	NA

Quenching correction was applied to images from all flow rates, and a statistical analysis, summarized in Table 5, reveals key trends. The relative number density in the bulk decreases by about 21% as the flow rate increases from 10 l/m to 40 l/m. In contrast, the relative

number density at the edge and hole regions increases with higher flow rates. As the flow rate rises, the intensity gradient of OH increases, particularly along the edges. The reduced residence time and interaction with turbulent air cause OH structures to contract, limiting diffusion and raising the relative number density at the edges.

Table 5: Relative number density in different regions at various flow rates. All values is in the unit of detector counts.

Flow Rate	Ring [10^3]	Edge [10^3]	Bulk [10^3]	Hole [10^3]
10 l/m	2.01 ± 1.89	0.89 ± 0.68	3.23 ± 1.93	0.67 ± 0.34
20 l/m	1.99 ± 1.85	0.97 ± 0.79	3.01 ± 1.98	0.74 ± 0.71
30 l/m	1.84 ± 1.88	1.03 ± 0.89	2.98 ± 2.09	0.83 ± 0.95
40 l/m	1.65 ± 1.59	1.05 ± 0.89	2.48 ± 1.84	0.95 ± 1.02

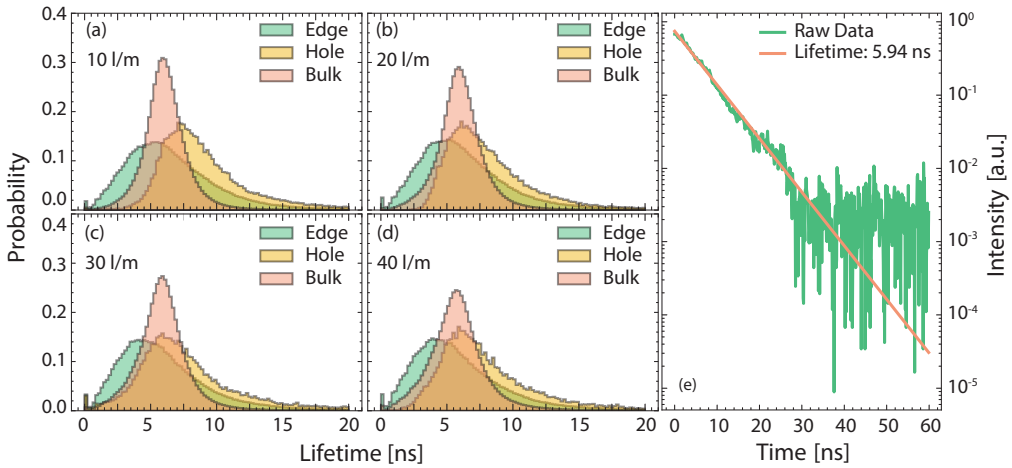

Figure 12.13: Lifetime statistics displayed in panels (a) to (d), with data extracted from the hole, edge, and bulk regions. Panel (e) features a representative decay curve from 10 l/m, recorded by the Microchannel Plate Photomultiplier Tube, along with a mono-exponential fit.

Fluorescence lifetime measurements can be used to estimate temperatures in the surrounding gas, with some assumptions. Sensitivity analysis indicates that O_2 and N_2 are the primary collisional quenching partners for OH, with their relative concentrations changing only marginally. Therefore, variations in fluorescence lifetime are mainly attributed to temperature changes at different flow rates. The key assumption is that collisional velocity remains thermally characteristic.

The quenching behavior of OH fluorescence by major air species, specifically N_2, O_2, and H_2O, was simulated and compared with experimental data[134]. Quenching cross-sections were determined using empirical formulas from Heard & Henderson [135].

$$k_Q = \langle v(T) \rangle \sigma_Q(T) \tag{12.1}$$

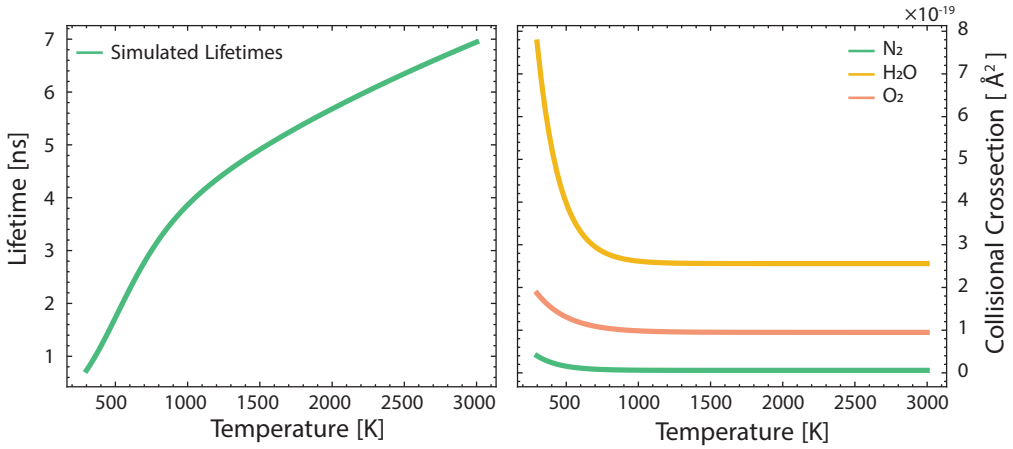

Figure 12.14: The left panel shows the fluorescence lifetime of OH in air, with major quenching partners being N_2, O_2, and H_2O at atmospheric pressure. The right panel depicts the quenching cross-section of OH due to collisions with N_2, O_2, and H_2O as a function of temperature.

where $\langle v \rangle$ is the average thermal velocity, and σ_Q is the temperature-dependent quenching cross-section. The average thermal velocity, $\langle v \rangle$, is given by $\sqrt{\frac{8k_BT}{\pi\mu}}$, with k_B as the Boltzmann constant, T as the temperature, and μ as the reduced mass of the colliding molecules. The total quenching rate was calculated using:

$$Q = \sum_i k_{Qi} N_i \tag{12.2}$$

where k_{Qi} is the quenching rate constant for species i, and N_i is the number density of that species. The fluorescence lifetime was then determined using $1/(A + Q)$, where A is the Einstein coefficient for OH, valued at 1.467×10^6 s^{-1} [136]. Using the determined fluorescence lifetimes in Table 4 and applying the above model in Figure 12.14 the derived temperature results are shown in Table 6.

Table 6: Temperature in Different Regions of OH fluorescence structure at Various Flow Rates derived from the fluoresence lifetime.

Flow Rate	Ring [K]	Edge [K]	Bulk [K]	Hole [K]
10 l/m	2160	2080	2230	4100
20 l/m	2080	1870	2160	3230
30 l/m	2010	1680	2080	2960
40 l/m	1870	1610	1940	3040

The central region of the arc is the hottest, with the plasma and gas gradually cooling as they move radially outward toward the edge of the OH distribution. During these experiments, the humidity level was measured at 40%, and an ionization/dissociation degree of

approximately 1% is assumed. The analysis indicates that the temperature derived from the measured lifetimes is around 2200 K at the lowest flow rate, decreasing with higher flow rates due to reduced residence time, which limits the time the arc has to heat the surrounding gas.

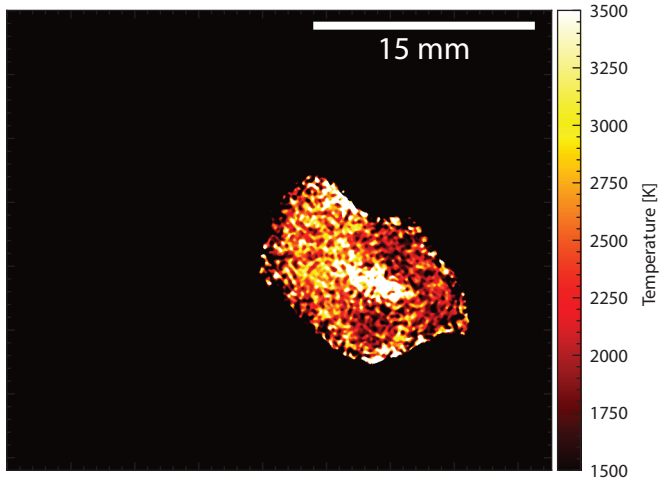

Figure 12.15: The fluorescence lifetime image depicted in Figure 12.12 (b) converted to temperature using the fluorescence lifetime model shown in Figure 12.14.

Combined Rayleigh Thermometry and OH LIF Imaging

Previous Rayleigh temperature measurements by Zhu et al. under similar flow conditions reported gas temperatures around 1100 K, which differ significantly from the values measured using fluorescence lifetime imaging [137]. However, Zhu et al. did not directly correlate the Rayleigh scattering signal with the arc's location or the OH signal from the arc, suggesting their temperature measurements may correspond to regions outside the arc. Moreover, Laser-Rayleigh thermometry can be challenging by strong background emissions from luminous objects, which may lead to underestimations in temperature.

Current fluorescence lifetime imaging data reveal higher temperatures within the core of the OH distribution, a region that Zhu et al. did not identify. This highlights the need for further investigation into local variations in fluorescence lifetimes and gas temperatures. As a result, a new experiment was designed, combining laser Rayleigh thermometry and laser fluorescence imaging to more accurately map gas temperatures in relation to OH fluorescence.

To minimize potential background interference, structured Rayleigh thermometry is employed, which has been shown to improve accuracy and signal quality [85]. A 532 nm laser was incorporated into the experimental setup (Figure 12.8), spatially aligned with the 283 nm laser used to excite OH. The 532 nm laser was temporally delayed by 20 ns to prevent interference with the OH measurements. Figure 12.16 presents a sample from the 10 l/min case. Both images were spatially aligned by recording a checkerboard pattern and using the Python cv2 package for sub-pixel precision.

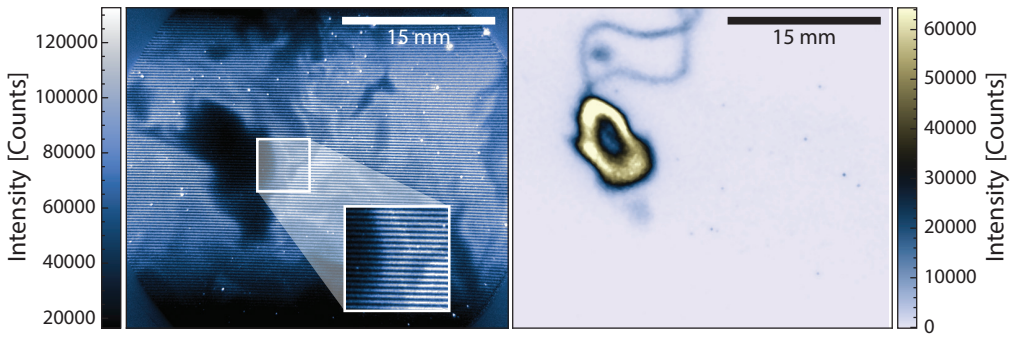

Figure 12.16: Panel (a) shows raw data from the structured Rayleigh scattering experiment, where darker regions correspond to higher temperatures. In panel (b), the OH fluorescence signal is displayed. The images are inversely related, indicating that the regions with OH presence correspond to elevated temperatures.

The Rayleigh data is converted to temperature by first applying Fourier filtering to the image in Figure 12.16(a), followed by the use of Equation (9.3), with the results displayed in Figure 12.17. The resulting temperature map and contours are superimposed on the OH data to illustrate the relationship between temperature gradients and the OH signal

in Figure 12.17(b). The data clearly demonstrates that the central region, where no OH signal is present, is significantly hotter than the OH-rich regions, supporting the findings from lifetime imaging, assuming that OH is in thermal equilibrium with the surrounding gas. Additionally, a small region at the bottom of Figure 12.17 (b) shows some OH signal, originating from an area where the arc has passed through, which is also reflected in the temperature map.

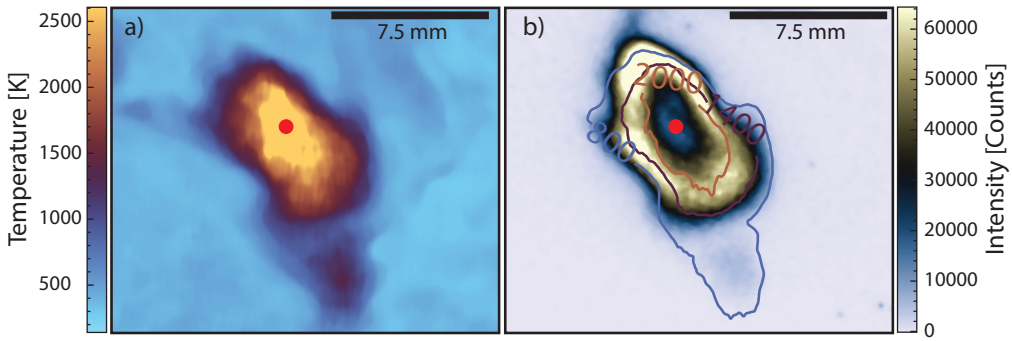

Figure 12.17: Panel (a) displays the temperature field around the OH structure derived from Figure 12.16. In panel (b), the OH fluorescence signal is displayed with temperature contours superimposed on the image.The red dots in both panels indicate the center of the OH signal.

Cross-sectional data along both horizontal and vertical directions are extracted from the temperature and OH signal in Figure 12.17 and is shown in Figure 12.18. It is evident that the temperature at the center of the OH hole reaches nearly 4000 K, which can also bee seen in Table 6. Additionally, as the OH signal decreases, the temperature increases, while at the edges of the OH signal, the temperature decreases, coinciding with a rise in gas temperature.

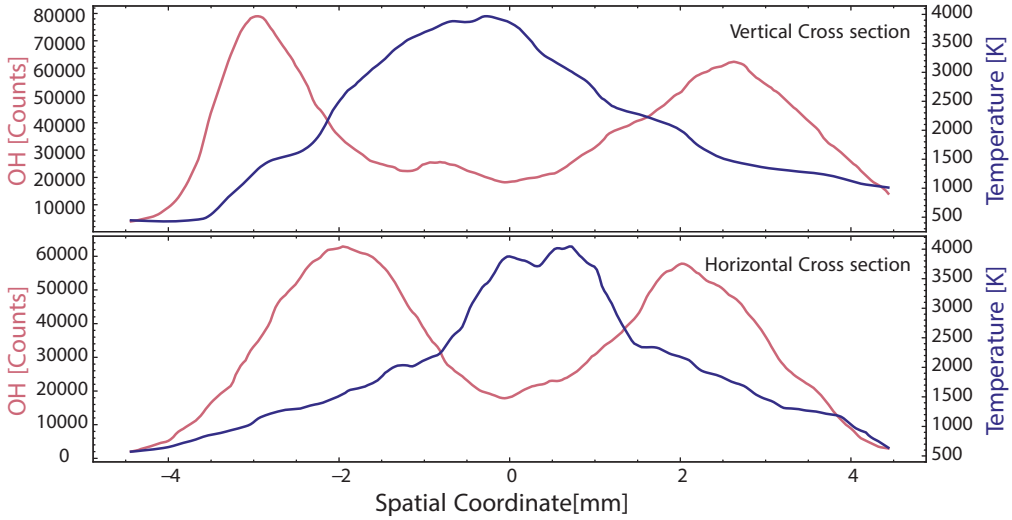

Figure 12.18: Cross-sectional data of the temperature and OH signal in both vertical and horizontal directions originating from the center of the red dots from Figure 12.17.

The data presented here exhibit similar trends to the temperatures derived from fluorescence lifetime imaging. However, these are preliminary results, and further analysis is required to increase confidence in these measurements, which will ultimately form the basis of a standalone publication.

12.3 Methyl Measurements in DBD Reactor

The formation of methyl radicals (CH_3) is crucial in plasma-assisted hydrocarbon chemistry, particularly during methane dehydrogenation. Accurate in situ imaging of CH_3 is essential for understanding various plasma processes [138, 139, 140]. Traditional detection methods, like infrared absorption spectroscopy, typically offer limited measurements [141, 142].

With growing interest in plasma-assisted technology, spatial and temporal imaging, such as planar laser-induced fluorescence (PLIF), becomes increasingly important [143, 144, 145, 132]. While direct detection of CH_3 via LIF is hindered by pre-dissociation, pump-probe methods like photofragmentation followed by LIF (PF-LIF) are effective alternatives [134, 146, 147].

To address challenges like overlapping background signals, techniques such as structured illumination modulate the PF beam to distinguish photofragments, with Fourier lock-in analysis used for signal extraction. Larsson et al. successfully applied this method to detect hydroperoxyl (HO_2) photofragmentation in a methane/air flame, as shown in Figure 7.1 [148].

As part of this thesis, structured illumination is combined with PF-PLIF to observe CH_3 dynamics in an atmospheric pressure DBD. A fifth harmonic Nd:YAG laser photofragments methyl into CH fragments, probed at 431.4 nm. Structured illumination helps differentiate natural from photofragmented CH and reduces interference from stray light, plasma emission, and the probe laser.

The optical setup involves the interaction of several laser beams within the probe volume. A picosecond Nd:YAG laser att 266 nm initiates the plasma discharge by illuminating the electrode, while a second nanosecond Nd:YAG laser operating at 212.8 nm provides pulses for photofragmentation of specific radicals. These lasers are synchronized to ensure proper timing of the discharge events. The photofragmentation laser beam passes through a Diffractive Optical Element (DOE) and is shaped into a sinusoidal modulation pattern as it enters the probe volume.

A third ps laser, operating at a 431.4 nm, probes the fragments produced during the photofragmentation process. The probe and photofragmentation beams are combined and focused to form laser sheets within the probe volume. Fluorescence signals are captured by two IsCMOS cameras, allowing for detailed imaging of the CH fluorescence.

Three different scenarios were studied: (1) The temporal dynamics of CH generated from the photofragmentation (PF) of CH_3 were investigated by varying the pump-probe delay (D_A) while keeping a fixed delay (D_B) between the ignition laser and the pump pulse. The goal was to identify the optimal delay time between plasma formation and the photolysis

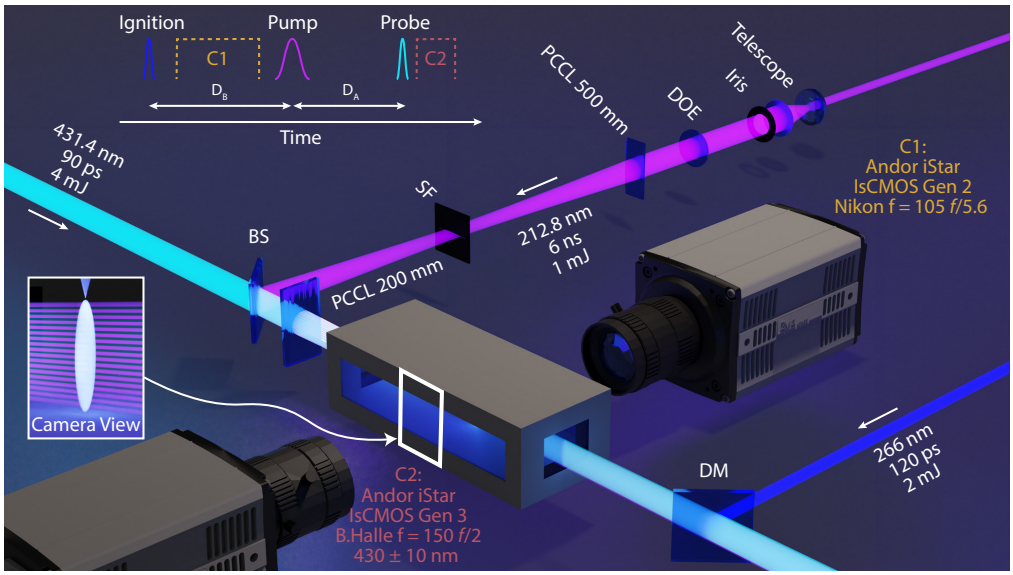

Figure 12.19: An overview of the experimental setup, PCCL: Planar Cylindrical Convex Lens, BS: Beam Splitter, DM: Dichroic Mirror, DOE: Diffractice Optical Element, SF: Spatial Filter.

pulse to maximize the signal from photolytically produced CH fragments and determine its decay rate. Next, (2) the temporal dynamics of CH_3 were examined by varying D_B while maintaining D_A constant, allowing for the investigation of the chemical lifetime of CH_3. Finally, (3) a typical case was analyzed, where the PF CH_3 signal reached its peak, capturing both the natural emission from the discharge and the laser-induced fluorescence from both naturally occurring CH and the photofragmented CH species derived from CH_3.

Figure 12.20 (e) compares the cross-sectional profiles of plasma-produced CH and CH from CH_3 radicals at three diffrent time delays after plasma initiation. The curves, normalized to unity, show that both species overlap spatially and have similar widths up to 220 ns post-discharge. The CH_3 FWHM is about 10% of the plasma-produced CH width, indicating CH forms a sheet around the CH_3-containing discharge channel. Spatio-temporal variations suggest different chemical reactions across the discharge channel, though further study is needed to fully understand these differences.

The temporal dynamics of CH photofragments, formed via photolysis, were studied around 150 ns after plasma generation (D_B) with varying D_A. As shown in Figure 12.21 (a), the optimal D_A for maximum signal intensity is 10-15 ns after discharge. The CH signal, from CH_3 photofragmentation, decays rapidly, falling below noise levels by 225 ns, indicating fast kinetics. This decay follows a mono-exponential pattern, suggesting a single dominant reaction with a lifetime of approximately 160 ns, likely involving CH reacting with CH_4 to form C_2H_4 and H (R.1), with other possible reactions including:

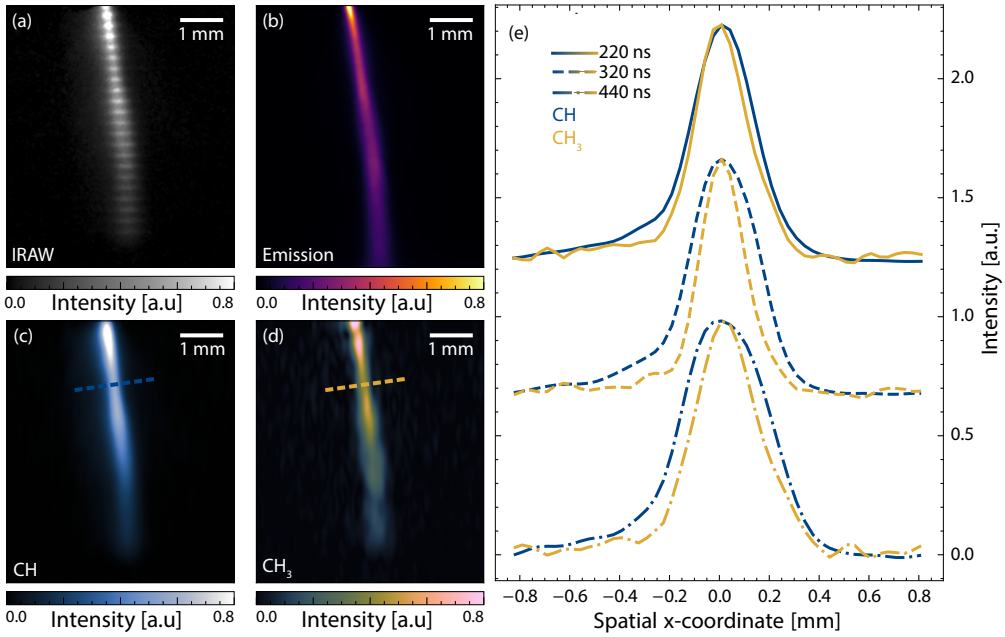

Figure 12.20: Typical data acquired with the temporal delays D_B = 150 ns and D_A = 10 ns. Panel (a) presents raw LIF data depicting both plasma produced CH and CH generated by UV photolysis of CH_3. This data is captured by camera C2. Panel (b) illustrates natural plasma emission captured by camera C1, while panel (c) showcases the Fourier-filtered plasma produced CH derived from panel (a). In panel (d), the Fourier-filtered signal from CH_3 derived from panel (a) is displayed. Lastly, panel (e) exhibits a cross-section of the plasma derived from the dashed lines in panels (c) and (d). Cross sectional data are shown for three delays after the discharge formation (D_B).

$$CH + CH_3 \rightarrow C_2H_3 + H \tag{R.1}$$

$$CH + CH_2 \rightarrow C_2H_2 + H \tag{R.2}$$

$$CH + H \rightarrow C + H_2 \tag{R.3}$$

The temporal dynamics of CH_3 consumption, with a 10 ns delay between photolysis and probe pulses (D_A), are shown in Figure 12.21 (b). The CH_3 signal rises slowly, peaking around 80 ns after discharge. CH_3 forms primarily from CH_4 dissociation via electron collisions or interactions with metastable Ar, and does not directly contribute to CH production, suggesting separate pathways for CH and CH_3 [141].

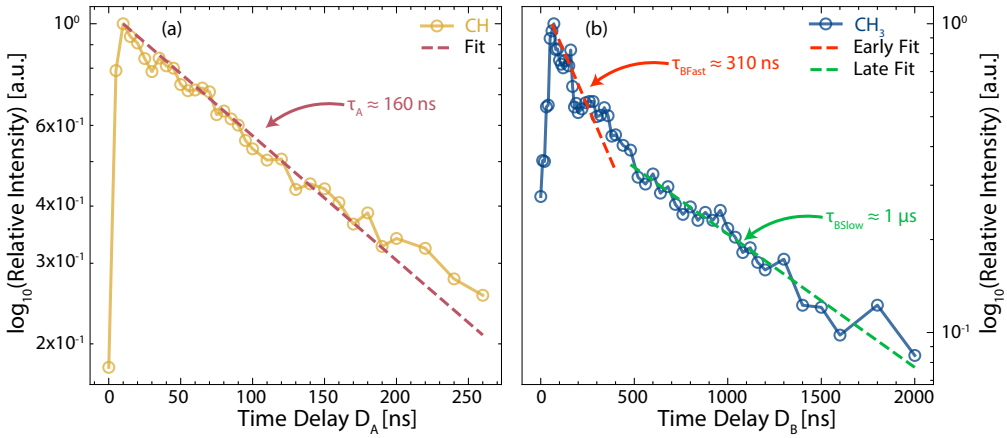

Figure 12.21: Panel (a) displays spatially averaged temporal dynamics of CH generated by the PF of CH_3, while panel (b) depicts the spatially averaged temporal dynamics of CH_3 generated by the plasma discharge. Each panel is accompanied by corresponding mono-exponential fits.

CH_3 has a longer chemical lifetime ($\sim$ 600 ns) than CH that is produced from photolysis, considerably shorter than what was observed by Van den Bekerom et al., although this was under different conditions (200 Torr, CO_2/CH_4 mixture) [149]. The CH_3 decay is multi-exponential, with a fast component ($\sim$ 310 ns) and a slower one ($\sim$ 1 μs), likely due to reactions forming CH_4, C_2H_6, and C_3H_8:

$$CH_3 + H + M \rightarrow CH_4 + M \tag{R.4}$$

$$CH_3 + CH_3 + M \rightarrow C_2H_6 + M \tag{R.5}$$

$$CH_3 + C_2H_5 + M \rightarrow C_3H_8 + M \tag{R.6}$$

These reactions likely explain the observed multi-exponential decay.

The data presented in this study offers valuable insights into the spatio-temporal behavior of the CH_3 radical. However, to fully understand the evolution of CH and CH_3 signals over time and to correlate their temporal and spatial dynamics in this context, it would be beneficial to combine these experimental measurements with plasma kinetic simulations.

Outlook

Now this is not the end.
It is not even the beginning of the end.
But it is, perhaps, the end of the beginning.
–Winston Churchill

The research presented in this thesis has significantly advanced the development of diagnostic techniques, specifically for high-temperature surface measurements and the investigation of plasma discharges. The results demonstrate the effectiveness and adaptability of both phosphor thermometry and laser-based optical diagnostics in extreme environments, ranging from hydrogen-powered gas turbines to highly dynamic plasma systems.

Looking ahead, the integration of advanced diagnostic techniques into real-world applications, such as plasma chemical processing and power generation is of great interest. Combining these methods with other diagnostic tools in multi-parameter measurement frameworks will be essential for correlating physical phenomena like temperature, molecular distribution, and system dynamics. This approach will further improve our understanding of complex systems, such as plasma-assisted combustion and non-thermal plasma reactors, where accurate, real-time diagnostics are critical for optimization and control.

The development of new high-temperature phosphors marks a significant advancement in surface temperature measurements beyond conventional limits. The novel phosphor YAG:Tm;Li, calibrated to nearly 2000 K while being coated on a surface, and having a SNR almost 10 times higher than the most commonly used phosphor for high temperature measurements, YAG:Dy, represents a breakthrough in this area. These phosphors provide robust, non-intrusive temperature monitoring at extreme temperatures, with promising applications in industries such as gas turbines and combustion systems. Future work can build on the methodologies introduced in this thesis, expanding their application range and refining their performance. For phosphor thermometry, research could focus on extending the temperature range and sensitivity of phosphors, targeting applications exceeding 2000 K, particularly in advanced propulsion and energy systems. Additionally, the development

of more accessible and scalable experimental setups for laser diagnostics could facilitate broader adoption in both research and industrial environments.

In plasma research, the laser diagnostic methods developed in this work have tackled key challenges associated with the stochastic and non-equilibrium nature of non-thermal plasmas. The innovative combination of fluorescence lifetime imaging (FLI) and 3D emission tomography has yielded new insights into plasma behavior, offering enhanced spatial and temporal diagnostics in highly reactive and dynamic environments. Expanding these techniques to more complex systems, such as plasma coupled with reactive flows where quenching conditions vary, would be particularly valuable. Moreover, the limited adoption of FLI in the broader research community underscores the need for more accessible and streamlined experimental setups. Developing such setups for FLI and 3D emission tomography would facilitate broader use, enabling quenching-corrected fluorescence imaging and, consequently, the acquisition of quantitative data.

A photofragmentation technique based on structured illumination has been developed to study methyl in plasma systems. Extending this method to more complex systems, such as plasma-assisted methane reforming in thermal plasmas, and combining it with FLI would be highly valuable. The photofragmentation of methyl would provide spatial information, while FLI would offer temperature and quenching data, enabling quenching-corrected imaging of methyl. This approach would require further development of the FLI model and the overall imaging system. Additionally, detecting multiple molecular species simultaneously would significantly enhance its applicability in combustion and chemical kinetics studies. Techniques like multiplexed excitation or the use of broadband laser sources could improve diagnostic efficiency, providing more comprehensive real-time data.

Ultimately, the advancements made in this thesis not only offer powerful tools for investigating high-temperature surface temperatures and plasma systems but also lay the foundation for future applications in energy production and sustainable technologies. As global energy demands continue to grow, the precise diagnostic techniques developed here will assist in creating cleaner, more efficient, and scalable solutions to meet the energy challenges of tomorrow.

References

[1] K. Kohse-Höinghaus. Laser techniques for the quantitative detection of reactive intermediates in combustion systems. *Progress in Energy and Combustion Science*, 20:203–279, 1991.

[2] Christopher Abram, B. Fond, and F. Beyrau. Temperature measurement techniques for gas and liquid flows using thermographic phosphor tracer particles. *Progress in Energy and Combustion Science*, 64:93–156, 2018.

[3] J. Gord, T. Meyer, and Sukesh Roy. Applications of ultrafast lasers for optical measurements in combusting flows. *Annual review of analytical chemistry*, 1:663–687, 2008.

[4] A. Ehn, Jiajian Zhu, Xuesong Li, and J. Kiefer. Advanced laser-based techniques for gas-phase diagnostics in combustion and aerospace engineering. *Applied Spectroscopy*, 71:341–366, 2017.

[5] Patrick Nau, Andre Müller, Niklas Petry, Sebastian Nilsson, Torsten Endres, Mattias Richter, and Benjamin Witzel. Fiber-coupled phosphor thermometry for wall temperature measurements in a full-scale hydrogen gas turbine combustor. *Measurement Science and Technology*, 34, 10 2023.

[6] M. Gentleman, V. Lughi, J. Nychka, and D. Clarke. Noncontact methods for measuring thermal barrier coating temperatures. *International Journal of Applied Ceramic Technology*, 3:105–112, 2006.

[7] D. White. Hot and cold: defining and measuring temperature. *Contemporary Physics*, 61:256–276, 2020.

[8] B. R. Reddy, I. Kamma, and P. Kommidi. Optical sensing techniques for temperature measurement. *Applied Optics*, 52 4:B33–B39, 2013.

[9] Ashiq Hussain Khalid and Konstantinos Kontis. Thermographic phosphors for high temperature measurements: Principles, current state of the art and recent applications. *Sensors*, 8:5673–5744, 9 2008.

[10] Marcus Aldén, Alaa Omrane, Mattias Richter, and Gustaf Särner. Thermographic phosphors for thermometry: A survey of combustion applications. *Progress in Energy and Combustion Science*, 37:422–461, 2011.

[11] Henrik Feuk, Sebastian Nilsson, and Mattias Richter. Temperature resolved decay time components of mg4fge06:mn using the maximum entropy method. *Review of Scientific Instruments*, 94, 3 2023.

[12] Sebastian Nilsson, Henrik Feuk, and Mattias Richter. High temperature thermographic phosphors yag:tm;li and yag:dy in reduced oxygen environments. *Journal of Luminescence*, 256, 4 2023.

[13] Sebastian Nilsson, Elias Kristensson, Marcus Aldén, Joakim Bood, and Andreas Ehn. Fluorescence lifetime imaging through scattering media. *Scientific Reports*, 13, 12 2023.

[14] Yupan Bao, Chengdong Kong, Jonas Ravelid, Jinguo Sun, Sebastian Nilsson, Elias Kristensson, and Andreas Ehn. Effect of a single nanosecond pulsed discharge on a flat methane–air flame. *Applications in Energy and Combustion Science*, 16, 12 2023.

[15] Jinguo Sun, Yupan Bao, Jonas Ravelid, Sebastian Nilsson, Alexander A. Konnov, and Andreas Ehn. Application of emission spectroscopy in plasma-assisted nh3/air combustion using nanosecond pulsed discharge. *Combustion and Flame*, 263, 5 2024.

[16] Jinguo Sun, Jonas Ravelid, Yupan Bao, Sebastian Nilsson, Alexander A. Konnov, and Andreas Ehn. Dynamics of atomic oxygen production in an nh3/air flame assisted by a nanosecond pulsed plasma discharge. *Proceedings of the Combustion Institute*, 40, 1 2024.

[17] A. Donné and C. J. Barth. Laser-aided plasma diagnostics. *Fusion Science and Technology*, 49:375–386, 2004.

[18] R. Mcwilliams and D. Edrich. Laser-induced fluorescence diagnosis of plasma processing sources. *Thin Solid Films*, 435:1–4, 2003.

[19] A. Donné and C. J. Barth. Laser-aided plasma diagnostics. *Fusion Science and Technology*, 53:398–408, 2008.

[20] Timothy Ombrello, Sang Hee Won, Yiguang Ju, and Skip Williams. Flame propagation enhancement by plasma excitation of oxygen. part ii: Effects of o2(a1Δg). *Combustion and Flame*, 157(10):1916–1928, 2010.

[21] S. Hübner, J. Sousa, J. van der Mullen, and W. Graham. Thomson scattering on non-thermal atmospheric pressure plasma jets. *Plasma Sources Science and Technology*, 24, 2017.

[22] E. Carbone and S. Nijdam. Thomson scattering on non-equilibrium low density plasmas: principles, practice and challenges. *Plasma Physics and Controlled Fusion*, 57, 2014.

[23] Andreas Ehn, Malin Jonsson, Olof Johansson, Marcus Aldén, and Joakim Bood. Quantitative oxygen concentration imaging in toluene atmospheres using dual imaging with modeling evaluation. *Experiments in Fluids*, 54:1–8, 1 2013.

[24] A. Ehn, O. Johansson, J. Bood, A. Arvidsson, B. Li, and M. Aldén. Fluorescence lifetime imaging in a flame. *Proceedings of the Combustion Institute*, 33:807–813, 2011.

[25] Sebastian Nilsson, Jonas Ravelid, Jin Park, Min Suk Cha, and Andreas Ehn. Photofragmentation laser-induced fluorescence imaging of ch 3 by structured illumination in a plasma discharge. *Optics Express*, 32:26492, 7 2024.

[26] Sebastian Nilsson, David Sanned, Adrian Roth, Jinguo Sun, Edouard Berrocal, Mattias Richter, and Andreas Ehn. Holistic analysis of a gliding arc discharge using 3d tomography and single-shot fluorescence lifetime imaging. *Communications Engineering*, 3, 12 2024.

[27] BH Bransden and CJ Joachain. *Physics of Atoms and Molecules*. Prentice Hall, 2nd edition, 2000.

[28] David J Griffiths. *Introduction to Quantum Mechanics*. Cambridge University Press, 3rd edition, 2017.

[29] Peter Atkins and Ronald Friedman. *Molecular Quantum Mechanics*. Oxford University Press, 5th edition, 2011.

[30] Donald A McQuarrie and John D Simon. *Physical Chemistry: A Molecular Approach*. University Science Books, 1997.

[31] Attila Szabo and Neil S Ostlund. *Modern Quantum Chemistry: Introduction to Advanced Electronic Structure Theory*. Dover Publications, 1996.

[32] Bahaa E A Saleh and Malvin Carl Teich. *Fundamentals of Photonics*. John Wiley & Sons, 3rd edition, 2019.

[33] Eugene Hecht. *Optics*. Pearson Education, Inc., 2016.

[34] Wolfgang Demtröder. *Laser Spectroscopy: Basic Concepts and Instrumentation*. Springer Science & Business Media, 4th edition, 2008.

[35] Peter W Milonni and Joseph H Eberly. *Laser Physics*. John Wiley & Sons, 2010.

[36] A.C. Eckbreth. *Laser Diagnostics for Combustion Temperature and Species*. CRC Press, 2022.

[37] Craig F. Bohren and Donald R. Huffman. *Absorption and Scattering of Light by Small Particles*. Wiley, 1983.

[38] Derek A Long. *The Raman Effect: A Unified Treatment of the Theory of Raman Scattering by Molecules*. John Wiley & Sons, 2002.

[39] John R. Ferraro, Kazuo Nakamoto, and Chris W. Brown. *Introductory Raman Spectroscopy*. Academic Press, 2nd edition, 2003.

[40] Joseph R Lakowicz. *Principles of Fluorescence Spectroscopy*. Springer, 3rd edition, 2006.

[41] Wolfgang Demtröder. *Molecular Physics: Theoretical Principles and Experimental Methods*. Wiley-VCH, 2003.

[42] Nicholas J. Turro, V. Ramamurthy, and J. C. Scaiano. *Principles of Molecular Photochemistry: An Introduction*. University Science Books, 2010.

[43] John B. Birks. *Photophysics of Aromatic Molecules*. Wiley-Interscience, 1970.

[44] Wolfgang Demtröder. *Atoms, Molecules and Photons: An Introduction to Atomic-Molecular- and Quantum Physics*. Springer, 2nd edition, 2015.

[45] Robert W Boyd. *Nonlinear Optics*. Academic Press, 4th edition, 2020.

[46] Y. R. Shen. *The Principles of Nonlinear Optics*. Wiley-Interscience, 1984.

[47] Philip N. Butcher and David Cotter. *The Elements of Nonlinear Optics*. Cambridge University Press, 1991.

[48] Govind P. Agrawal. *Nonlinear Fiber Optics*. Academic Press, 6th edition, 2019.

[49] Hermann Haken and Hans Christoph Wolf. *The Physics of Atoms and Quanta: Introduction to Experiments and Theory*. Springer, 7th edition, 2005.

[50] Hans R. Griem. *Principles of Plasma Spectroscopy*. Cambridge University Press, 1997.

[51] Francis F. Chen. *Introduction to Plasma Physics and Controlled Fusion*. Springer, 3rd edition, 2016.

[52] Alexander Fridman. *Plasma Chemistry*. Cambridge University Press, 2008.

[53] T.J.M. Boyd and J.J. Sanderson. *The Physics of Plasmas*. Cambridge University Press, 2003.

[54] Nicholas A. Krall and Alvin W. Trivelpiece. *Principles of Plasma Physics*. McGraw-Hill, 1973.

[55] Paul M. Bellan. *Fundamentals of Plasma Physics*. Cambridge University Press, 2006.

[56] Peter A. Sturrock. *Plasma Physics: An Introduction to the Theory of Astrophysical, Geophysical and Laboratory Plasmas*. Cambridge University Press, 1994.

[57] Yu P. Raizer. *Gas Discharge Physics*. Springer, 2019.

[58] A. E. D. Heylen. Sparking formulae for very high-voltage paschen characteristics of gases. *IEEE Electrical Insulation Magazine*, 22:25–35, 2006.

[59] Michael A. Lieberman and Allan J. Lichtenberg. *Principles of Plasma Discharges and Materials Processing*. Wiley-Interscience, 2005.

[60] Johnston T.W. Shkarofsky, I.P. and M.P. Bachynski. *The Particle Kinetics of Plasmas*. Addison-Wesley, 1966.

[61] Orazio Svelto. *Principles of Lasers*. Springer, 2010.

[62] Peter W. Milonni and Joseph H. Eberly. *Laser Physics*. Wiley, 2010.

[63] Glenn F. Knoll. *Radiation Detection and Measurement*. John Wiley & Sons, 2010.

[64] Philip C.D. Hobbs. *Building Electro-Optical Systems: Making It All Work*. John Wiley & Sons, 2009.

[65] Martin P. Slater and Nicholas H. Slater. *Electronics and Communications for Scientists*. Cambridge University Press, 2009.

[66] Photomultiplier tube - Wikipedia — en.wikipedia.org. `https://en.wikipedia.org/wiki/Photomultiplier_tube#/media/File:PhotoMultiplierTubeAndScintillator.svg`. [Accessed 20-09-2024].

[67] MD Dramićanin. Trends in luminescence thermometry. *Journal of Applied Physics*, 2020.

[68] T Yokomori N Ishiwada, K Tsuchiya. Applicability of dy-doped yttrium aluminum garnet (yag: Dy) in phosphor thermometry at different oxygen concentrations. *Journal of Luminescence*, 2019.

[69] Y Mao F Jahanbazi. Recent advances on metal oxide-based luminescence thermometry. *Journal of Materials Chemistry C*, 2021.

[70] K Kontis AH Khalid. Progress towards absolute intensity measurements of emissions from high temperature thermographic phosphors. *Journal of Luminescence*, 2011.

[71] Frank Beyrau, Benoît Fond, and Christopher Abram. A summary of new developments in phosphor thermometry. *Measurement Science and Technology*, 32(12):120101, oct 2021.

[72] SF León-Luis JL Rodríguez C Pérez-Rodríguez, LL Martín. Relevance of radiative transfer processes on nd3+ doped phosphate glasses for temperature sensing by means of the fluorescence intensity ratio technique. *Sensors and Actuators B*, 2014.

[73] Y Zheng Z Zhang W Cao Y Zhou, F Qin. Fluorescence intensity ratio method for temperature sensing. *Optics letters*, 2015.

[74] GW Baxter SA Wade, SF Collins. Fluorescence intensity ratio technique for optical fiber point temperature sensing. *Journal of Applied physics*, 2003.

[75] Stephen W. Allison and George T. Gillies. Review of thermographic phosphors for gas turbine engines. *Applied Optics*, 36(13):3379–3393, 1997.

[76] M Richter H Feuk, S Nilsson. Temperature resolved decay time components of mg4fgeo6: Mn using the maximum entropy method. *Review of Scientific Instruments*, 2023.

[77] M Kim J Jung H Shin KC Kim T Cai, J Han. Adaptive window technique for lifetime-based temperature and velocity simultaneous measurement using thermographic particle tracking velocimetry with a single .... *Experiments in Fluids*, 2022.

[78] N. Fuhrmann, J. Brübach, and A. Dreizler. On the mono-exponential fitting of phosphorescence decays. *Applied Physics B: Lasers and Optics*, 116:359–369, 2014.

[79] M Richter G Särner M Aldén, A Omrane. Thermographic phosphors for thermometry: a survey of combustion applications. *Progress in energy and combustion science*, 2011.

[80] Y Lai C Jiang J Liu F Vetrone X Liu, A Skripka. Fast wide-field upconversion luminescence lifetime thermometry enabled by single-shot compressed ultrahigh-speed imaging. *Nature Communications*, 2021.

[81] A Dreizler N Fuhrmann, J Brübach. Phosphor thermometry: A comparison of the luminescence lifetime and the intensity ratio approach. *Proceedings of the Combustion Institute*, 2013.

[82] Henrik Feuk. *Lifetime Surface Phosphor Thermometry - Technique Developments, Sources of Error, and Applications*. Doctoral thesis (compilation), Faculty of Engineering, LTH, March 2023. Defence details Date: 2023-04-14 Time: 09:15 Place: Lecture Hall Rydbergsalen, Department of Physics, Professorsgatan 1, Faculty of Engineering LTH, Lund University, Lund. External reviewer(s) Name: Petersen, Brian Title: Senior Lect. Affiliation: University of Edinburgh, United Kingdom.

[83] Edouard Berrocal, Elias Kristensson, Mattias Richter, Mark Linne, and Marcus Aldén. Application of structured illumination for multiple scattering suppression in planar laser imaging of dense sprays. *Optics Express*, 16(22):17870, oct 2008.

[84] Tobias Breuninger, Klaus Greger, and Ernst H. K. Stelzer. Lateral modulation boosts image quality in single plane illumination fluorescence microscopy. *Optics Letters*, 32(13):1938, jul 2007.

[85] Elias Kristensson, Andreas Ehn, Joakim Bood, and Marcus Aldén. Advancements in rayleigh scattering thermometry by means of structured illumination. *Proceedings of the Combustion Institute*, 35(3):3689–3696, 2015.

[86] Vassily Kornienko. *Structured Light for Ultrafast Videography*. Doctoral thesis (compilation), Faculty of Engineering, LTH, 2024. Defence details Date: 2024-04-12 Time: 09:15 Place: Lecture Hall Rydbergsalen, Department of Physics, Professorsgatan 1, Faculty of Engineering LTH, Lund University, Lund. The dissertation will be live streamed, but part of the premises is to be excluded from the live stream. External reviewer(s) Name: Richardson, Daniel R. Title: Prof. Affiliation: Sandia National Laboratories, USA.

[87] Klaus Suhling, Liisa M. Hirvonen, James A. Levitt, Pei Hua Chung, Carolyn Tregidgo, Alix Le Marois, Dmitri A. Rusakov, Kaiyu Zheng, Simon Ameer-Beg, Simon Poland, Simao Coelho, Robert Henderson, and Nikola Krstajic. Fluorescence lifetime imaging (FLIM): Basic concepts and some recent developments. *Medical Photonics*, 27:3–40, may 2015.

[88] Wolfgang Becker. *Advanced Time-Correlated Single Photon Counting Techniques*. Springer, 2012.

[89] Wolfgang Becker. *Fluorescence Lifetime Imaging—Techniques and Applications*. Springer, 2005.

[90] Yahui Li, Lixin Liu, Dong Xiao, Hang Li, Natakorn Sapermsap, Jinshou Tian, Yu Chen, and David Day-Uei Li. Lifetime determination algorithms for time-domain fluorescence lifetime imaging: A review. In Raffaello Papadakis, editor, *Fluorescence Imaging*, chapter 5. IntechOpen, Rijeka, 2022.

[91] Sing Po Chan, Z. J. Fuller, J. N. Demas, and B. A. DeGraff. Optimized gating scheme for rapid lifetime determinations of single-exponential luminescence lifetimes. *Analytical Chemistry*, 73(18):4486–4490, 2001. PMID: 11575797.

[92] Andreas Ehn, Olof Johansson, Andreas Arvidsson, Marcus Aldén, and Joakim Bood. Single-laser shot fluorescence lifetime imaging on the nanosecond timescale using a dual image and modeling evaluation algorithm. *Opt. Express*, 20(3):3043–3056, Jan 2012.

[93] J Sutton and J Driscoll. Rayleigh scattering cross sections of combustion species at 266, 355, and 532 nm for thermometry applications. *Optics Letters*, 29(22):2620–2622, 2004.

[94] A Mielke, KA Elam, and C Sung. Rayleigh scattering diagnostic for measurement of temperature, velocity, and density fluctuation spectra. *AIAA Journal*, 47(10):850–862, 2006.

[95] N Kempema and M Long. Quantitative rayleigh thermometry for high background scattering applications with structured laser illumination planar imaging. *Applied Optics*, 53(29):6688–6697, 2014.

[96] D Müller, R Pagel, A Burkert, V Wagner, and W Paa. Two-dimensional temperature measurements in particle loaded technical flames by filtered rayleigh scattering. *Applied Optics*, 53(9):1750–1758, 2014.

[97] E Kristensson, A Ehn, J Bood, and M Aldén. Advancements in rayleigh scattering thermometry by means of structured illumination. *Proceedings of the Combustion Institute*, 35(3):3689–3696, 2015.

[98] Jinpeng Pu and J Sutton. Quantitative 2d thermometry in turbulent sooting non-premixed flames using filtered rayleigh scattering. *Applied Optics*, 60(19):5742–5751, 2021.

[99] David Sanned, Johan Lindström, Adrian Roth, Marcus Aldén, and Mattias Richter. Arbitrary position 3D tomography for practical application in combustion diagnostics. *Measurement Science and Technology*, 33(12), 2022.

[100] Kyle J. Daun, Samuel J. Grauer, and Paul J. Hadwin. Chemical species tomography of turbulent flows: Discrete ill-posed and rank deficient problems and the use of prior information. *Journal of Quantitative Spectroscopy and Radiative Transfer*, 172:58–74, mar 2016.

[101] Roger Y. Tsai. A Versatile Camera Calibration Technique for High-Accuracy 3D Machine Vision Metrology Using Off-the-Shelf TV Cameras and Lenses. *IEEE Journal on Robotics and Automation*, 3(4):323–344, 1987.

[102] SA Hashemi Jazi. *A Contactless Solid Surface Temperature Determination Using Phosphor Thermometry*. PhD thesis, 2021.

[103] Henrik Feuk, Sebastian Nilsson, Marcus Aldén, and Mattias Richter. Investigating photomultiplier tube nonlinearities in high-speed phosphor thermometry using light emitting diode simulated decay curves. *Review of Scientific Instruments*, 92, 12 2021.

[104] C. Abram, B. Fond, and F. Beyrau. Temperature measurement techniques for gas and liquid flows using thermographic phosphor tracer particles. *Progress in Energy and Combustion Science*, 2018.

[105] DR Clarke MD Chambers. Doped oxides for high-temperature luminescence and lifetime thermometry. *Annual Review of Materials Science*, 2009.

[106] S. Nilsson, H. Feuk, and M. Richter. High temperature thermographic phosphors yag: Tm; li and yag: Dy in reduced oxygen environments. *Journal of Luminescence*, 2023.

[107] C. Binder, H. Feuk, and M. Richter. Phosphor thermometry for in-cylinder surface temperature measurements in diesel engines. *Journal of Luminescence*, 2020.

[108] R. A. Hansel. *Phosphor thermometry using rare-earth doped materials*. PhD thesis, 2010.

[109] L. M. Chepyga, G. Jovicic, A. Vetter, A. Osvet, and C. J. Brabec. Photoluminescence properties of thermographic phosphors yag: Dy and yag: Dy, er doped with boron and nitrogen. *Applied Physics B*, 2016.

[110] L. M. Chepyga, A. Osvet, and C. J. Brabec. High-temperature thermographic phosphor mixture yap/yag: Dy3+ and its photoluminescence properties. *Journal of Luminescence*, 2017.

[111] Daniel Avram, Bogdan Cojocaru, Ion Tiseanu, Mihaela Florea, and Carmen Tiseanu. Down-/up-conversion emission enhancement by li addition: Improved crystallization or local structure distortion? *Journal of Physical Chemistry C*, 121:14274–14284, 7 2017.

[112] Daniel Avram, Ion Tiseanu, Bogdan S. Vasile, Mihaela Florea, and Carmen Tiseanu. Near infrared emission properties of er doped cubic sesquioxides in the second/third biological windows. *Scientific Reports*, 8, 12 2018.

[113] Ellen Hertle, Liudmyla Chepyga, Miroslaw Batentschuk, Stefan Will, and Lars Zigan. Temperature-dependent luminescence characteristics of dy3+ doped in various crystalline hosts. *Journal of Luminescence*, 204:64–74, 2018.

[114] S. W. Allison, D. L. Beshears, M. R. Cates, M. B. Scudiere, D. W. Shaw, and A. D. Ellis. Luminescence of yag:dy and yag:dy,er crystals to 1700 °c. *Measurement Science and Technology*, 31, 2020.

[115] Ellen Hertle, Liudmyla Chepyga, Miroslaw Batentschuk, and Lars Zigan. Influence of codoping on the luminescence properties of yag:dy for high temperature phosphor thermometry. *Journal of Luminescence*, 182:200–207, 2 2017.

[116] Jeffrey I. Eldridge, Stephen W. Allison, Thomas P. Jenkins, Sarah L. Gollub, Carl A. Hall, and D. Greg Walker. Surface temperature measurements from a stator vane doublet in a turbine afterburner flame using a yag:tm thermographic phosphor. *Measurement Science and Technology*, 27, 11 2016.

[117] Henrik Feuk, Sebastian Nilsson, and Mattias Richter. Automated phosphor thermometry lifetime calibration of multiple phosphors and emission lines to above 1900 k. *Measurement Science and Technology*, 33, 12 2022.

[118] Naohiro Ishiwada, Kazuki Tsuchiya, and Takeshi Yokomori. Applicability of dy-doped yttrium aluminum garnet (yag:dy) in phosphor thermometry at different oxygen concentrations. *Journal of Luminescence*, 208:82–88, 4 2019.

[119] T Cai, D Li, J Jung, M Kim, CH Jeon, and KC Kim. Two-dimensional visualization of oxygen concentration field at high-temperature environment using phosphor y203: Eu3+. *Sensors and Actuators B: Chemical*, 2022.

[120] Rosario Esposito, Carlo Altucci, and Raffaele Velotta. Analysis of simulated fluorescence intensities decays by a new maximum entropy method algorithm. *Journal of Fluorescence*, 23(1):203–211, October 2012.

[121] Rosario Esposito, Giuseppe Mensitieri, and Sergio de Nicola. Improved maximum entropy method for the analysis of fluorescence spectroscopy data: evaluating zero-time shift and assessing its effect on the determination of fluorescence lifetimes. *Analyst*, 140:8138–8147, 2015.

[122] N. Fuhrmann, J. Brübach, and A. Dreizler. Spectral decomposition of phosphorescence decays. *Review of Scientific Instruments*, 84(11):114902, 11 2013.

[123] Tânia M. Ribeiro, Tiago E.C. Magalhães, Bohdan Kulyk, Alexandre F. Carvalho, Sebastian Nilsson, Henrik Feuk, António J.S. Fernandes, Florinda Costa, Paulo T. Guerreiro, and Helder Crespo. Observation of thickness-independent ultrafast relaxation times in mpcvd few-layer graphene. *Carbon*, page 119700, 2024.

[124] Henrik Feuk, Sebastian Nilsson, and Mattias Richter. Upconversion phosphor thermometry for use in thermal barrier coatings. *Measurement Science and Technology*, 34(6):064003, mar 2023.

[125] P Bruggeman and R Brandenburg. Atmospheric pressure discharge filaments and microplasmas: physics, chemistry and diagnostics. *Journal of Physics D: Applied Physics*, 2013.

[126] J Zhu, Y Kusano, and Z Li. Optical diagnostics of a gliding arc discharge at atmospheric pressure. *Atmospheric pressure plasmas*, 2016.

[127] S Heijkers V Hessel W Wang, B Patil. Nitrogen fixation by gliding arc plasma: better insight by chemical kinetics modelling. *ChemSusChem*, 2017.

[128] S Yao B Wang, Y Peng. Oxidative reforming of n-heptane in gliding arc plasma reformer for hydrogen production. *International Journal of Hydrogen Energy*, 2019.

[129] X Li L Han M Yan Y Zhong H Zhang, W Wang. Plasma activation of methane for hydrogen production in a n2 rotating gliding arc warm plasma: a chemical kinetics study. *Chemical Engineering Journal*, 2018.

[130] Yupan Bao, Karolina Dorozynska, P. Stamatoglou, Chengdong Kong, T. Hurtig, S. Pfaff, J. Zetterberg, M. Richter, E. Kristensson, and A. Ehn. Single-shot 3d imaging of hydroxyl radicals in the vicinity of a gliding arc discharge. *Plasma Sources Science and Technology*, 30, 2021.

[131] Jiajian Zhu, Zhiwei Sun, Zhongshan Li, Andreas Ehn, Marcus Aldén, Mirko Salewski, Frank Leipold, and Yukihiro Kusano. Dynamics, OH distributions and UV emission of a gliding arc at various flow-rates investigated by optical measurements. *Journal of Physics D: Applied Physics*, 47(29), jul 2014.

[132] Z. Wang, P. Stamatoglou, C. Kong, J. Gao, Y. Bao, M. Aldén, A. Ehn, and M. Richter. Hydroxyl radical dynamics in a gliding arc discharge using high-speed PLIF imaging. *Plasma Research Express*, 4(2), jun 2022.

[133] Z. Yin, Z. Eckert, I. V. Adamovich, and W. R. Lempert. Time-resolved radical species and temperature distributions in an Ar-O2-H2 mixture excited by a nanosecond pulse discharge. *Proceedings of the Combustion Institute*, 35(3):3455–3462, 2015.

[134] O. Johansson, J. Bood, B. Li, A. Ehn, Z. S. Li, Z. W. Sun, M. Jonsson, A. A. Konnov, and M. Aldén. Photofragmentation laser-induced fluorescence imaging in premixed flames. *Combustion and Flame*, 158(10):1908–1919, 2011.

[135] Dwayne E. Heard and David A. Henderson. Quenching of OH (A 2Σ+, ν' = 0) by several collision partners between 200 and 344 K. Cross-section measurements and model comparisons. *Physical Chemistry Chemical Physics*, 2(1):67–72, jan 2000.

[136] Mahdi Yousefi, Peter F. Bernath, James Hodges, and Thomas Masseron. A new line list for the A2Σ+–X2Π electronic transition of OH. *Journal of Quantitative Spectroscopy and Radiative Transfer*, 217:416–424, sep 2018.

[137] Jiajian Zhu, Andreas Ehn, Jinlong Gao, Chengdong Kong, Marcus Aldén, Mirko Salewski, Frank Leipold, Yukihiro Kusano, and Zhongshan Li. Translational, rotational, vibrational and electron temperatures of a gliding arc discharge. *Optics Express*, 25(17):20243, aug 2017.

[138] Stijn Heijkers, Maryam Aghaei, and Annemie Bogaerts. Plasma-Based CH_4 Conversion into Higher Hydrocarbons and H_2: Modeling to Reveal the Reaction Mechanisms of Different Plasma Sources. *Journal of Physical Chemistry C*, 124(13):7016–7030, apr 2020.

[139] Jiayu Feng, Xin Sun, Zhao Li, Xingguang Hao, Maohong Fan, Ping Ning, and Kai Li. Plasma-Assisted Reforming of Methane. *Advanced Science*, 9(34), dec 2022.

[140] Dae Hoon Lee, Kwan Tae Kim, Young Hoon Song, Woo Suk Kang, and Sungkwon Jo. Mapping plasma chemistry in hydrocarbon fuel processing processes. *Plasma Chemistry and Plasma Processing*, 33(1):249–269, feb 2013.

[141] Weizong Wang, Ramses Snoeckx, Xuming Zhang, Min Suk Cha, and Annemie Bogaerts. Modeling Plasma-based CO_2 and CH_4 Conversion in Mixtures with N_2, O_2, and H_2O: The Bigger Plasma Chemistry Picture. *Journal of Physical Chemistry C*, 122(16):8704–8723, apr 2018.

[142] Maynard J. Kong, Szetsen S. Lee, Julia Lyubovitsky, and Stacey F. Bent. Infrared spectroscopy of methyl groups on silicon. *Chemical Physics Letters*, 263(1-2):1–7, dec 1996.

[143] Aaron W. Skiba, Timothy M. Wabel, Campbell D. Carter, Stephen D. Hammack, Jacob E. Temme, Tonghun Lee, and James F. Driscoll. Reaction layer visualization: A comparison of two PLIF techniques and advantages of kHz-imaging. *Proceedings of the Combustion Institute*, 36(3):4593–4601, 2017.

[144] Mirosław Kwaśny and Aneta Bombalska. Applications of Laser-Induced Fluorescence in Medicine. *Sensors*, 22(8), apr 2022.

[145] D. C.M. Van Den Bekerom, E. R. Jans, and I. V. Adamovich. NO PLIF flow visualization and time-resolved temperature distributions in laser induced breakdown plumes. *Journal of Physics D: Applied Physics*, 54(26), jul 2021.

[146] Wubin Weng, Christian Brackmann, Marcus Aldén, and Zhongshan Li. Planar laser-induced photofragmentation fluorescence for quantitative ammonia imaging in combustion environments. *Combustion and Flame*, 235, jan 2022.

[147] Emil Thorin and Florian M. Schmidt. TDLAS-based photofragmentation spectroscopy for detection of K and KOH in flames under optically thick conditions. *Optics Letters*, 45(18):5230, sep 2020.

[148] Kajsa Larsson, Malin Jonsson, Jesper Borggren, Elias Kristensson, Andreas Ehn, Marcus Aldén, and Joakim Bood. Single-shot photofragment imaging by structured illumination. *Optics Letters*, 40(21):5019, nov 2015.

[149] Dirk van den Bekerom, Caleb Richards, Erxiong Huang, Igor Adamovich, and Jonathan H. Frank. 2D imaging of absolute methyl concentrations in nanosecond pulsed plasma by photo-fragmentation laser-induced fluorescence. *Plasma Sources Science and Technology*, 31(9), sep 2022.

Scientific publications

Author contributions

Paper I: Investigating photomultiplier tube nonlinearities in high-speed phosphor thermometry using light emitting diode simulated decay curves

Phosphor thermometry, which relies on temperature-sensitive luminescence decay times, is often affected by two key PMT nonlinearities: photocathode bleaching and space charge accumulation. These can distort decay time readings, leading to temperature errors.

Using LEDs to simulate decay curves, the study isolates PMT behavior under various gain settings and radiant flux levels. It shows that higher repetition rates and low PMT gain settings increase nonlinearity, especially due to photocathode bleaching. Space charge accumulation also worsens nonlinearities at high gain. It was found that operating PMTs at the highest radiant flux level where the response remains linear, ensuring the anode current stays within recommended limits.

Additionally, it was found that effects of background radiant flux on decay time accuracy, though a gated PMT can reduce these errors at lower repetition rates. Overall, this work provides guidelines for improving accuracy and precision in high-speed phosphor thermometry by optimizing PMT settings, especially in kHz-range experiments.

HF conducted the experimental work, performed the formal analysis, created the figures, and wrote the manuscript, while I had an supportive role throughout the process.

Paper II: Automated phosphor thermometry lifetime calibration of multiple phosphors and emission lines to above 1900 K

An automated system to perform lifetime calibration for temperatures exceeding 1900 K was developed. This method enables simultaneous calibration of several phosphors un-

der identical conditions, improving efficiency and data consistency, especially in high-temperature environments like gas turbines.

The experimental setup uses a Nd:YAG laser to excite the phosphors, which are applied to an alumina oxide disc. The system automates the data collection, ensuring real-time calibration without manual input. The calibration process is performed on four phosphors (YAG:Dy, YAG:Dy,Ce, BSAS:Tb, and $Y_2Si_2O_7$:Dy), and the algorithm analyzes different emission lines in a randomized sequence to avoid systematic errors.

The system's reliability and efficiency significantly reduce the time required for calibration, making it suitable for high-temperature applications where multiple phosphors need to be evaluated simultaneously under the same conditions.

HF and I jointly initiated the study and collaborated on the experimental work. HF was responsible for data evaluation and visualization, while I created the experimental setup figure. HF also developed the algorithm for automating data collection and wrote the manuscript. I had supportive role throughout the review process.

Paper III: Laser excitation effects in lifetime-based high-speed phosphor thermometry

This study examines how laser fluence and irradiance influence the decay time of phosphors, which is crucial for temperature calculations. It was found that MFG's decay time responds linearly to laser irradiance, while YVO_4:Tm is more sensitive to laser fluence. This challenges the assumption that laser-induced heating is the main source of error; instead, the study identifies photophysical effects in the phosphor materials as the primary cause of decay time changes. These effects shift the balance between shorter and longer decay time components as laser fluence increases. It is suggested that optimizing laser settings, minimizing fluence and irradiance while maintaining signal strength, can reduce errors in high-speed phosphor thermometry.

HF initiated the study and collaborated with me on the experimental work. HF was responsible for all data analysis and figure creation, as well as writing the manuscript. I had supportive role throughout the review process.

Paper IV: Fluorescence lifetime imaging through scattering media

Fluorescence lifetime determination is vital tool for quenching corrected fluorescence imaging but it becomes difficult when mixed signals from scattering affect the results. This study address this issue by combining structured illumination with spatial lock-in analysis to suppress the scattering and improve image contrast. The method is based on Dual Ima-

ging Modelling Evaluation (DIME), which enhances fluorescence lifetime measurements by separating the true fluorescence signal from scattered light. This allows for accurate lifetime imaging, even in harsh environments with significant scattering.

The experimental setup involves using a picosecond mode-locked laser and an imaging system that captures two images (short and long gated) of a toluene-seeded gas jet. Structured illumination creates a modulation pattern in the fluorescence signal, which is processed with spatial lock-in analysis to remove scattering artifacts. The results show that this approach can effectively recover accurate lifetime distributions, even in the presence of significant light scattering.

AE and EK conducted the experiments. I performed the data analysis, curated the figures, and wrote the majority of the manuscript, with assistance from AE and EK.

Paper V: Temperature resolved decay time components of Mg_4FGeO_6: Mn using the maximum entropy method

Maximum Entropy Method (MEM) allows for precise separation of multiple decay components from a single phosphor decay curve, outperforming traditional fitting methods that often assume a limited number of components.

In this study, two key decay components were identified. The longer component showed high sensitivity to temperature, making it useful for thermometry. By tracking the peaks in decay time distributions, MEM enables accurate temperature measurements, even in the presence of multi-exponential decay behavior. Techniques like optical filtering and dynamic down-sampling were used to minimize interference and capture both short and long decay times. MEM proved effective in resolving luminescence from both the phosphor and background sources, even in challenging environments.

I and HF jointly initiated the study and collaborated on the experimental work. HF developed the algorithm for data collection, performed the data analysis and visualization, and created all the figures. I authored the section on the Maximum Entropy Method, while HF wrote the remainder of the manuscript. I had supportive role throughout the review process.

Paper VI: Upconversion phosphor thermometry for use in thermal barrier coatings

The phosphors YSZ:Er,Yb and YSZ:Ho,Yb were characterized using both upconversion and downconversion luminescence. A Kubelka-Munk simulation compared their signal strength with YSZ:Er. Upconversion lifetime phosphor thermometry proved promising for

temperature measurements in a phosphor-doped YSZ layer due to its enhanced temperature sensitivity, reduced background interference, and strong signal strength.

HF initiated the study, performed the experimental work, analysis, figures and wrote the manuscript. I had a supportive role throughout.

Paper VII: High temperature thermographic phosphors YAG: Tm; Li and YAG: Dy in reduced oxygen environments

This study examines the performance of YAG:Tm;Li and YAG:Dy phosphors for high-temperature surface thermometry in low oxygen conditions. YAG:Tm;Li outperformed YAG:Dy, showing nearly ten times stronger signal strength and better signal-to-noise ratio, resulting in more accurate temperature measurements.

YAG:Tm;Li also exhibited lower sensitivity to oxygen concentration changes, minimizing errors due to oxygen quenching, particularly when using a mono-exponential decay fit. This makes it a better choice for high-temperature measurements in reduced oxygen environments, offering higher precision and reliability compared to YAG:Dy.

I initiated the study and collaborated with HF on the experimental work. I carried out most of the data analysis, with the exception of the Maximum Entropy Method, which was handled by HF. I authored the manuscript and was responsible for all the visualizations and figures.

Paper VIII: Fiber-coupled phosphor thermometry for wall temperature measurements in a full-scale hydrogen gas turbine combustor

Wall temperatures in a full-scale gas turbine combustor were measured using fiber-coupled phosphor thermometry with natural gas and up to 100% hydrogen. YAG:Dy and YAG:Tm;Li phosphors were tested, but YAG:Tm;Li was incompatible with the setup due to laser-induced interference. A strategy was developed to compensate for flame emission interferences during natural gas operation, enabling single-shot temperature measurements at 15 Hz with a precision of 2–7 K for a 1-second average.

PN, AM, and NP conducted the measurements at Siemens' test facility in Ludwigsfelde, near Berlin. Unfortunately, I was unable to participate in the experimental campaign due to unforeseen circumstances related to COVID-19. However, I provided the phosphors used in the measurements and authored the section of the paper on phosphor selection. PN wrote the remaining sections and handled all the visualizations. I had supportive role throughout the review process.

Paper IX: 3D-tomographic reconstruction of gliding arc plasma

This study introduces method for studying gliding arc discharges using 3D emission tomography, which allows for detailed volumetric measurements of plasma luminosity fields. This technique provides a more comprehensive view of the arc's structure and dynamics compared to traditional 2D methods, which often miss crucial details.

By using multiple CMOS cameras positioned around the plasma to capture simultaneous images of the arc from different angles. These images were then processed to reconstruct a 3D model of the plasma discharge. The study reveals several important findings. First, the arc length was shown to increase with airflow up to a certain point, after which higher flow rates caused the arc to shorten due to turbulence. In contrast, 2D projections consistently underestimated the arc length by up to 15%, especially at higher flow rates where the arc's curvature was more pronounced.

DS and I conducted the experimental activities together. The data analysis was carried out collaboratively by DS, AR, and me. DS was responsible for data visualization, creating the figures, and writing the article. I had supportive role throughout the review process.

Paper X: Effect of a single nanosecond pulsed discharge on a flat methane–air flame

This study explores how a nanosecond pulsed discharge impacts methane–air combustion. A single pulse, with an amplitude between 30 and 50 kV, was applied to a flat premixed flame at atmospheric pressure, and the effects were analyzed using optical and laser diagnostics.

It was found that the plasma pulse increased the flame speed for several milliseconds without significantly raising the gas temperature, suggesting that the enhancement is driven primarily by chemical rather than thermal effects. Additionally, formaldehyde formation an indicator of early combustion reactions was observed to increase in both the unburnt and preheat zones after the plasma pulse, demonstrating the plasma's influence on combustion chemistry. Temperature measurements revealed minimal changes at the flame front immediately following the pulse, but localized heating was detected near plasma filaments in the unburnt region.

YB, CK, JR, and JS conducted the measurements. YB, CK, and JS carried out the data analysis and visualization. I performed COMSOL simulations to support the findings and assisted in constructing the experimental setup. I had supportive role throughout the review process.

Paper XI: Application of emission spectroscopy in plasma-assisted NH_3/air combustion using nanosecond pulsed discharge

The study explores the influence of nanosecond pulsed plasma discharges on ammonia (NH_3) and air combustion using optical emission spectroscopy (OES). The study reveals that plasma discharges generate excited nitrogen (N_2^*) and hydrogen (H^*) species, which play a crucial role in enhancing combustion. These reactive species contribute to both the kinetic and thermal effects observed in NH_3 combustion. It was observed that two distinct emission events within a single discharge pulse, separated by 80 nanoseconds, each exhibiting a double exponential decay pattern.

The plasma discharges also lead to significant localized gas heating, raising the temperature by up to 700 K in the flame region. Additionally, the electron density along the flame increases, reaching up to 1×10^{17} electrons per cubic centimeter. The study finds that approximately 20% of the discharge energy is used for gas heating, with the remaining energy driving important kinetic processes that enhance combustion.

JS, YB, and JR conducted the experiments. JS handled the analysis, visualization, and figure creation and wrote the paper . I assisted in constructing the experimental setup. I had supportive role throughout the review process.

Paper XII: Photofragmentation laser-induced fluorescence imaging of CH_3 by structured illumination in a plasma discharge

The study introduces a new for detecting methyl radicals (CH_3) in plasma-assisted methane dehydrogenation. CH_3 is a key intermediate in such processes, but its detection is challenging due to its high reactivity and interference from naturally occurring CH fragments.

This was solved by use Photofragmentation Planar Laser-Induced Fluorescence (PF-LIF) combined with structured illumination. This approach involves using a laser to fragment CH_3 into CH radicals, which are then imaged with a probe laser. Structured illumination helps distinguish between CH radicals produced from CH_3 photofragmentation and those naturally occurring in the plasma, reducing background interference and improving the clarity of the signal.

The study shows that this method successfully detects CH_3 in a methane-argon plasma, with structured illumination significantly enhancing signal clarity. The results also reveal that CH_3 quickly reacts with its environment, displaying a multi-exponential decay.

I built the experimental setup and conducted the measurements with JP and JR. I performed the data analysis, created the visualizations and figures, and authored the paper.

Paper XIII: Holistic analysis of a gliding arc discharge using 3D tomography and single-shot fluorescence lifetime imaging

The study explores gliding arc plasmas, which are vital for sustainable chemical processes due to their high temperatures and efficient energy transfer. These plasmas are complex, making traditional 2D analysis difficult. To address this, the researchers combined single-shot fluorescence lifetime imaging of hydroxyl radicals with 3D optical emission tomography to gain a detailed understanding of the plasma's structure and behavior.

This allows us to map the spatial distribution of OH radicals and the plasma arc, revealing how increased flow rates lead to more turbulent plasma structures and shorter arc lengths. The FLI method also corrected for quenching effects, enabling accurate measurement of OH densities and temperature variations.

DS and I performed the experiments. The data analysis was carried out collaboratively by DS, AR, and me. I made all the figures and visualization. I authored the article.

Paper XIV: Fluorescence lifetime imaging of nitric oxide in nanosecond pulsed discharge-assisted NH_3/air flames

The work studies NO fluorescence lifetime in ammonia NH3/air flames enhanced by nanosecond pulsed discharges (NPD), crucial for improving plasma-assisted combustion (PAC) of ammonia, a promising carbon-free fuel. Using laser-induced fluorescence (LIF), the study reveals distinct behaviors in the burnt and unburnt flame zones.

In the burnt zone, NO fluorescence lifetime increased slightly due to a temperature rise, primarily governed by the number density of particles. In contrast, in the unburnt zone, NO exhibited a much longer fluorescence lifetime than expected, likely influenced by plasma-generated excited radicals like N_2^*. Additionally, a shockwave in the burnt zone caused a localized dip in lifetime due to gas compression, emphasizing the importance of number density in quenching dynamics.

JS built the experimental setup and collected the data, performed measurement and analysis. I had supportive role building the experimental setup. I had supportive role in the analysis and help discussing key results.